NONLINEAR CIRCUITS AND ANTENNAS FOR

MICROWAVE ENERGY CONVERSION

by

JOSEPH ALEXEI HAGERTY

B.S., University of Houston, 1998

M.S., University of Colorado, 2001

A thesis submitted to the

Faculty of the Graduate School of the

University of Colorado in partial fulfillment

of the requirements for the degree of

Doctor of Philosophy

Department of Electrical and Computer Engineering

2003

This thesis for the Doctor of Philosophy degree by

Joseph Alexei Hagerty

has been approved for the

Department of

Electrical and Computer Engineering

by

_____

Zoya Popović

_____

Regan Zane

Date _____

The final copy of this thesis has been examined by the signatories, and we
find that both the content and the form meet acceptable presentation
standards of scholarly work in the above mentioned discipline.

Hagerty, Joseph Alexei (Ph.D., Electrical Engineering)

Nonlinear Circuits and Antennas for Microwave Energy Conversion

Thesis directed by Professor Zoya Popović

This thesis covers theory and experiment for four distinct applications involving RF–DC and DC–RF energy conversion between 1 and 18 GHz. Microwave circuits and antennas containing nonlinear elements are used with high-efficiency operation techniques in a microwave rectifier, broadband rectifying antenna array, switched-mode oscillator, and switched-mode oscillating antenna. The applications include dc-dc conversion at microwave switching speeds, broadband energy recycling with microwave rectifying arrays, and a high-efficiency transmitting antenna for free-space power combining.

Switched-mode operation for rectifiers is discussed in terms of nonlinearly driven diodes used with proper harmonic terminations and impedance matching. The results are organized in terms of classes of operation in the same way as is done for microwave amplifiers. What is unique for this thesis is the application of these switched-mode classifications to microwave rectifiers.

The next topic is a broadband rectenna for low-power ambient energy recycling (the term *rectenna* is simply a neologism for *rect*ifying ant*enna*). A broadband rectenna element and 64-element array are extensively characterized for energy recycling of arbitrarily polarized stray fields in the microwave region to usable DC energy. Concepts gathered from the rectifier analysis are

used together with a nonlinear simulation technique and antenna analysis to design the rectenna and rectenna array.

Next, the class-E mode of amplification is applied to a free-running oscillator at 10-GHz. This highly nonlinear, switched-mode class of operation, which has been documented at 10 GHz for amplifiers, is analyzed further for application in a high-efficiency oscillator. The analysis techniques provide a framework for future, improved versions of the class-E oscillator and the oscillator is evaluated as the DC–RF stage of a DC–DC converter.

Finally, a class-E oscillating annular ring antenna for a high-efficiency transmitting array. An extensive characterization of this active antenna is presented for class-E operation, antenna geometry, and oscillatory behavior. Future work is proposed for a 24-element array with a concentration on the phase-locking and coupling of individual elements.

Future and related work is suggested for each of the four previously mentioned topics along with a proposal for new work on a DC–DC converter which makes use of the high-efficiency rectifiers and oscillators.

Dedication

To family, friends, and dogs

Acknowledgments

I would like to acknowledge, offer thanks, and otherwise recognize the positive influence of a few dozen or more friends and colleagues. As a German friend pointed out to me, the people on this list might rather appreciate a beer than a mention on paper, and that offer hereby stands. Nevertheless, let this list limn historical, from the fall of 1997 to the summer of 2003, my time in the electromagnetics world.

From the University of Houston:

Lori Basilio, Amit Mehrotra, Stuart Long, Jeff Williams and Michael Khayat

From my brief post as a practicing EMI engineer:

Mark Upcavage

From the beginning at the University of Colorado:

Thanks very much to Zoya Popović for the tutelage, the financial support and the opportunity; Helen Frey, Michael Forman, Wayne Shiroma, and Manoja

Weiss

My forefathers and good friends in the Antenna Lab:
Jan Peeters Weem, Joe Tustin, Jim Vian, and Todd Marshall

My successors and new friends:
Nestor and Ileana, Sébastien Rondineau, Christi Walsh, Alan Brannon, Narisi Wang, Patrick Bell, Matt Osmus, and Deki Filipović

My contemporaries and friends in suffering:
Paja Pajić, Paul Smith, Darko Popović, Stefania Römisch, Rachael Tearle, Jason Breitbarth, Edeline Fotheringham, and Naoyuki (Nao) Shino

Meinen Deutschen, Österreichischen, Italienischen, Koreanishen und Bayerischen Bekannten und Bierkumpeln bei der Technischen Universität München:
Florian Helmbrecht, Paul Matyas, Martin Kaleja, Johannes Russer, Fabio Coccetti, Mark Kühn, Michael Zedler, Robert Wanner, Jung Han Choi, Klaus Heppenheimer, Tobias Hermann and Bruno Biscontini

Contents

ix

Tables

Figures

xvi

xvii

xviii

Chapter 1

Introduction and Background

The phrase *Nonlinear Circuits and Antennas* used in the title of this thesis refers to passive microwave transmission lines and wave-guiding structures that are integrated with nonlinear semiconductor devices such as diodes and transistors. The nonlinearity of the device is used to transfer or convert energy in one form to another, such as DC to radio frequency (RF). The process of performing this conversion efficiently using microwave circuit techniques and nonlinear analysis is the task of this thesis. While energy conversion at microwave frequencies has been done for over 40 years, the high-efficiency techniques and applications discussed herein are either less than 8 years old or introduced here for the first time.

1.1 Thesis Organization

Four types of microwave energy conversion are covered in this thesis. In each case, the conversion is between electric potential (the expenditure of which is referred to as DC), and electromagnetic wave energy both guided and radiated, in the RF/microwave frequency range.

1.1.1 Microwave Rectifier

The first form of microwave energy conversion discussed is RF-DC conversion as performed by a microwave rectifier (Chapter 2). In this project, a transmission line loaded with a nonlinear Schottky diode is used to convert guided RF into usable and/or storable energy for DC loads. Chapter 2 looks at circuit methods for achieving high efficiency RF-DC conversion at $1\,\mathrm{GHz}$ using proper impedance matching and harmonic terminations. The results are organized into special classes or modes of microwave rectification based on definitions used for high-efficiency amplifiers.

1.1.2 Microwave Rectifying Array

A second kind of RF-DC conversion, free-space RF waves to DC, is addressed in Chapter 3. Such an instrument is known as a *rectenna* which is a *portmanteau* word for **Rect**ifying Ant**enna**. This converter uses antennas loaded with diodes at the antenna feed points to capture and convert low-power, stray, ambient RF as efficiently as possible. The chapter explores solutions for recti-

fication of multi-frequency (between 1 and 18 GHz), random orientation, and low-power RF and pursues novel measurement methods of such a system.

1.1.3 Microwave Oscillator

Energy conversion in the reverse direction, DC–RF is the topic of Chapters 4 and 5. Chapter 4 looks at the generation of guided RF at 10 GHz from DC in the form of a high-efficiency transmission line oscillator. The important points in this chapter are methods used and conclusions drawn in designing a high efficiency oscillator around a high efficiency amplifier.

1.1.4 Microwave Oscillating Antenna

Finally, in Chapter 5, an active antenna is presented which efficiently radiates the RF it converts from DC. The principle of operation is nearly the same as the oscillator in Chapter 4, only that instead of using a $50\,\Omega$ output the feedback loop of the oscillator is used as an antenna. Special attention is given to the antenna design and overall conversion of DC to RF contained in the main beam of the antenna.

1.1.5 Related and Future Work

Each of the four converters can be used together for additional forms of energy conversion as well: A proposed application of the rectenna is for conversion of stray energy at multiple frequencies first to DC, then to use

the DC over time to intermittently power transmission at another frequency. Such a system would constitute an RF–RF converter involving both an RF–DC and DC–RF stage. The DC–RF stage can take the form of an oscillator or amplifier in this case.

Conversely, DC–DC conversion can be used to regulate and/or provide Galvonic isolation between a DC-supply and DC-load. This would involve a DC–RF and RF–DC stage in the opposite order from the RF–RF converter. The reason for performing the energy conversion back and forth from microwave frequencies is discussed throughout the thesis.

1.2   Microwave Energy Conversion

The term energy conversion is used instead of power conversion throughout this thesis. The reason stems from the applications and modes of operation intended for the circuits and antennas discussed: In most of the hypothetic applications for either RF–DC or DC–RF conversion the input is typically not a continuous source. In fact, for the rectenna array (Chapter 3), the input is a superposition of electromagnetic waves of time varying frequency and amplitude. Furthermore, the output is not continuous, but rather stored energy dissipated intermittently as DC power. The DC–RF oscillators may be used as high-efficiency, battery controlled communication components with strict power consumption requirements, or as the first stage in a DC–DC converter with similar constraints. For these reasons the term energy conversion used

to emphasize the non-continuous operation of each converter as well as its application under limited energy reserve.

1.3 High-Efficiency Operation

Semiconductors, composed of materials which become lossier with increasing operation frequency, are also limited by physical dimensions leading to device reactances which also become significant at higher frequencies. In the microwave region, between 1 and 30 GHz, semiconductor deficiencies are manifested in the form of ohmic losses in the device. Circuit efficiencies defined by DC–RF, RF–DC, RF–RF, and DC–DC conversion scale directly with energy consumption and battery lifetime: A circuit with twice the efficiency of another uses half as much power for the same application with operating twice as long on the same supply. Furthermore, the higher the efficiency, the less heat is produced.

One way to remedy the losses incurred at higher frequencies is to continue to tailor the semiconductor for high frequency operation. Such has been done with MESFET and HEMT technologies which have sought to reduce physical dimensions, transit times, and loss mechanisms at the expense of power handling capability. The other approach is to introduce external circuits designed to overcome deficiencies in the semiconductor. Such is the purpose of the well-documented amplifier classes B through H and S, [2, 3]. The strategy of each of these classes of transistor operation is to move the device out of a

small-signal, linear regime into a mode which allows greater performance in terms of power and/or efficiency. Of course improved performance is usually gained at the expense of linearity and bandwidth. Furthermore, a transistor driven with nonlinear transconductance, to the point of switch-like behavior, is necessarily attended by significant harmonic content. It is typically the degree of nonlinearity (how hard the device is driven and bias level), attention to the device output impedance (based on device reactances), and storage of the energy created at the harmonics that is of concern to the high-efficiency microwave circuit designer.

The rectifiers presented in Chapter 2 address the concerns of high efficiency in just this way. A diode driven with a relatively large input (compared to the diode power handling limits) is terminated with appropriate impedances at DC, the fundamental, and harmonics to shape the diode voltage and current waveforms. Optimized waveforms are those which avoid regions of high ohmic loss in the diode operation. The result is a set of four rectification classes defined by optimized impedance values for a given diode.

The well-established class-E mode of amplification is used for the oscillators of Chapter 4 and Chapter 5. This class of operation notably considers the internal reactance of the device and seeks to control when and when not energy is stored in the transistor. In this way, ohmic losses are minimized during the switch-like class-E operation.

The high-efficiency nonlinear regimes discussed here are responsible for energy conversion ratios 1.2 to 2 times higher than conventional operation

6

modes. The implications this has on energy consumption and battery lifetime form the crux of the emphasis placed on high-efficiency.

1.4 Analysis Methods

In this thesis an emphasis is placed on measurement solutions to problems that numerical analysis can not fully address. The nonlinear phenomena encountered typically have parameters which vary with applied RF power, frequency, DC power, and harmonic content. Not surprisingly, analytic methods for optimizing a particular parameter lead quickly to intractable coupled differential equations. An example can be found in [4] for optimizing DC–RF conversion efficiency in microwave switched-mode amplification. There, the nonlinearly operated transistor was reduced to a switch circuit element with harmonic content. For microwave switched-mode oscillators, the dynamics of chaos and stability also enter the picture, further limiting the power of numerical analysis.

As nonlinear circuit equations become more complex, the Harmonic Balance technique becomes indispensable. Explanations of this nonlinear-circuit analysis method are given in [5, 1]. In [6], for instance, a static analysis of diode IV characteristics was used to predict RF–DC conversion properties for rectennas. This method was integral in the design of some of the most important and successful rectenna work to date. In this thesis, a more complex diode analysis is necessary to take into account multiple frequency and

harmonic content not taken into account by [6]. In this way HB is used, for example, to compare rectifier performance with various harmonic terminations and for various types of diodes and to study performance trends as a function of source and load impedances for the class-E oscillator.

In still other cases, HB and the nonlinear models used in HB are simply not accurate enough to use for a final circuit design: for example, finding the operating point for a switched mode oscillator in terms of loop gain, output power, gate and drain bias, and source and load impedance. In this case, separate measurements on isolated portions of the oscillator are used to predict oscillator performance as a function of each of these. This can require thousands of data points taken over all dimension of interest. In this case computerized techniques are developed to both take and process the data.

In Chapters 2 and 4, the HB routine from Agilent *ADS* is used extensively for analysis and design in terms impedance terminations and nonlinear response to power. In Chapter 2 a impedance tuning system known as a source-pull/load-pull system is used to compare results to the HB simulations. In Chapter 4, the oscillator design relies most heavily on measurements made on individual components of the oscillator, such as the amplifier and resonator. In Chapter 3, antenna and diode measurements are used in equal weight with MoM and HB simulations in the rectenna design. Results of the oscillator study in Chapter 4 are used together with MoM simulations and field equations to design the active antenna in Chapter 5.

Chapter 2

RF–DC Conversion: Microwave Rectifiers

Microwave rectification has predominately been used and discussed in the context of microwave rectennas (rectifying antennas). Rectennas and rectifiers have a wide variety of applications including dc-dc conversion [7], space solar power stations [8], remote actuation [9], signal detection [10], and stray-energy recycling [11]. In each of these cases high RF–DC conversion efficiency is a primary concern. Typically the rectifier can be optimized separately from the antenna or converter as an independent circuit component. In the past, this has been done only by impedance matching at the fundamental frequency. Little attention, however, has been given to studying the effects of properly terminating the harmonic content generated by the diode during rectification. In this chapter, switched-mode principles of

operation for which proper termination of the harmonics is essential, are applied to microwave rectifiers in much the same way as those methods are applied to high-efficiency microwave amplifiers. The main goal of this chapter is to assess various rectification modes in terms of high and/or optimal dc-rf conversion efficiency for realistic diodes at microwave frequencies.

2.1   Rectification

Rectification, or ac-dc conversion, has long been understood for low frequency operation. In its simplest form, a series diode may be used to pass one-half of the ac-cycle to an RC circuit where the time-varying content is filtered and only the DC component appears across the load. Such a half-wave rectifier is limited to 50% AC-DC power conversion for an ideal diode. At microwave frequencies, the rectifier circuit must be looked at as a resonant circuit, containing a nonlinear element (i.e. shunt diode) which traps modes of the fundamental frequency and its harmonics. If the circuit is matched at each frequency, the rectifier acts as a full-wave rectifier (even though only one diode is used).

In addition to harmonics, the nonlinear diode creates a dc-bias in the resonant circuit which can be extracted without affecting the RF characteristics of the resonant circuit. The time varying voltage and current relationship at the physical point of the diode in the cavity determines the loss in the diode and, consequently, the RF–DC efficiency. If the cavity is high-Q for the

fundamental and harmonics (not much energy is lost in the diode or escapes the cavity), the dc-rf efficiency can approach 100%. If the RF circuit is well designed, the losses can be limited to the forward voltage, reverse breakdown voltage, and series resistance of the diode.

Figure 2.1 depicts the principle of microwave rectification. In the following subsections, the generalized microwave rectifier is further explained before the high-efficiency methods are discussed.

2.1.1 Figures of Merit

The critical definition of efficiency relates the total input power to the the total DC output power delivered to a load, R_L:

$$\eta_{rf-dc} = \frac{P_{rf(in)}}{P_{dc(out)}} = \frac{P_{rf(in)}}{V_{dc}^2/R_L}. \tag{2.1}$$

The main sources of loss are due to I^2/R dissipation in the diode, reflected power at the fundamental, and power lost in the harmonics generated by the diode. Some have defined a conversion efficiency which does not take into account the reflected power of the fundamental:

$$\eta_{conv} = \frac{P_{rf(in)} - P_{rf(refl)}}{P_{dc(out)}}. \tag{2.2}$$

This definition only takes into account the efficiency of the diode and not the efficiency of the entire circuit. The usable DC power is always defined as the DC power dissipated in a DC load, R_L. The reflected power is always
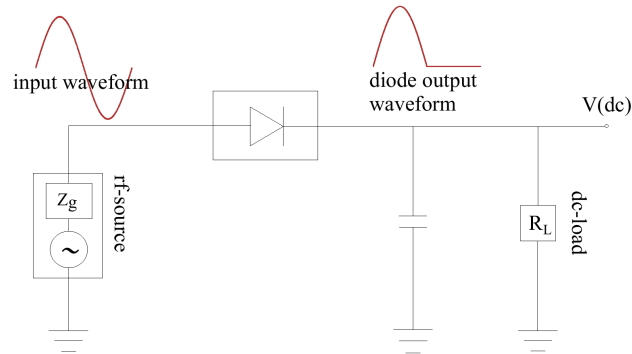
(a)
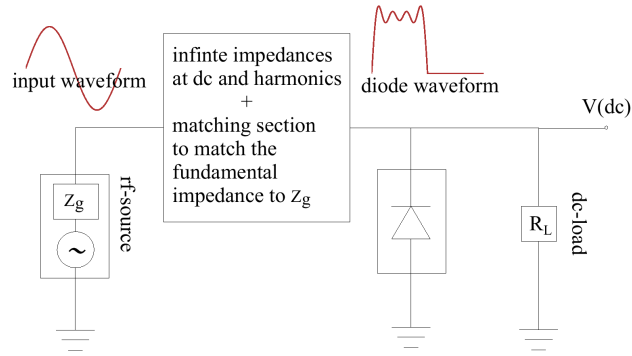
(b)

Figure 2.1: Standard half-wave rectifier (a) and microwave model of the rectifier (b) with impedance matching at dc, the fundamental, and harmonics.

defined here as the power reflected in the fundamental not including the power lost to the source in the harmonics:

$$P_{refl} = P(f_o)_{refl} \quad \text{and} \quad P_{refl-tot} = \sum_{i=1}^{\infty} P(f_i)_{refl} \quad (2.3)$$

The reflected can also be defined, though not for this study, as the ratio of the total power reflected at the fundamental and harmonics to $P_i n$.

12

2.1.2 IV Curves

The dc characteristics of a diode can be described by a variable resistor with an *IV* relationship given by

$$I(V) = I_s(e^{\frac{V}{KT/q}} - 1). \tag{2.4}$$

A very convenient way of predicting rectifier behavior and identifying loss mechanisms is by using diode *IV* curves relating the drawn current to the applied diode voltage. Figure 2.2 (a) and Figure 2.2 (b) show *IV* curves for Equation 2.4, the *Spice* model of a MA4E2054, and the measured curves for the the MA4E2054 and SMS7630 diodes.

2.1.3 RF Diode Impedance

To compute the input impedance of a diode, $Z_{in}(\omega, V)$, the expression

$$G_d = \frac{1}{R_j} = \frac{dI}{dV}\bigg|_{V=V_o} \tag{2.5}$$

can be used to include the voltage dependence. Since we also have the formula relating current and voltage across the nonlinear resistor given in Equation 2.4, a Taylor expansion can be used to obtain

$$R_j = \frac{1}{\alpha I_s e^{\alpha V}\big|_{V=V_o}} \tag{2.6}$$

for small signals. To calculate Z_{in} the junction capacitance C_j, package inductance L_p, package capacitance C_p, and series resistance R_s, are included
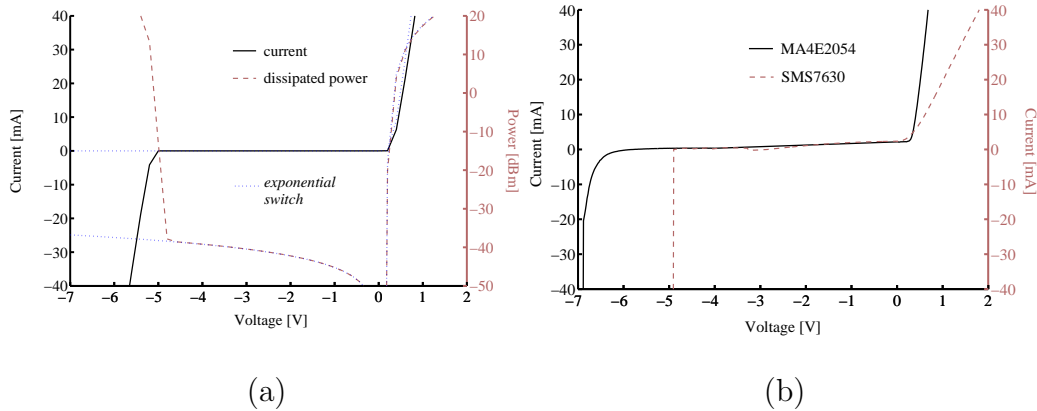
Figure 2.2: Simulated (a) and measured (b) *IV*-curves. The curves in (a) are for an exponential and *Spice* model of the MaCom MA2E2054 Schottky diode. The measured characteristic of the MA2E2054 is compared in (b) with the Alpha SMS7630 diode used in Chapter 3. In (a) it is also shown how the power dissipated in the diode is large in the case of operation near the reverse breakdown region.

in parallel with R_j so that

$$Z_{in} = C_p \parallel (L_p + R_s + C_j \parallel R_j) \tag{2.7}$$

and finally

$$Z_{in}(\omega, V) = \left[j\omega C_p + (j\omega L_p + R_s + \frac{1}{\alpha I_s e^{\alpha V} + j\omega C_j})^{-1} \right]^{-1}. \tag{2.8}$$

However, Equation 2.8 is a only a useful predictor of the nonlinear diode input impedance under small-signal conditions. As with similar definitions of small-signal transistor input and output impedances, this definition is of limited use when large-signal matching of the fundamental frequency and harmonics are necessary.

For this reason, the Harmonic Balance (HB) method of nonlinear circuit analysis is used here to simulate and analyze the RF rectifier. HB intrinsically uses Equation 2.4 and the equivalent circuit represented by Equation 2.8. In addition, HB takes into account the energy at DC, the fundamental frequency, and a specified number of harmonics in the circuit.
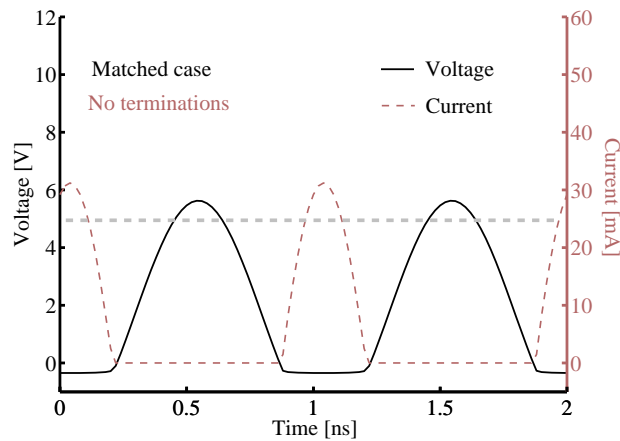
Figure 2.3: Simulated voltage and current waveforms at 1 GHz for a diode matched at the fundamental for efficiency without additional matching for the harmonics. Waveforms appear across a switch modeled by an exponential curve in parallel with a capacitor.

2.1.4   Diode Waveforms

The simulated waveform of Figure 2.3 is obtained using HB in Agilent *ADS* for a variable resistor given by Equation 2.4 in parallel with a junction capacitance of $0.1 \, \text{pF}$. The idealized diode is matched at the fundamental frequency for optimal rectification efficiency. The voltage and current levels

15

can be compared to Figure 2.2 (a) to see how normal operation of the diode breaches the high-loss regions of the *IV* curve. If either of the *Spice* models had been used, the voltage waveform would have been clipped at the reverse breakdown voltage.

(a) (b)
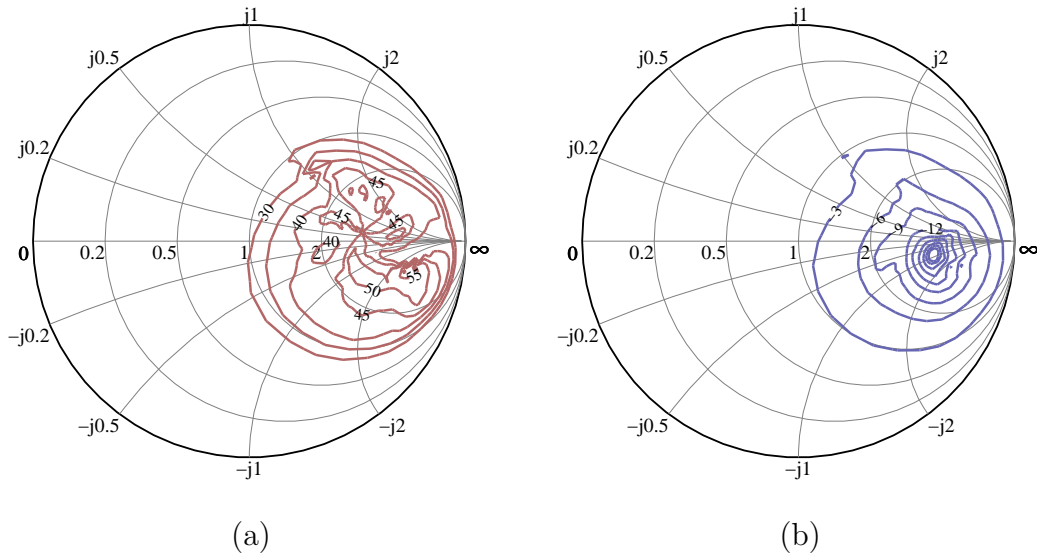
Figure 2.4: Source-pull diagram of the un-harmonically terminated case. Rf-dc conversion efficiency (a) normalized rf reflected power (b). Contours of constant efficiency [%] and relative reflected power [db] are plotted over varying source impedance.

2.1.5 Diode Matching

The source-pull diagram of Figure 2.4(*source-pull* is to be explained later) shows how the dc-rf rectification efficiency varies with impedance tuning. The source impedance where the optimal efficiency occurs corresponds to the maximum rectified output power and the best matching for this case.

16

However, this case does not include harmonic terminations. Later sections show how proper impedance matching at the fundamental, DC and harmonics can improve the efficiency further.

2.2   Special Modes of Rectification

Class-E behavior was first introduced in the context of an amplifier by Sokal and Sokal in 1975 [12]. The theory was modified in 1988 in [13] for rectifiers to be used in high-efficiency DC-DC converters [14, 15]. In both cases the frequency of operation was around $1\,\mathrm{MHz}$. Mader further developed class-E theory for transmission line amplifiers at microwave frequencies in 1995 [16]. Mader's work is modified here, for the first time, for microwave transmission line rectifiers. The outline of Mader's approach is paraphrased here for brevity and details are left out where they are identical to his original analysis.

2.2.1   Class-E Rectification

The development of the simplified class-E rectifier theory begins with the assumptions that 100% RF–DC efficiency can be achieved with an ideal switch in parallel with a linear capacitance, C_s. This corresponds to the nonlinear resistor, R_j, and the junction capacitance, C_j, in the diode. The RF voltage that drives the switch is assumed to generate a 50% duty cycle. During the OFF (open) cycle of the switch, C_s stores energy which is partially dis-

sipated in the switch during the ON cycle if there is any resistance in the closed switch. The output impedance of the switch is then designed to present impedances at the fundamental and harmonics that will force C_s to dissipate all its stored energy *before* the switch closes. Additional assumptions about the instantaneous switch voltage and slope of the voltage at the moments of switching serve as initial conditions for the circuit equations which determine the following impedances to be seen by the diode:

$$\text{at DC:} \qquad R_L = \frac{V_s}{I_s} = \frac{1}{\pi \omega_s C_s}$$

$$f_{fund}: \qquad Z_{net} = \frac{v_s}{i_s} = \frac{0.28}{\omega_s C_s} e^{j49°}$$

$$f_{harm}: \qquad Z_{harm} = \frac{v_s}{0} = \infty$$

$$(2.9)$$

The strategy for implementing the *class-E impedance* at the fundamental is to transform the source impedance to this value. The harmonic impedances are created by using open circuited transmission lines of appropriate length and distance from the diode. In practice, only the second and third harmonic are terminated with an open circuit. The limitations of using a finite number of harmonics in class-E has been addressed in [17]. The DC load resistance is rf-decoupled from the circuit using a usual bias network.

In order to solve for the anticipated V_{dc}, I_{dc}, $v(t)_{max}$, and $i(t)_{max}$, Equation 2.9 must be solved for using $V_{dc}I_{dc} = P_{in}$ for 100% efficiency. The resulting class-E voltage and current waveforms across the switch-element of the diode are shown in Figure 2.6. As will be shown, this first order approximation of the class-E impedances will have limitations for large signal operation and alternative design methods are discussed and proposed.

2.2.2 Class-F Rectification

Class-F theory has been developed in a less extensive manner than class-E for microwave transmission line circuits. The critical aspect of class-F behavior is the wave-shaping accomplished by the harmonic terminations: even harmonics are terminated with an open circuit, odd harmonics with a short circuit such that the switch voltage achieves a *square* wave shape. The determination of the fundamental impedance is designed for maximal power transfer to the load in the case of an amplifier. It has been shown that a *real* impedance equal to $2V_{ds}/I_{dss}$ can be used (even in saturation) for the fundamental impedance. However, like the class-E impedances, the optimal fundamental impedance for class-F will be better found using non-linear simulation techniques rather than first order approximations.

2.2.3 Inverse Class-E and Class-F

The less common inverse modes of class-E and class-F are defined by their harmonic terminations which are opposite in phase angle from their counterparts. In inverse class-E, or class-Ei, each harmonic termination is a short circuit. The class-Ei circuit design and switch waveforms bear no resemblance to class-E and do not employ the philosophy of draining the stored charge in C_s before the switch turns on. Similarly, in class-Fi, the even harmonics are terminated with a short circuit and the odd harmonics with opens. In both cases there are no design guidelines for the optimal DC and fundamental impedances. Therefore, nonlinear simulations will be used to find these. The reason for considering these two classes for rectifiers is that class-Ei has a short conduction period and high current peak, while class-Fi has a squared current waveform. Each case can provide special advantages and disadvantages depending on the diode, RF input level, and/or load resistance.

2.2.4 Comparison of Waveforms

The effect of these special cases of impedance terminations on the diode waveforms are demonstrated in this section for an idealized rectifier at 1 GHz with a diode based on Equation 2.4 in parallel with a capacitor. The same scale is used for each case as was used in Figure 2.3 for the matched diode. Each waveform is also taken at the optimal fundamental impedance and DC load resistance for that particular mode.

In Figure 2.5(a), it can be seen how the squared-off shape of the class-F voltage waveform maintains the voltage below about 5 V in the reverse bias region. At the same time, the total current and peak current value is kept below 30 mA. The class-Ei waveform of Figure 2.5(b) shows the decreased conduction cycle, as described earlier. It can be seen that the large current peak, over 50 mA in this case will cause greater instantaneous $I^2 R_s$ losses but comparable total $\int I^2 R_s dt$ energy loss to class-F since the current duty cycle is smaller. The advantage of class-Ei is in the small voltage peak, as will be discussed.
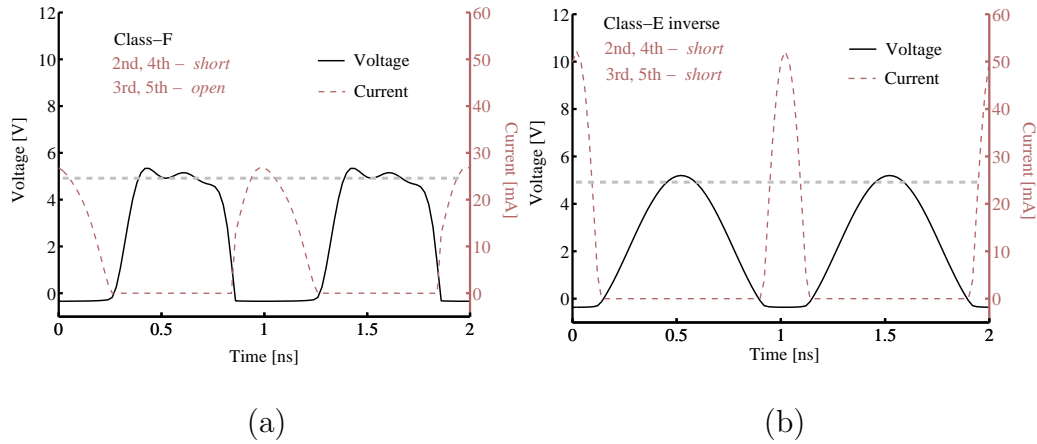
Figure 2.5: Class-F (a) and Class-Ei (b) waveforms appearing at across the idealized exponential switch.

The class-E waveform of Figure 2.6(a) shows the same familiar current and voltage characteristics as has been demonstrated in the past for class-E amplifiers (though reversed in time). The important aspect for rectifiers is that the voltage across the switch becomes very high, while the total current

21
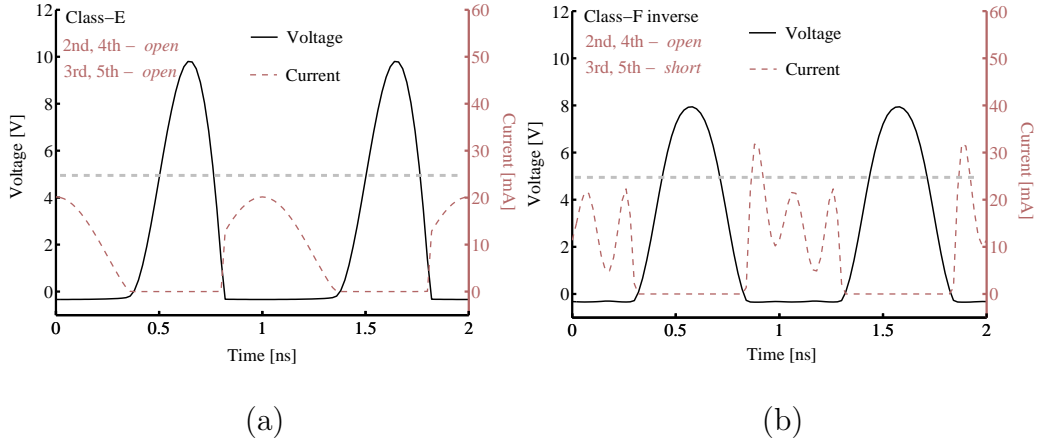
Figure 2.6: Class-E (a) and Class-Fi (b) waveforms appearing at across the idealized exponential switch.

draw is very small. Similarly, in class-Fi shown in Figure 2.6(b) the current approaches a square shape (only 4 harmonics are used) and the total $\int I^2 R_s dt$ energy loss is small compared to classes F and Ei. However, like class-E, the voltage peak is high.

The voltage and current waveforms are direct consequences of the harmonic terminations. Class-E includes the additional rigorous definition of the fundamental impedance. Each special case has an advantage for four particular cases of operating condition and diode type.

As can be seen in Table 2.1 Class-F is ideal for the worst (and most realistic) kind of diode, low reverse-voltage breakdown and high series resistance. Class-E and class-Fi can be used if the input RF power is so low that the peak voltage becomes less than the reverse breakdown voltage. However, as the input RF decreases, each class begins to operate with approximately the

Table 2.1: Most suitable rectification mode vs. diode reverse breakdown, V_{rB} and series resistance, R_s.

	high R_s	low R_s
low V_{rB}	class-F	class-Ei
high V_{rB}	class-E	class-Fi

same efficiency.

2.3   Harmonic Terminations

The impedance terminations at the harmonics of the input RF frequency, referred to as harmonic terminations, are of fundamental importance to high-efficiency rectification. In order to prevent losing the energy which is converted into harmonics, notch filters can be used to present a reflection coefficient of unity magnitude to the diode at the harmonics. The phase of the reflection coefficient is primarily responsible for the wave-shaping at the diode terminals. The previously discussed special modes are four special cases of the infinite array of possible harmonic terminations. In this section, diode rectification is addressed in terms of a continuum of harmonic-termination phase combinations.

The same HB simulations used to generate the waveforms in the previous section are modified to allow sweeps in harmonic termination reflection coefficients. In this section, an idealized switch and diode model are simulated at $1\,\mathrm{GHz}$ and $13.2\,\mathrm{dBm}$ input power. Each of the second through fifth

harmonics are terminated with a reflection coefficient of magnitude 0.92 and variable phase. The second and fourth harmonics are stepped in increments of 9° as the third and fifth harmonic are swept every 9°. The result is shown as a plot of rectified voltage vs. even and odd harmonic termination phase angle.

A fundamental impedance and load resistance between the optimal values of Z_{fund} and R_L for class-E and class-F are also chosen in each case. This allows comparison of harmonic-termination response between these two classes which does not depend on the termination of the fundamental. This also means however that the class of operation is not optimal class-E or F when the harmonics reach their class-E or F values.

2.3.1 Simulations Using an Exponential Switch

An idealized diode is created using the resistance given by Equation 2.4 in parallel with a $0.10\,\mathrm{pF}$ capacitor and both in series with a resistance of $11\,\Omega$ (C_j and R_s for the MA4E2054). In this case there is no reverse breakdown voltage and the diode is referred to here as an exponential switch. Therefore the main source of loss is expected to be during current conduction through the series resistance.

The results of Figure 2.7 show that optimal rectification performance results for regions near the class-F and class-E terminations. This is due to the near 180° current conduction angle and smooth transition of charge. In the case of short-circuited even harmonics, the conduction angle becomes

24
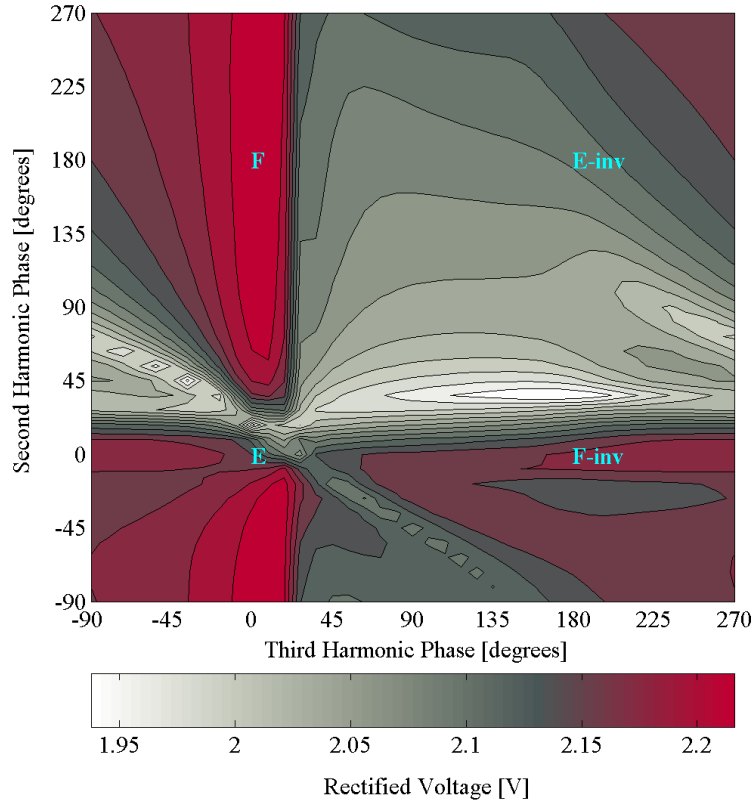
Figure 2.7: Simulated second and third harmonic termination phase sweeps for an idealized exponential switch.

small for short-circuited odd harmonics (class-Ei region). Here the current reaches a large value and much power is dissipated in R_s. In the class-Fi region, the conduction angle increases and the current waveform becomes squared-off. This effect is beneficial because the IR^2 power is minimized.

2.3.2 Simulations Using a Diode Model
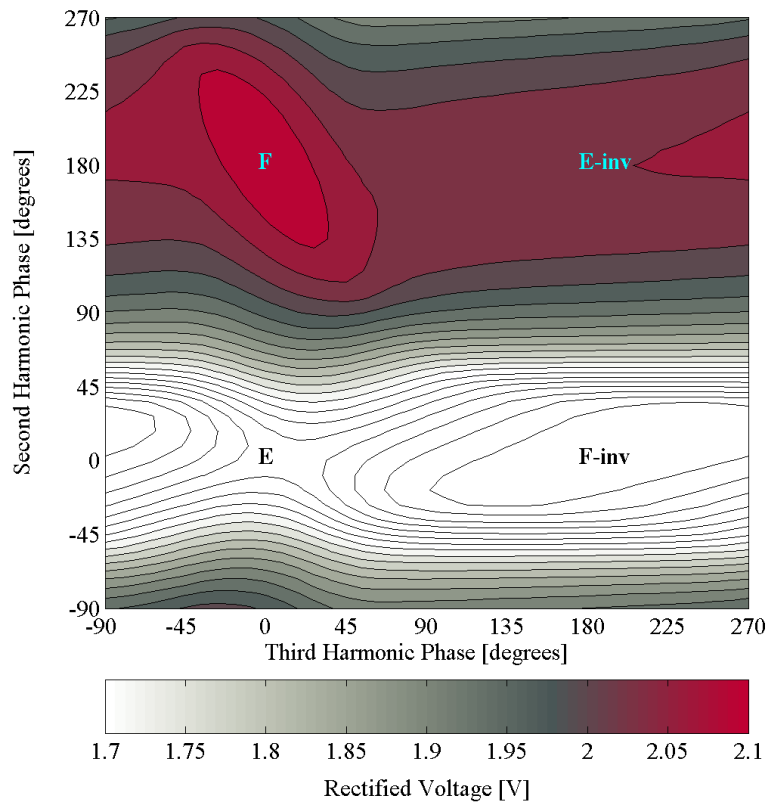
Figure 2.8: Simulated second and third harmonic-termination phase sweeps for the spice model of the diode.

The spice model for the MA4E2054 diode is simulated with the same frequency and power as the exponential switch, but with slightly modified fundamental input impedance for comparison purposes. In this case the breakdown voltage of $5\,\mathrm{V}$ becomes a large factor, as demonstrated by Fig-

ure 2.5 and Figure 2.6.

Figure 2.8 shows that the favored region is now purely the case where the voltage is squared-off and kept below the breakdown voltage. Furthermore, the low-conduction angle, high current peak case (class-Ei) actually becomes much more favorable than class-E and class-Fi simply due to its low voltage profile. A saddle point in rectified voltage occurs at class-E, while class-Fi exhibits the poorest performance.

2.3.3   Measurements

A measurement set-up was created at dBm Engineering using a Focus impedance tuner and 2nd and 3rd harmonic tuner (see Figure 2.14 below) to produce measurements comparable to the previous simulation. The MA4E2954 diode was placed in a test fixture and measured at the same frequency and input power level. The fundamental impedance tuner is used to vary the input impedance as desired. A harmonic tuner was capable of presenting, on average, a 0.92 magnitude reflection coefficient at the second and third harmonics. The phase is then variable to a precision better than a degree. The Focus control software is able to adjust the fundamental impedance tuner as the harmonic tuner changes so that the fundamental impedance is always the same. However, the correction is limited and it is not guaranteed that a particular fundamental impedance can be reached for every position of the harmonic tuner without the use of pre-matching. In the present case, pre-matching was not available. As a result, desired fundamental impedances

27
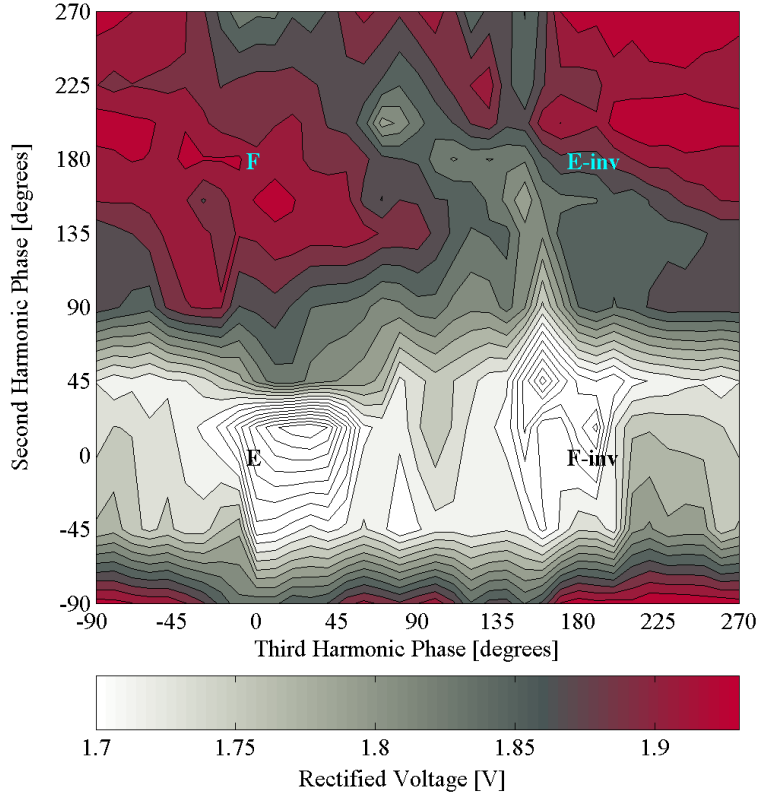
Figure 2.9: Measured second and third harmonic termination phase sweeps for the MA4E2054 diode.

could not be reached for second harmonic phase angles in the rang of -15 to 15°. Therefore the points on the measured phase sweep near class-E and class-Fi (2nd harmonic phase = 0°) are interpolated between -15 to 15°. The rest of the points are separated by 30° for the second harmonic and 30° for the third harmonic.

The results are similar to those of the simulated diode model in Figure 2.8

28

in that the optimal regions occur near the class-F and Ei cases while the poorest performance occurs along the class-E to Fi region.

2.4 Rectifier Source-Pulling

A source-pull measurement or simulation is the name given to the method of sweeping the impedances seen by a device looking back towards the source. As in the previous section, the phase of the harmonic impedances are varied to find optimal rectification performance, the source-pull allows the fundamental impedance to be varied for a particular set of harmonic terminations. In this section, simulated load pulls are demonstrated for a large-signal case to show how the optimal impedance, rectification efficiency, and reflected power reacts to fundamental impedance.

2.4.1 Simulated Source Pulls for the Diode Model

The following figures show the resulting RF–DC efficiency and normalized reflected power $(P_{refl(db)} - P_{in(dB)})$ at the fundamental versus source impedance. In each case, the source impedance is varied using a single-stub matching section as in Figure 2.4. In the following cases, however, the harmonic terminations are maintained using the proper lengths of open transmission line. The operating conditions for these simulations using the MA4E2054 diode are $f = 1\,\mathrm{GHz}$, $P_{in} = 13.2\,\mathrm{dBm}$, and $R_L = 300\,\Omega$.

The voltage and current levels of the waveforms demonstrated in the

29
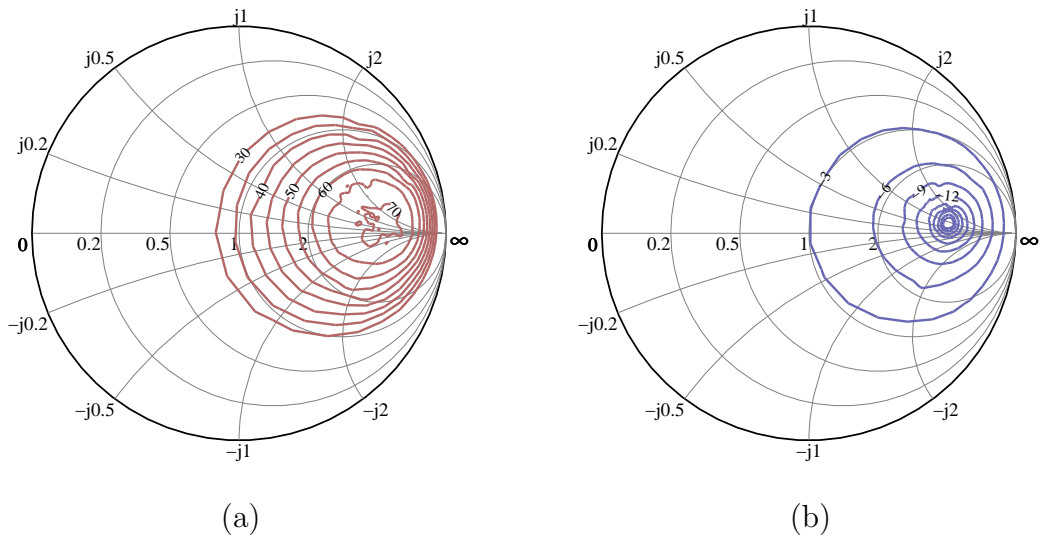
Figure 2.10: Class-F source-pull diagram of RF–DC efficiency (a) and normalized rf reflected power (b).
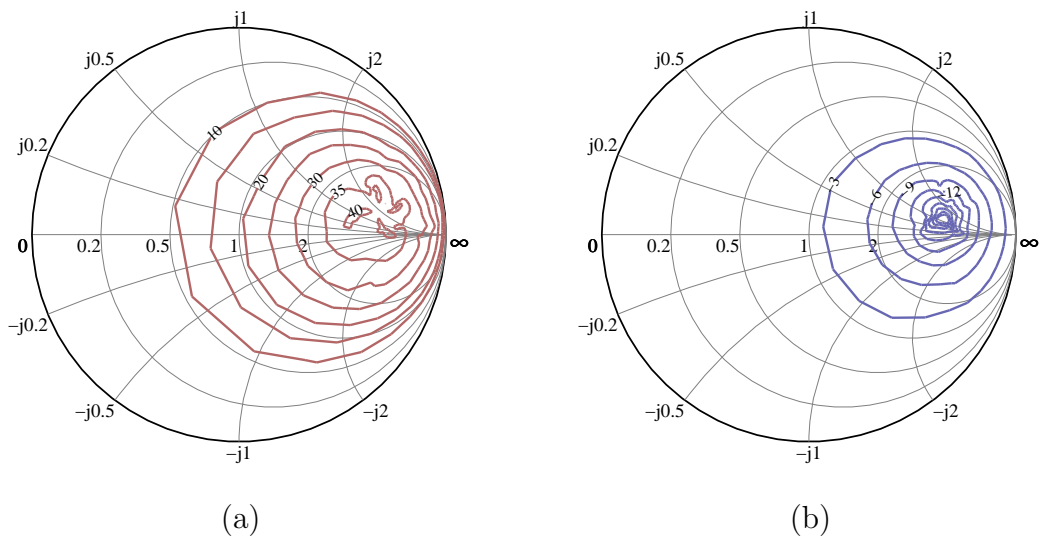
Figure 2.11: Class-E source-pull diagram of RF–DC efficiency (a) and normalized rf reflected power (b).
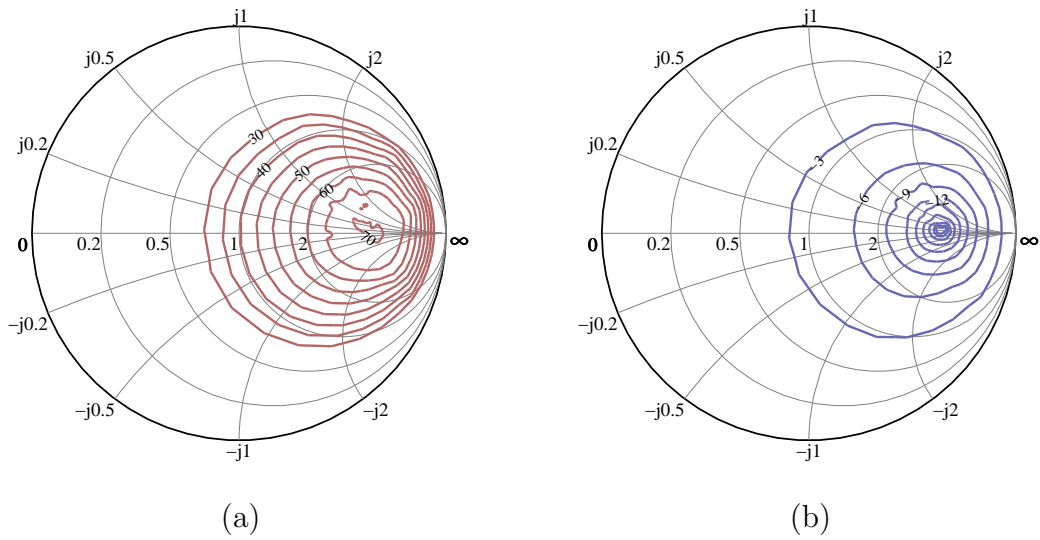
Figure 2.12: Class-Ei source-pull diagram of RF–DC efficiency (a) and normalized rf reflected power (b).
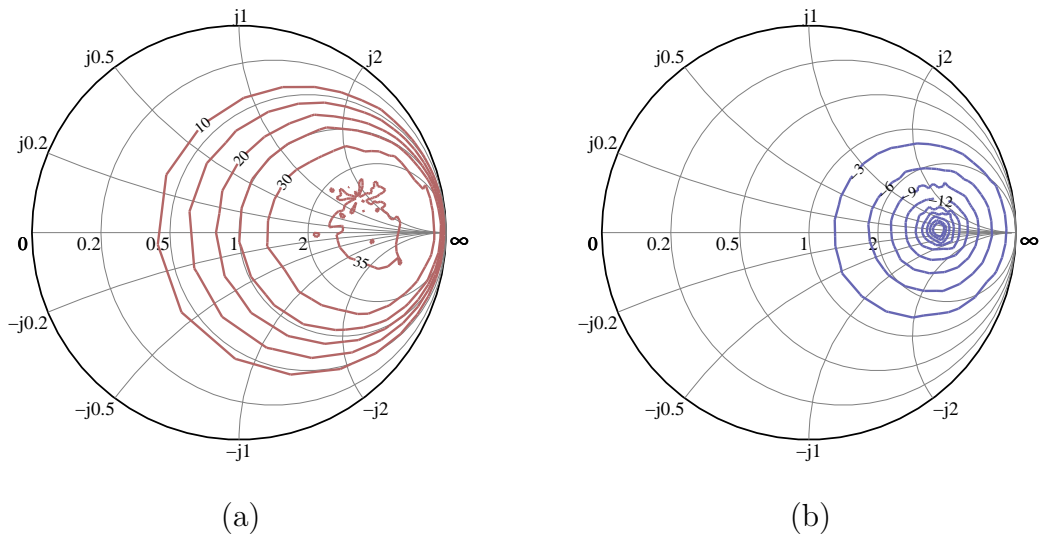
Figure 2.13: Class-Fi source-pull diagram of RF–DC efficiency (a) and normalized rf reflected power (b).

previous section apply for these source-pull diagrams and help explain why the class-E and Fi cases had poorer results. The reverse breakdown voltage for these simulations was 5 V and voltages in excess of this value are the main contributors to loss and low efficiency. In fact, for class-E, the optimal source impedance no longer corresponds to the class-E impedance, but simply to where the diode is best matched in terms of reflection.

2.4.2   Measured Source Pulls

A source-pull measurement system was used on the MA4E2054 diode using the same *Focus Microwaves* measurement system used for the harmonics sweep in Section 2.4.2. The system includes an RF source, passive source-impedance tuner, passive 2nd and 3rd harmonic tuner, and diode test fixture (Figure 2.14) courtesy of dBm Engineering.

Source-pull measurements were taken for several combinations of R_L and harmonic terminations. Graphical results of the class-E and class-F terminated source-pulls are shown in Figure 2.15. The results for each of the four classes are summarized in the next section and compared with simulated values. The same operating conditions (f_o, P_{in}, R_L) were used in the measurements as were used for the above simulated source-pulls.
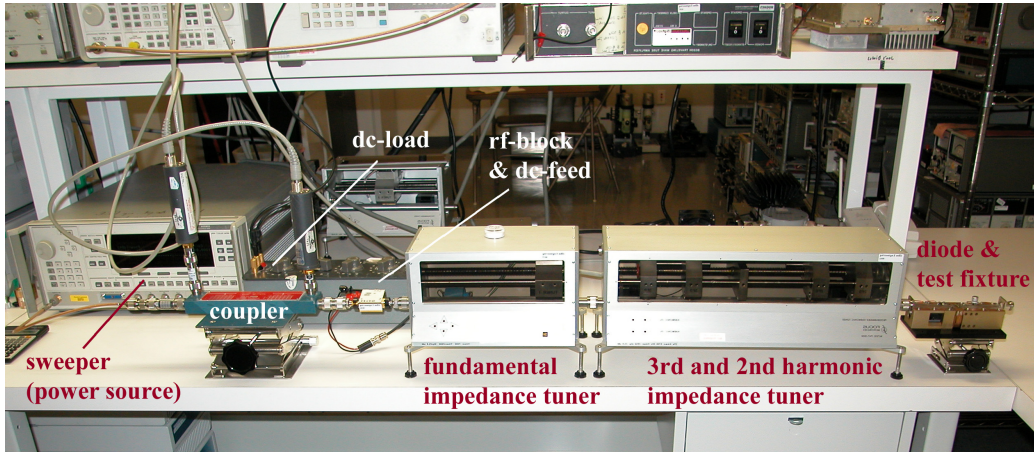
Figure 2.14: Measurement set-up used for the diode source pull with fundamental impedance tuner and second and third harmonic phase tuners. Lab and equipment courtesy of dBm Engineering and Focus Microwaves.

2.5 Switched Mode Rectifier Performance

The performance of four switched-mode rectifiers is summarized and compared with simulated results for the MA4E2054 diode operating at $1\,$GHz with $13.2\,$dBm input power. Subsequently, four microstrip circuit designs are presented as show how each class can be realized outside of the source-pull system.

2.5.1 Comparison of Simulated and Measured Results

The results of the previous simulated source-pulls are summarized in Table 2.2. For each class, the source impedance is chosen based on the optimal rectification efficiency. Not shown in the table is the result of the matched
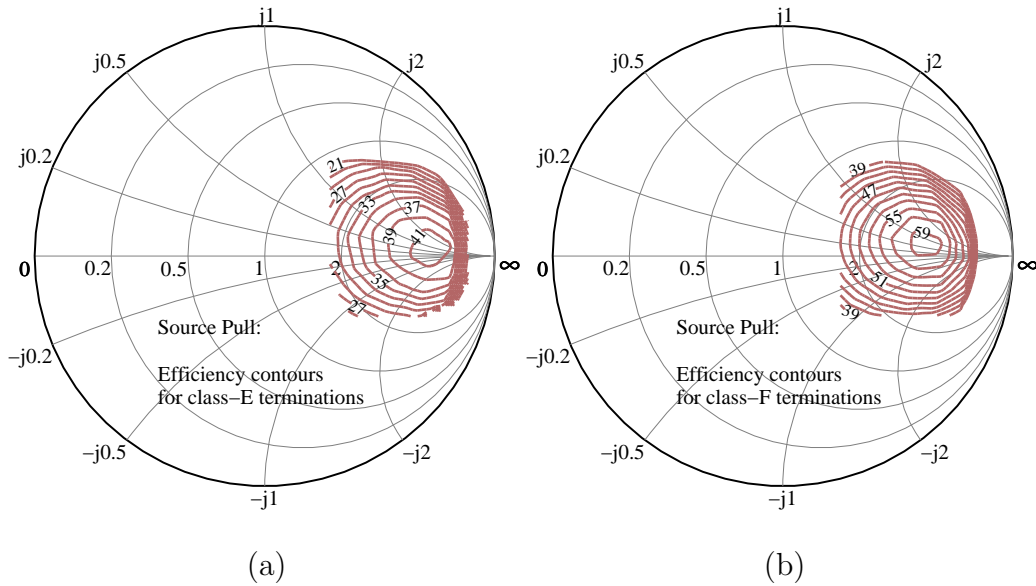
Figure 2.15: Source-pull diagrams for Class-E (a) and class-F (b) terminated diodes showing contours of constant RF–DC efficiency.

diode with no harmonic terminations. By comparison, its simulated maximum efficiency was 49% with an optimal source impedance of $153 + j14\,\Omega$. Similarly, Table 2.3 shows the optimal source impedance for maximum rectification efficiency for each class under the same operating conditions as Table 2.2.

The discrepancies between the measured and simulated rectification efficiencies are mostly due to the poor representation of actual reverse-bias behavior given by the *Spice* model of the MA4E2054. A smaller effect can be attributed to the non-ideal harmonic terminations of the measurement system which led to extra loss in the circuit.

Table 2.2: 1-GHz Rectifier simulated results for special modes

mode	Z_{fund}	Z_{2f_o}	Z_{3f_o}	R_L	η	V_{dc}
	Ω	Ω	Ω	Ω	$\%$	V
class-F	$260 + j82$	0	∞	300	75	2.17
class-E	$235 + j80$	∞	∞	300	39	1.56
class-Ei	$224 + j14$	0	0	300	71	2.11
class-Fi	$223 + j25$	∞	0	300	35	1.48

Table 2.3: 1-GHz Rectifier measurements for special modes

mode	Z_{fund}	Γ_{2f_o}	Γ_{3f_o}	R_L	η	V_{dc}
	Ω	mag/$\angle$	mag/$\angle$	Ω	$\%$	V
class-F	$194 + j25$	$0.95\angle180°$	$0.92\angle\text{-}1°$	300	60	1.93
class-E	$306 + j30$	$0.94\angle17°$	$0.92\angle1°$	300	42	1.61
class-Ei	$193 + j20$	$0.95\angle180°$	$0.91\angle180°$	300	56	1.88
class-Fi	$194 + j20$	$0.94\angle17°$	$0.91\angle180°$	300	44	1.66

2.5.2 Circuit Designs for Switched Mode Rectifiers

Rectifier designs are presented for each of the four classes of rectification mentioned above. The transmission line scheme of terminating the harmonics used in the simulations above are shown below for a putative microstrip circuit. While the given electrical lengths of the open stubs provide exact open and short circuits in simulation, the fringing capacitance and effective propagation constant must be carefully taken into account in practice to achieve the desired impedances at the harmonics. Microstrip implementation should, however, provide greater accuracy than the source-pull system with harmonic tuner.

The method used for fundamental-impedance matching used in the simulation was to use a pre-match single stub section followed by a fine-tuning single stub section. In effect this comprised a double-stub matching section; however, since single stub matching would be adequate, the fundamental-impedance matching scheme is left as a block in Figure 2.16 and Figure 2.17.

Designing impedance matching circuits based on source-pull measurements and method of moments simulations has been successfully carried out and documented in [18] for power amplifiers between 1 and 2 GHz.
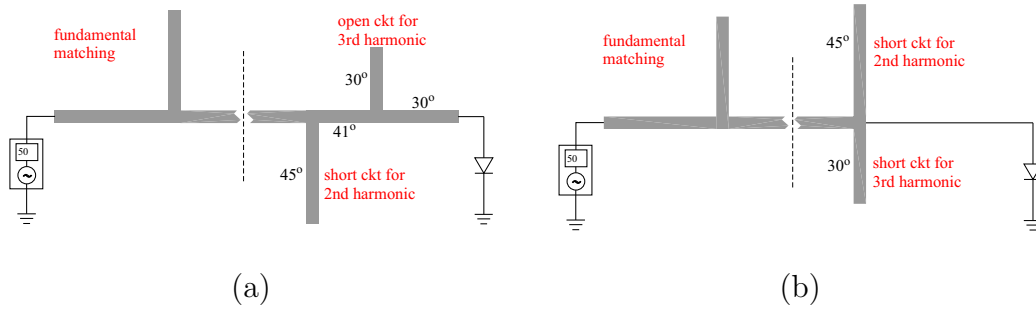
Figure 2.16: Class-F (a) and class-Ei (b) circuit layouts demonstrating possible harmonic termination schemes in microstrip form. Line dimensions are given in electrical length referenced to the fundamental frequency.
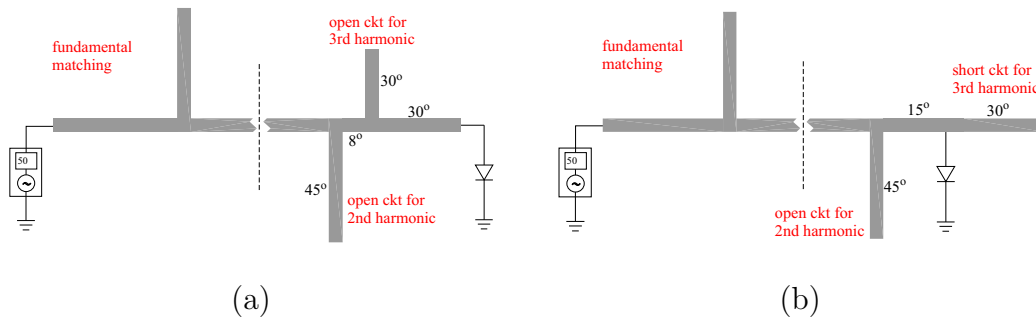
Figure 2.17: Class-F (a) and class-Ei (b) circuit layouts demonstrating possible harmonic termination schemes in microstrip form. Line dimensions are given in electrical length referenced to the fundamental frequency.

Chapter 3

RF Energy Recycling:

A Broadband Rectenna Array

3.1 Introduction

Rectification of microwave signals for supplying dc power through wireless transmission has been proposed and researched in the context of high power beaming since the 1950s, a good review of which is given in [19]. In microwave power transmission, the antennas have well-defined polarization and high rectification efficiency enabled by single-frequency, high microwave power densities incident on an array of antennas and rectifying circuits. Applications for this type of power transfer have been proposed for helicopter powering [19], solar-powered satellite-to-ground transmission [8], inter-satellite power transmission [20] including utility power satellites [21], mechanical actuators for

space-based telescopes [9], small dc motor driving [22], and short range wireless power transfer, e.g. between two parts of a satellite. Both linear [23],[24] dual-linear [9],[25] and circular polarization [8], [26] of the receiving antennas were used for demonstrations of efficiencies ranging from around 85–90% at lower microwave frequencies to around 60% at X-band and around 40% at Ka-band [21].
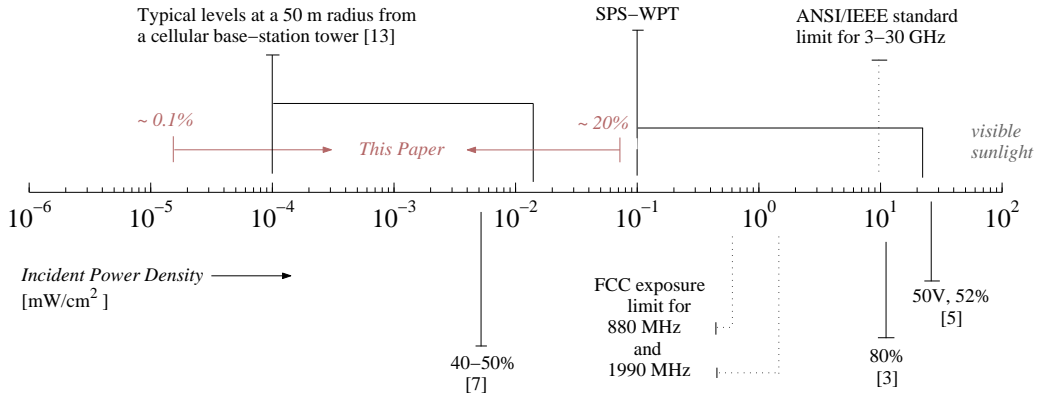
Figure 3.1: A diagram of various microwave power sources and their typical power density levels. The power density operating points of several rectenna designs found in the literature and their s corresponding efficiencies [23, 20, 9]. Also shown is the range of expected power densities used in the Solar Power Satellite (SPS) and Wireless Power Transmission (WPT) applications. The range of power densities measured in this paper is also shown for comparison. Measured ambient levels in our lab. are in the 10^{-6} to 10^{-5} mW/cm^2 range.

In the above referenced work, rectification was performed for narrowband, essentially single-frequency, incident microwave radiation with relatively high power densities. A survey of the typical power densities associated with high-power rectennas is given in Figure 3.1, in which three examples are taken from

[20],[9], and [23] along with the corresponding operating rectification efficiencies. Also shown in the figure are expected power densities near a typical base station tower operating at 880 and 1990 MHz [27]. Concerns have been expressed in terms of possible health hazards [28]. In [23], rectification of low power levels was discussed for battery-free transponders, with power densities on the order of 10^{-2} mW/cm^2. More recently, broadband rectification of very low-power incident radiation (less than 1 mW/cm^2) was demonstrated in [29]. This paper focuses on incident power densities and input power levels that are orders of magnitude lower than those associated with the projects in the literature cited above.

In this paper, simulation, design and performance of a broadband rectenna array (tested from 2–18 GHz) for rectification of comparatively low-power (10^{-5} to 10^{-1} mW/cm^2), arbitrarily polarized incident radiation is presented. The work is motivated by two types of applications: powering of low-power sensor networks and rf energy recycling. Because of the low input power levels, a nonlinear decrease in efficiency is expected when compared to power beaming applications. The goal of this paper is to determine the usefulness of low power rectification.

The general block-diagram of the rectenna array discussed in this paper is shown in Figure 3.2. Multiple sources of different frequencies are radiating power in all directions in a rich scattering environment. The DC powers from many rectenna elements are added by current and voltage summing with a
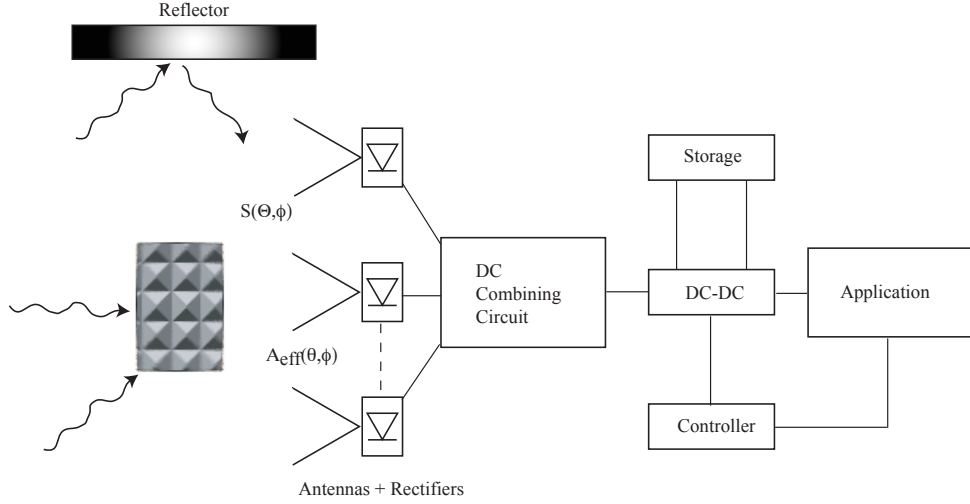
Figure 3.2: Block diagram of a rectenna array for ambient energy recycling. Waves of different frequencies and power levels propogate through a complex environment before they are received by a dual-polarized array of antennas. Each element in the array is integrated with a rectifying device. The resulting DC outputs are combined and fed to energy management electronics.

conversion efficiency

$$\eta = P_{DC}/P_{RF} \qquad (3.1)$$

which is a function of statistically varying incident RF power, $\eta = \eta(P_{RF})$. The received average RF power over a range of frequencies, at any instant in time is given by

$$P_{RF}(t) = \frac{1}{f_2 - f_1} \int_{f_1}^{f_2} \int_0^{4\pi} S(\Omega, f, t) A_{eff}(\Omega, f) d\Omega df \qquad (3.2)$$

where Ω is the solid angle in steradians and $S(\Omega, f, t)$ is the time varying frequency and angle dependent incident power density. A_{eff} is the angle,

frequency, and polarization dependent effective area of the antenna. The DC power at a single frequency, f_i, is given by

$$P_{DC}(f_i) = P_{RF}(t, f_i)\eta[P_{RF}(t, f_i), \rho] \tag{3.3}$$

where ρ represents the diode mismatch to the antenna. Because of the nonlinearity of the diode, the mismatch is dependent on power as well as frequency.

The issues related to low-power arbitrarily-polarized reception, rectification and power management are addressed in this paper as follows:

- Section 3.2 discusses rectification of low power microwave signals. Nonlinear simulations of the rectifying device are confirmed with source-pull measurements over a broad frequency range and broad range of input powers. The result is a range of RF impedances presented to the diode for optimal rectification efficiency.

- Section 3.3 discusses design of an antenna integrated with a rectifier. Electromagnetic field simulations are coupled to nonlinear circuit simulations to ensure optimal broadband match between the antenna and rectifier. Based on known range of input power levels, a rectifier diode is chosen among several candidates. Measurements on single antenna elements are compared to analysis results.

- Section 3.4 describes the design and characterization of a 64–element dual circular polarized rectenna array. The frequency response, receive radiation patterns, DC power rectification efficiency, and radiated harmonics are measured. Finally, given the statistical nature of incident RF

radiation, the DC rectified power was measured over 10,000 trials with varying frequency and power.

- Section 3.5 presents a discussion on storage and management of the extracted DC power with two example applications.

3.2 Microwave Rectification and the Rectenna

At low RF frequencies (kHz to low MHz), both pn-diodes and transistors are used as rectifiers. At microwaves (1 GHz and higher), Schottky diodes (GaAs or Si) with shorter transit times are required. In the present case, we have chosen silicon based on availability, low-cost, and simulated performance. Similar to low-frequency, high-power applications, the diode is driven as a half-wave rectifier with an efficiency limited to

$$\eta_{max} = \frac{1}{1 + \frac{V_D}{2V_{out}}} \tag{3.4}$$

where V_{out} is the output DC voltage and V_D is the drop across the conducting diode. In this work it is more appropriate to measure the efficiency defined by Equation 3.1 which includes the loss due to reflected power.

For low power applications, as is the case for collected ambient energy, there is generally not enough power to drive the diode in a high efficiency mode. Furthermore, rectification over multiple octaves requires a different approach from standard matching techniques. In a rectenna application,

the antenna itself can be used as the matching mechanism instead of using a transmission-line matching circuit as in [21]–[26]. The antenna design is therefore heavily dependent on the diode characteristics. The following section presents various techniques for analyzing diode operation at microwave frequencies. The results are then used to design the antenna and integrated rectenna for relevant ambient power levels.

3.2.1   Analysis and Design Method

A useful time domain analysis has been applied by McSpadden et al. in a number of papers dealing with single-frequency rectennas at microwave frequencies up to *Ka*-band [21]. The method uses current/voltage properties of the diode as a basis for predicting rectified power levels and conversion efficiencies. The method has proved a successful predictor of conversion efficiencies over a broad range of incident power levels and load impedances. In general this approach has been used for well filtered, well matched diodes integrated with antennas for narrowband use.

Several properties of the diode at microwave frequencies require a more comprehensive frequency domain approach: (1) The nonlinear capacitance of the diode needs to be taken into account past a few GHz for most devices. (2) Reflected harmonic energy from the source or load side of the diode can alter the voltage across the diode. (3) The diode also begins to bias itself as it produces more DC current, thus moving the DC operating point of the *IV* curve in a nonlinear fashion.

Certain qualities of microwave rectification can be visualized best in the time domain, i.e. monitoring the complex waveform across the diode. In the frequency domain, the Harmonic Balance (HB) method of analysis presents a more comprehensive treatment of the multi-spectral diode problem. Though less helpful diagnostically and heavily dependent on the accuracy of the non-linear model of the diode, HB provides a tool for addressing all previously mentioned aspects of microwave rectification. The method intrinsically takes into account the DC component and a specified number of harmonics, while allowing the ability to specify the source impedance and harmonic terminations.

3.2.2 Diode Source-Pull

A source pull of the diode is a sweep of RF input source impedance values over a given area of the Smith chart. Figure 3.3 (a) shows the HB simulation approach using Agilent ADS as well as the measurement approach using impedance tuners. In both simulation and measurements, for a variety of input powers the resulting DC voltage is quantified for each source impedance and plotted on the Smith chart as shown in Figure 3.4. The region of optimal source impedance is later used for optimizing the antenna design so that the antenna presents an equivalent source impedance to the diode. In the simulation an assumption must be made for the impedance seen by the reflected harmonics, and in the presented case this impedance was set to the impedance of a broadband, self-complementary antenna, $189\,\Omega$.
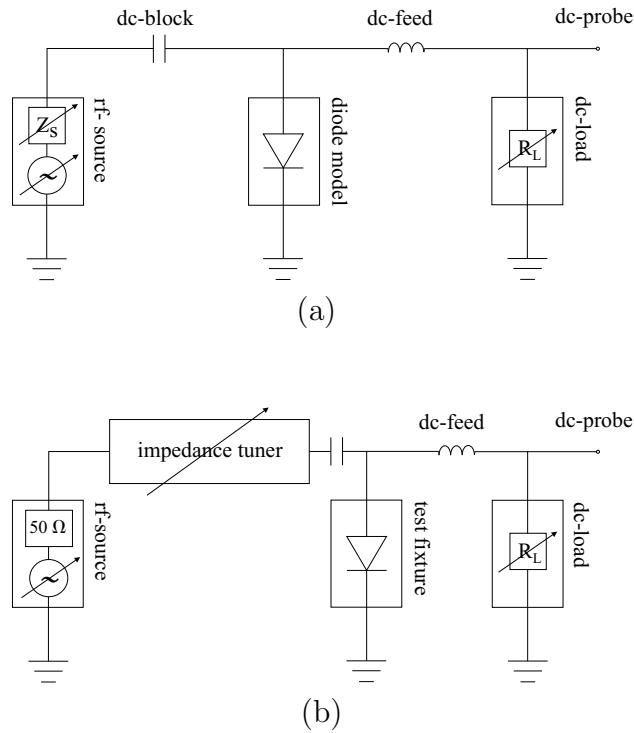
Figure 3.3: Circuit diagram of the Harmonic Balance simulation (a) and diagram of the equivalent source-pull measurement setup (b).

Figure 3.4 demonstrates the range of optimal source impedances across the range of 1 to 16 GHz and -30 to 10 dBm input power. The magnitude of the optimal source impedance becomes smaller with increasing incident power. The same occurs as the DC load approaches the optimal value, however the effect is not as dramatic. More significantly, the optimal source impedance moves counter-clockwise along a constant admittance circle with increasing frequency due to the junction capacitance.

The Smith chart plots of Figure 3.5 show a comparison between a simu-

46
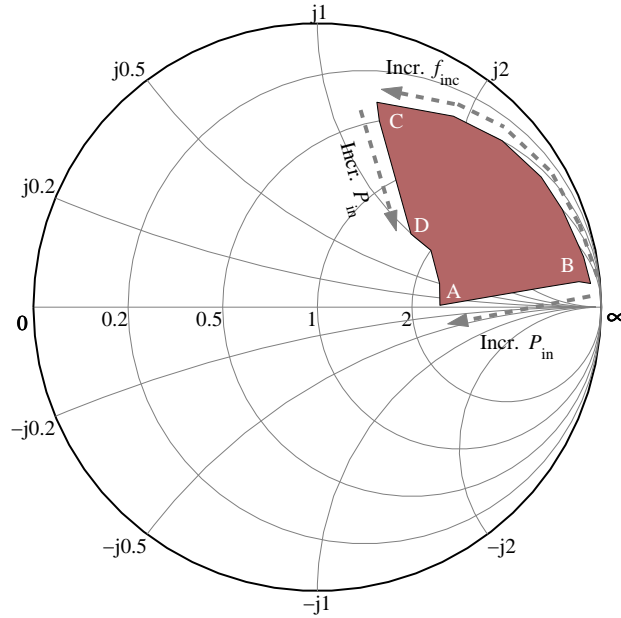
Figure 3.4: Simulated range of optimal source impedances for the SMS7630 Schottky diode as the frequency (f_{inc}) and input power (P_{in}) are varied. Within the shaded area, region A corresponds to high input power and low frequency, region B corresponds to low power and low frequency, etc.

lated source-pull using HB and measurements using a source-pull/load-pull measurement system. A Focus 9-GHz coaxial tuner was used in the measurement setup as described in Figure 3.3 (b).

3.3   Broadband Rectenna Design

Given the good agreement between simulation and experiment, HB was used to evaluate several diodes. The rectification performance is seen to depend most significantly on saturation current, junction capacitance, built-in po-
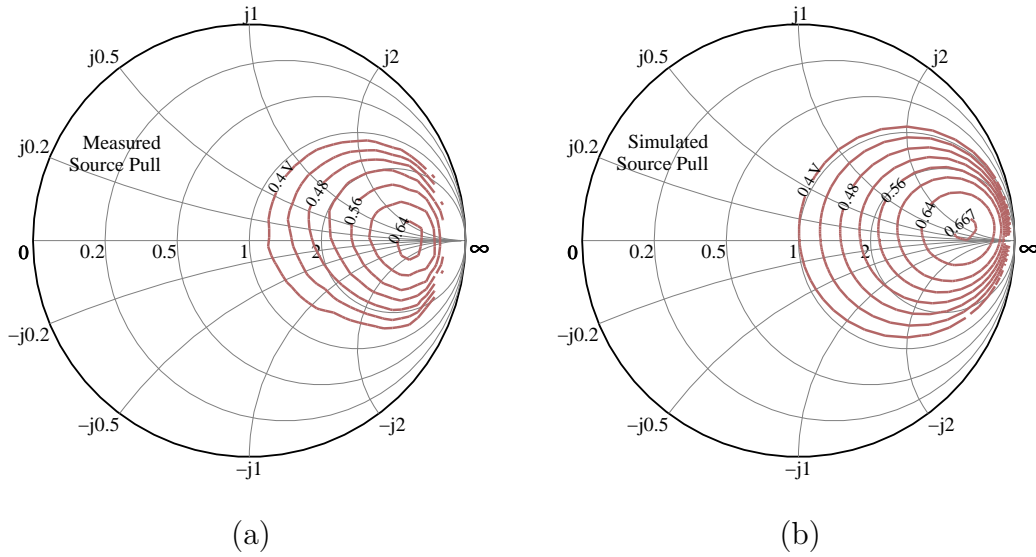
Figure 3.5: Measured (a) and simulated (b) source-pull of the MA4E2054 diode at 1 GHz. The contours show constant levels of DC voltage over source impedance with constant RF input power.

tential, and series resistance. Figure 3.6 shows qualitatively the efficiency performance of three different Schottky diodes obtained by HB simulations. Based on these results the Alpha Industries SMS7630-079 zero-bias device was selected.

3.3.1 Integrated Rectenna Analysis

In most rectenna designs the narrowband antenna is used to feed a transmission line followed by space-consuming, traditional matching and filtering sections. In contrast, in the work presented here the diode is integrated directly into the antenna. Consequently, the antenna is called upon to provide
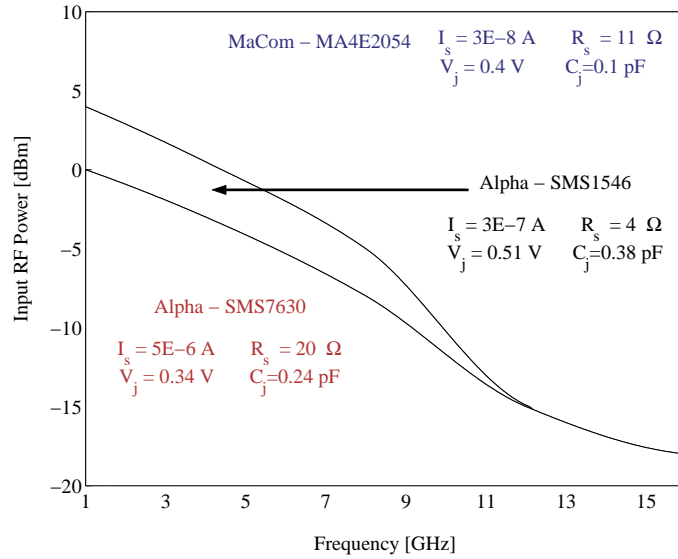
Figure 3.6: Simulated qualitative comparison for three commercially available diodes. This plot shows which diode will have optimal efficiency for a given power and frequency. For the low power region, the Alpha SMS7630 performs best over the frequency range.

both matching and filtering of the output signal, reducing the required area and increasing the bandwidth. The antenna is included in the HB simulation as the internal impedance of the power source used to drive the circuit. This Thévenin equivalent model allows use of measured or simulated S-parameters in the rectenna simulation Figure 3.3 (a).

3.3.2   The Spiral Antenna

As seen in the previous section, the major problem in broadband rectenna design lies in the nature of the antenna and diode frequency dependent
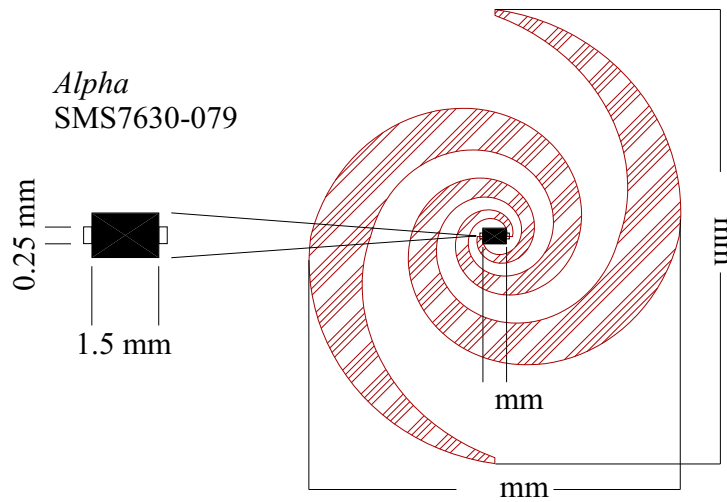
Figure 3.7: Layout of the spiral antenna element with a packaged Schottky diode connected directly at the feed. The size of the package limits the upper frequency for this broadband antenna, while the overall size limits the low frequency limit.

impedance. For maximal power transfer, the antenna impedance would match the optimal diode impedance for all frequencies. Our approach is to present a constant impedance to the diode by using a frequency independent antenna element.

The equiangular spiral is chosen for its convenient feed point where the diode can be connected. A spiral with dimensions shown in Figure 3.7 was designed using full wave MoM simulations with Ansoft *Ensemble* and Zeland *IE3D* and has a measured frequency response shown in the Figure 3.8 (a). The following measurements characterize the extent to which this spiral rectenna achieves favorable rectification over a multi-octave band.

Figure 3.8 (b) shows the frequency dependence of the rectified voltage for
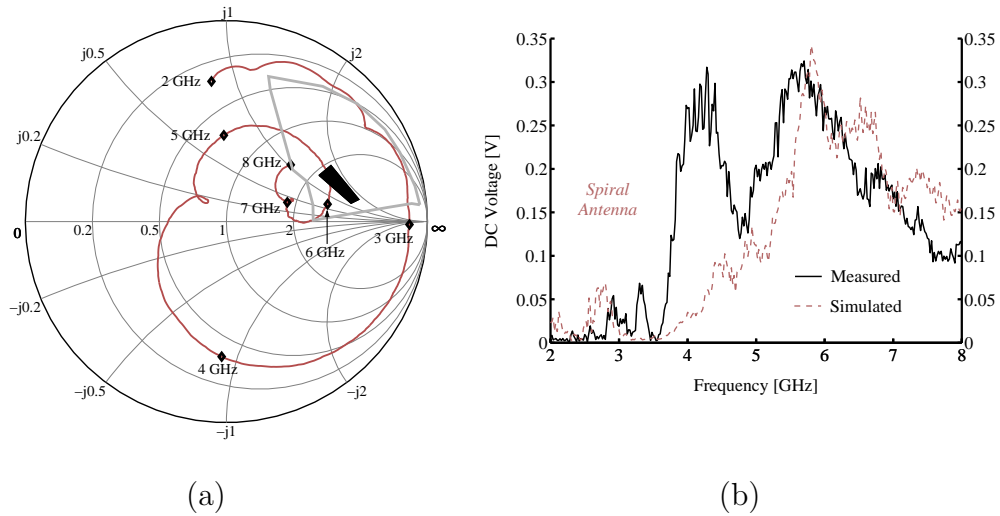
Figure 3.8: (a) Simulated *S*-parameters of the spiral antenna along with optimal diode source impedance from 2 to 8 GHz. (b) Resulting HB simulation and measurements of the DC rectified voltage response across a 600 Ω load.

approximately 0 dBm input to the diode. The disagreement at around 4 GHz is beleived to be caused by a resonance in the unbalanced coaxial feed. Therefore, an idependent validation for the simulation method was performed on a well characterized Vivaldi tapered slot antenna with a balanced antipodal feed [30]. In this case the nonlinear simulation and measured performance agree closely (Figure 3.9).

51
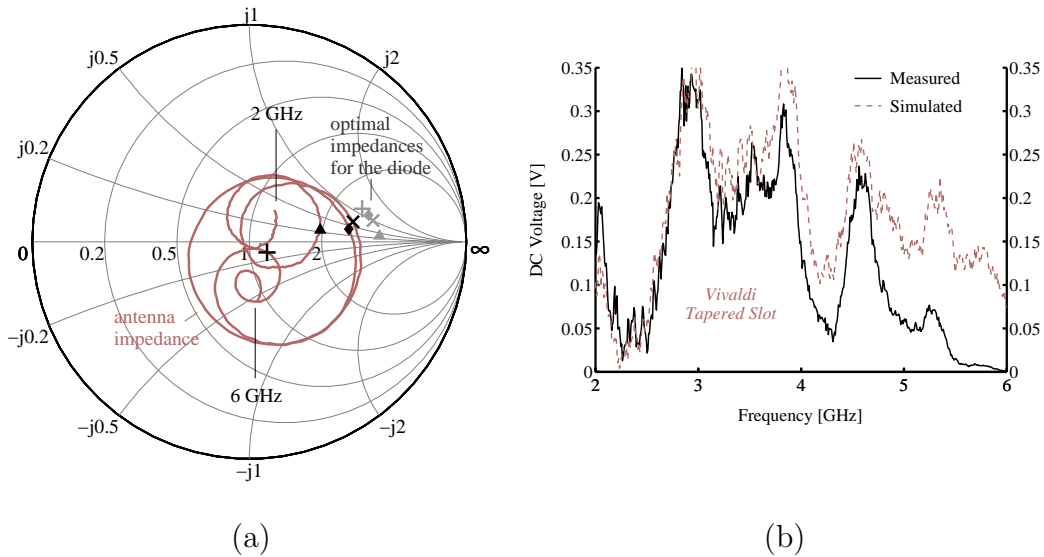
Figure 3.9: (a) Measured S-parameters of the Vivaldi tapered slot with balanced feed along with markers at the optimal diode source impedance coincident with peaks in the frequency response. (b) Simulated and measured rectified voltage across a $600\,\Omega$ load as a function of incident RF frequency for the Vivaldi tapered slot.

3.4 Performance of a Broadband Rectenna Array

The previously characterized spiral rectenna is chosen as the element of a 64-element array with a goal of increasing the effective area and therefore the rectified power as described by Equation 3.3. There are a number of additional effects and performance aspects that differ from standard array theory. Here the rectenna array is composed of individual spiral elements, each with a separate rectifier. In the present case, the rectenna array is

composed of individual spiral elements, each independent rectifiers. The fundamental property of such an array is that the energy is rectified at each element, and the DC voltages are subsequently combined. The radiation pattern for a single element at a single frequency incident wave measured at DC can be defined as

$$G_{DC}(\theta, \phi) = \eta(P_{RF}) \frac{4\pi \cdot P_{RF}}{S(\theta, \phi) \lambda^2} = \eta(P_{RF}) G(\theta, \phi) \qquad (3.5)$$

where $G(\theta, \phi)$ is the RF radiation pattern. The *DC radiation pattern, G_{DC},* is different from the RF radiation pattern due to the nonlinear dependence of efficiency on RF power. The resulting pattern obtained by measuring the DC voltage across an optimal load exhibits lower gain at larger angles θ and ϕ. The radiation pattern for the n-element array is given by

$$G_{DC}^n(\theta, \phi) = \kappa(P_{RF}) G_{DC}(\theta, \phi) \qquad (3.6)$$

where κ is a function of incident RF power and DC combining circuit. To first order, κ is not a funtion of incidence angle.

3.4.1 Array Design

Figure 3.10 depicts the compact element spacing. At lower frequencies the increased mutual coupling between elements and the presence of the bias lines increases the power delivered to the diodes by effectively increasing the effective aperture of each element. The problem of polarization perfor- mance is addressed by alternating left and right circular polarization between

neighboring elements, and by an additional rotation by 90° from element to element. This means that the array suffers an average 3 dB input polarization loss for *every* possible polarization of the incident energy. However, this strategy ensures a flat polarization response.
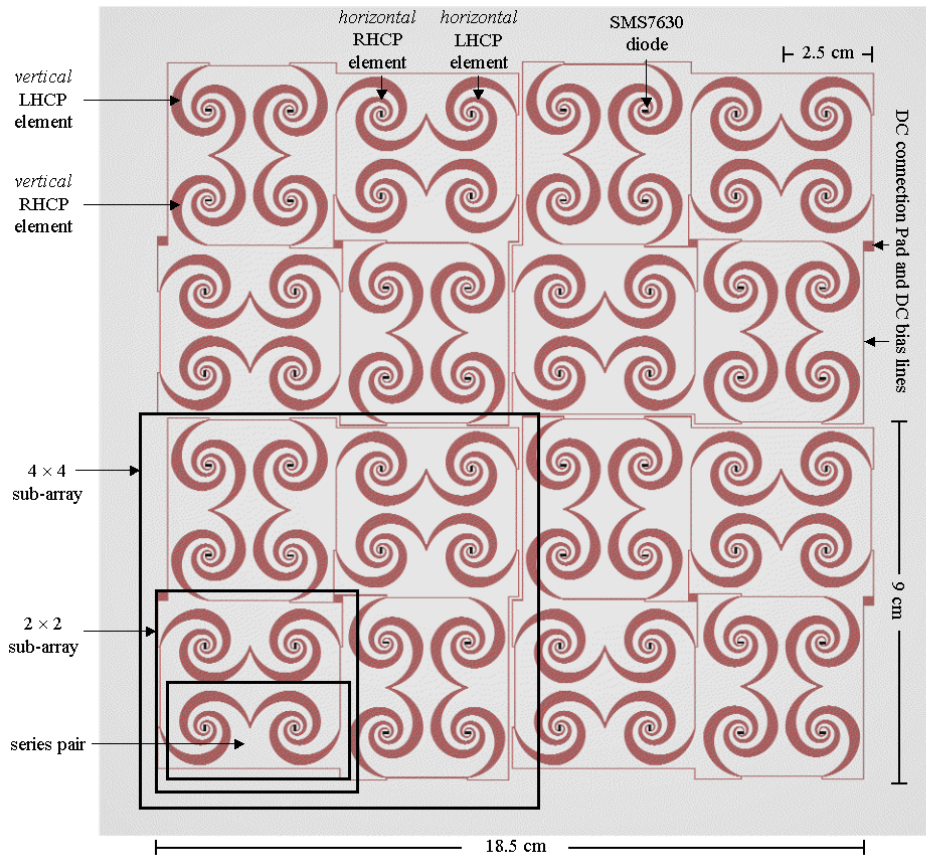
Figure 3.10: Diagram of the 64-element array. Received RF power is rectified at each spiral locally and the combined DC power for all elements is extracted using two bias lines at the edges of the array (not shown). A number of possible DC connections and their effect on efficiency are described in the text.

The crucial design step for the array is to acheive optimal DC combining efficiency. Previous work shows that predominately parallel connections (current-summing) lead to smaller matched loads for the rectenna [31]. For a series connected array (voltage-summed), the matched load is much higher. This can be seen by reducing the array to a combination of DC Thévenin sources where the matched load corresponds to the total source resistance. The nonlinear performance of the diodes must again be considered when considering the DC connections. Increased current or voltage in a predominately series or parallel-connected array can lead to over-biasing of the individual diodes such that the rectification process is uniformly degraded over the array. Furthermore, the DC power level is very sensitive to under illumination. For these reasons, the 64 element array was connected using 2×1 parallel pairs connected in series to form a 2×2 sub-subarray: four of these are connected in parallel to create a 4×4 subarray: four more of these are then left as units to comprise the 8×8 array with reconfigurable connectivity.

3.4.2 Frequency Response

The frequency dependence is measured in two ways: three-dimensional patterns are integrated from 2 to 8 GHz where sufficient power was available for the measurement. Since the radiation patterns are reasonably smooth, only the broadside frequency response was measured. Higher input powers were used for 2 to 8 GHz and a low power level was used for the broad range from 2 to 18 GHz. The broadside frequency response was also measured using a

uniform incident power density to synthesize constant input power to the diodes. The results for three input power levels are shown in Figure 3.11.
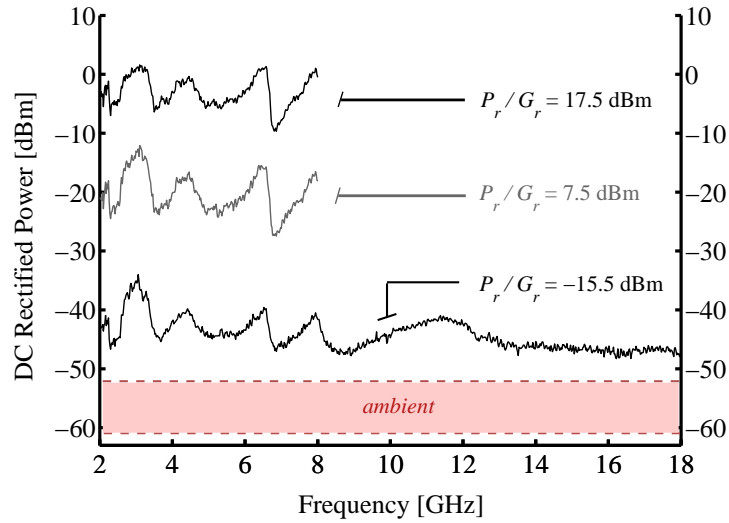
Figure 3.11: Measured broadband frequency response for various incident power levels related to the power density, S, by $P_r/G_r = S\lambda^2/(4\pi)$. The shaded area represents the range of rectified power levels resulting from ambient RF background signal present in the building.

3.4.3   DC-Power Response and Radiated Harmonics

To gain a better understanding of the nonlinear power dependence of the rectenna, a sweep of the input power is performed and the resulting DC output and reradiated power is quantified (Figure 3.12). The measurement is made with broadside linearly polarized radiation at $3\,\mathrm{GHz}$ with incident power densities ranging from tens of nW/cm^2 to 0.1 mW/cm^2. The reradiated energy is measured with a second antenna placed at broadside on the

Table 3.1: Rectification efficiency for a 2×2 sub-array and the 8×8 array with three DC-connection schemes for a *low* and *high* incident power density. Quartiles are defined as the 4×4 subarrays.

power density [mW/cm^2]	2×2 2 in series, 2 in parallel	8×8 2 in series, 2 in parallel	8×8 quartiles all in parallel	8×8 quartiles all in series
$S = 6.2 \cdot 10^{-2}$	0.4%	16%	20%	13%
$S = 6.2 \cdot 10^{-4}$	0.03%	1.1%	2.3%	0.95%

opposite side of the rectenna. The DC is extracted with bias lines and measured across a $100\,\Omega$ load. The rectification efficiency reaches the 20% range for an incident power density of 0.1 mW/cm^2 and arbitrary polarization.

Also shown in the plot is the relative amount of reflected power along with the radiated power of the 2nd through 5th harmonics. The reflected power is found from a time-gated S_{11} measurement using a vector network analyzer. The result, consistent with simulation results, indicates that the reflected varies linearly with input power up to $0.1\,\text{mW/cm}^2$. Simulations suggest, however, that the reflections begin to drop as higher power levels are applied (as more incident power becomes converted to DC and harmonics).

For different DC connections the diodes across the array are biased at different quiescent points on the diode IV curve. Table 3.1 shows efficiency measured across a $600\,\Omega$ load for a 2×2 sub-array and the 8×8 array with three DC-connection schemes for a *low* and *high* incident power density. Quartiles

are defined as the 4×4 subarrays. For this array the parallel configuration of the subarrays gave the highest efficiency over the range of incident power densities.
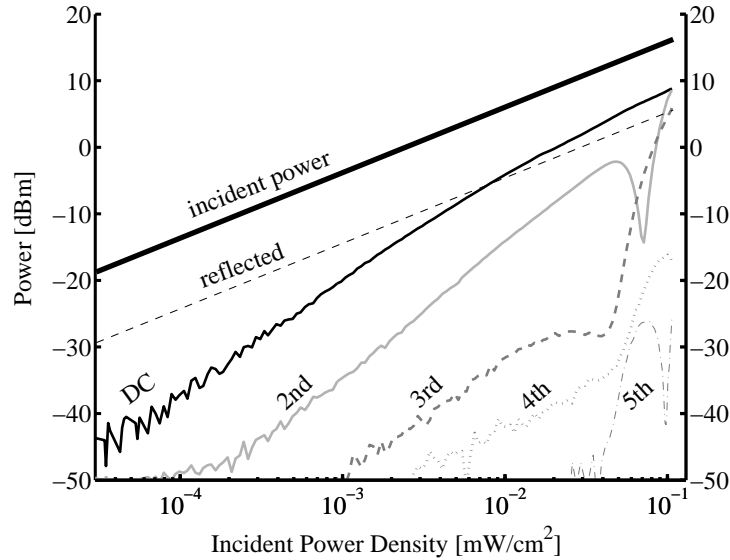
Figure 3.12: Measured reflected, rectified, and reradiated harmonic power as a function of incident power density. The measurement was performed at 3.4 GHz.

3.4.4 DC Receive Patterns and Polarization

The radiation patterns of the rectenna array are found by measuring the output DC rectified power over a hemisphere sampled at 1012 points, Figure 3.14 (a) and Figure 3.14 (b). These patterns are a superposition of the response to two orhtogonally linearly polarized incident waves. At higher frequencies the spiral element is predominately circularly polarized. In order

to design a broadband array with as uniform a pattern in space and polarization as possible, RHCP and LHCP spirals were alternated in the layout. The planar layout of the array places certain limits on the polarization and reception at azimuth angles. Figure 3.14 (a) and Figure 3.14 (b) show that the radiation pattern has low directivity and is similar to that of a single element. Note that the size of the array is $1.5\,\lambda_o^2$ at $2\,\text{GHz}$, and $116\,\lambda_o^2$ at $18\,\text{GHz}$. However, by observing the patterns in Figure 3.14 (a) and Figure 3.14 (b) it is seen that the array receives from all directions over a broad frequency range.
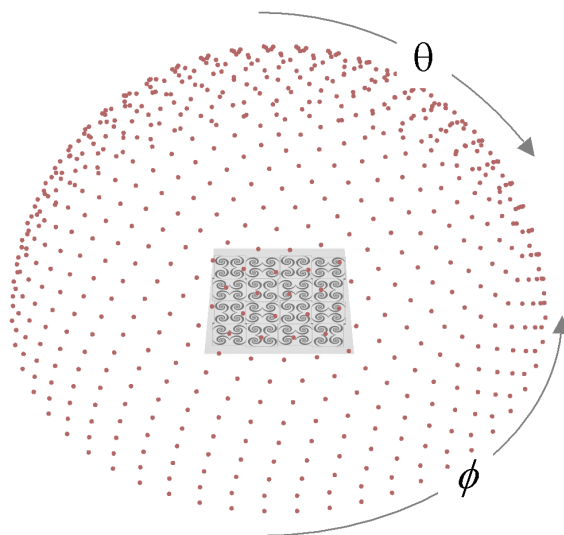
Figure 3.13: Sampled points over a hemisphere indicating angle of illumination for the DC receive patterns of Figure 3.14.
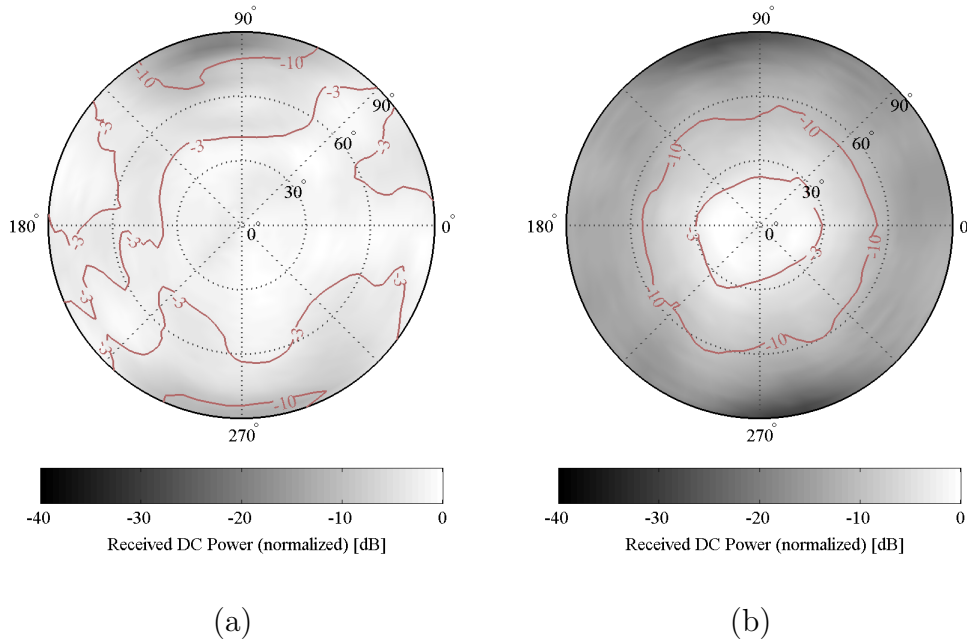
Figure 3.14: Measured DC Power as a function of angle of incidence over a hemisphere for two orthogonally linearly polarized input waves at $2\,\mathrm{GHz}$, (a), and $4.6\,\mathrm{GHz}$, (b). The pattern is related to an RF radiation pattern through Equation 3.5 and Equation 3.6.

3.4.5 A Statistical Study of Multitone Performance

As a final test, the array is placed in a controlled, multitone environment. The point of this test is to demonstrate how the DC response improves or degrades when more waves of more than one frequency are incident simultaneously. Two signal sources, separated by $20°$ in incidence angle from the rectenna and $45°$ in polarization, are used to represent multiple inputs with variable frequency and power. In order to ensure uncorrelated input waves, paired frequencies and power levels are generated randomly with a uniform

distribution using *Matlab*.

The experiment is run by first generating one randomized frequency between 2 and 8 GHz and one incident power level between approximately $0.1\,\mu\text{W/cm}^2$ and $0.1\,\text{mW/cm}^2$. Each source is turned on separately to record the independent DC rectified powers. Both sources are then turned on simultaneously and the new rectified power recorded. This process is repeated for 10,000 randomized input pairs. The sums of the two independent rectified powers for each trial were then sorted and compared with the corresponding rectified power from the simulataneous illumination from both sources.
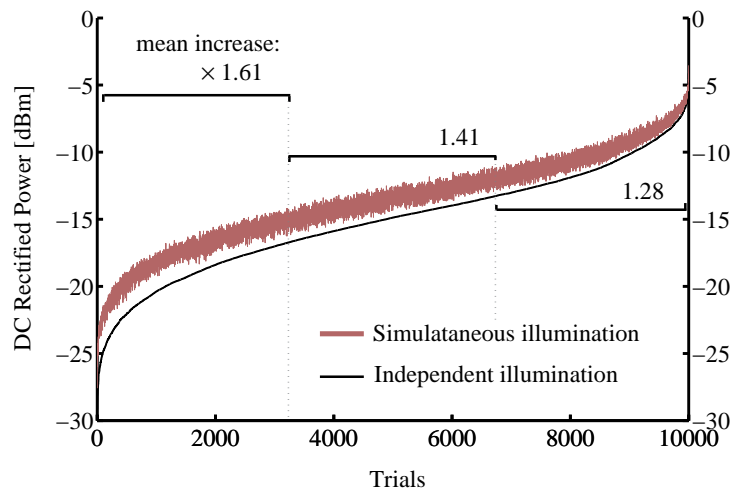
Figure 3.15: Comparison of total recitified power for independent and simultaneous dual-frequency illumination as explained in Section 4 E. The results of 10,000 trials are rank-ordered by DC power to illustrate the power dependent increase in rectification efficiency.

The result (Figure 3.15) reveals the phenomenon that the independent

sources combine nonlinearly, when simulataneously incident, to produce *more* rectified power in *every* instance. The amount of power increase (P_{simul}/P_{indep}) when both sources are on correlates roughly with the amount of rectified power when both sources are off. This correlation is much stronger than the frequency or incident power correlation. For this reason, Figure 3.15 was plotted according to P_{indep}. Also shown is the mean increase in power for three portions of the curve.

It should also be noted that in general, the power-increase diminishes as the two frequencies approach one another. Furthermore, local power-increase minima occur for certain difference frequencies, i.e. $|\Delta f|$. This is thought to be due to a spiral input impedance which efficiently radiates the difference frequency rather than further rectifying the energy. A map of simultaneous illumination power increase is show in Figure 3.16 for frequencies over 2 to 8 GHz with constant P_r/G_r.

3.5 Energy Storage and Management for Low Power Applications

To summarize, a study of rectification of broadband statistically-varying rf radiation is presented in this paper. The experimental results show that the combined electromagnetic field analysis for the radiating element and harmonic balance nonlinear circuit simulations result in predictable rectenna performance. The work focuses on arbitrary polarized low incident power
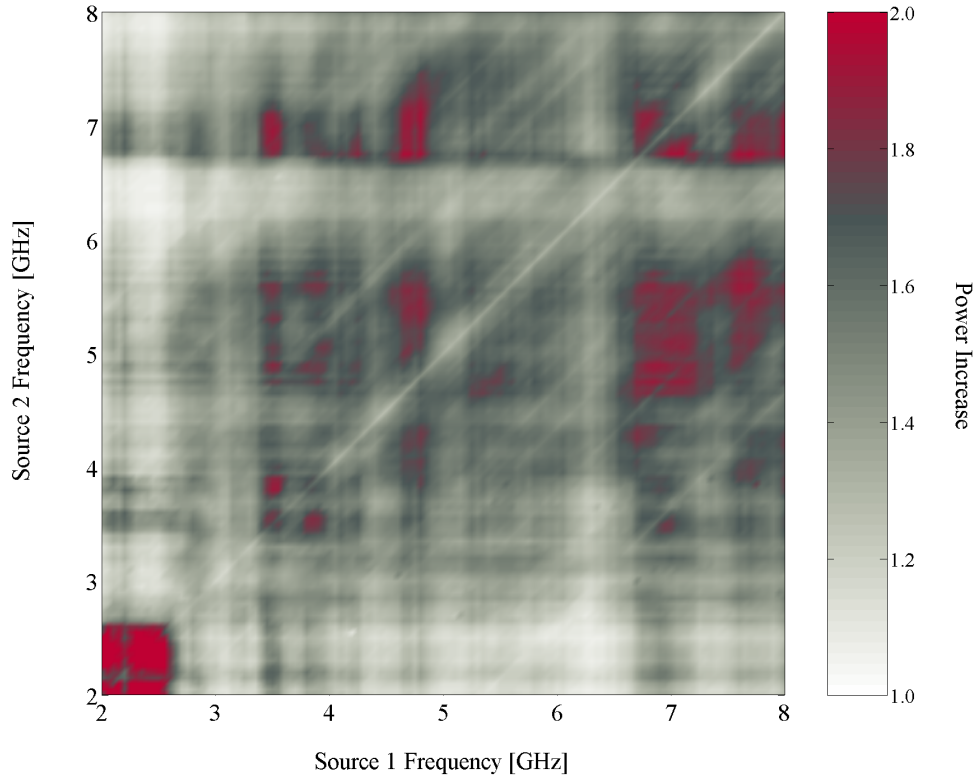
Figure 3.16: Psuedocolor representation of the power increase of simultaneous illumination over the independently summed case. In this plot, the x and y-axis represent the frequency of each of the two transmitters while the P_r/G_r ration for each was kept constant.

density reception and rectification and shows that rectification efficiencies with average 20% over time, frequency and polarization are achieved. If one of these requirements is relaxed, i.e., high-power, narrowband, linearly-polarized and/or time-constant power is transmitted, higher efficiencies up to 60% at X-band [21] can be expected. The motivation for considering

the low-power random case are applications in ambient energy recycling and low-power batteryless sensors.

The first type of application addresses using otherwise wasted power, which in some cases can also help reduce health hazards. For example, the rooftops of buildings in city centers are often leased to a number of wireless providers and technical staff has reported health problems when servicing a transmitter in the presense of other operating transmitters [29]. In this environment, a variety of output powers, frequencies, and polarizations are present, and interference between a number of antennas in each other's near fields changes their radiation properties, accounting for more *wasted* power. The results of this paper show that this power can be absorbed (received), rectified and stored for future use.

Figure 3.1 shows the more typical levels of ambient power densities in the microwave frequency range, with power levels that are too low for most continuous electronic functions. However, if this energy is stored over time efficiently, realistic functions can be performed in discrete time intervals. The ambient rf power levels vary by several orders of magnitude, implying a varying DC load as reflected in the IV characteristics of a single rectenna element, shown in Figure 3.17. For maximum DC power generation, it is necessary to either match the output characteristics of the source with the load, or to insert an intermediate dc-dc converter with peak power tracking. Many techniques for low-power dc-dc conversion are described in [33], with an emphasis on pulse-width modulated (PWM) converters. Traditional PWM

converters are likely to consume far too much power in the control and gate drive circuitry and/or require large off-chip inductor(s) for low-frequency operation. As an alternative, switched-capacitor (SC) converters can provide high efficiency conversion at low power levels over a discrete range of conversion ratios determined by the circuit size and complexity [34]. Although parasitics in silicon processing have limited efficiency of SC converters, recent advances in technologies such as fully-depleted silicon-on-insulator (FD-SOI) have enabled fully integrated efficiencies of greater than 90% [35].
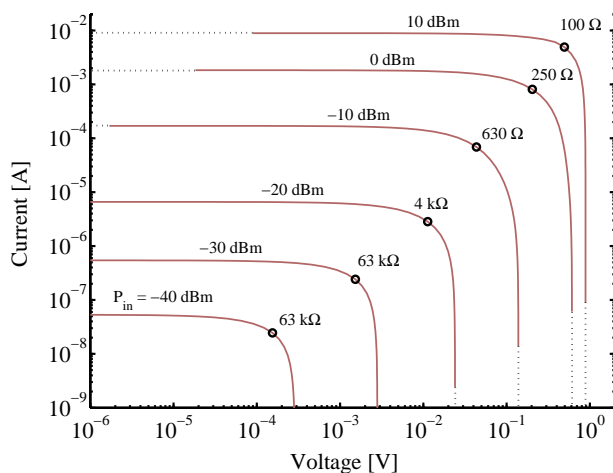
Figure 3.17: Simulated *IV*-curves as a function of load resistance and input RF power to the diode. The peaks in rectified power are indicated by circles with the corresponding optimal load resistance.

Referring to the block diagram in Figure 3.2, two options for energy storage include capacitors and micro-batteries [36]. Capacitive energy storage is appropriate for applications where repeated functions of storing and utilizing

small energy packets is performed, using on-chip (up to 10's of pJ of off-chip, up to 10's of μJ) capacitors. For prolonged operation or larger energy packets, up to four orders of magnitude higher energy densities can be achieved using microbatteries [37].

To illustrate the application of the rectenna energy source, we consider the ability to generate $10\,\mu$J energy packets, which is sufficient for a $1\,$mW, $10\,\mu$s load operation. The energy packet size was selected arbitrarily, but could be used for example for RF transmission of up to $10\,$kbit data packets, or simple sensory and signal processing functions. Over the range of incident power densities under consideration Figure 3.1, and assuming

$$A = A_{eff} = 25\,\text{cm}^2 \tag{3.7}$$

array, we estimate incident power levels of

$$P_{RFmin} = 250\,\text{nW}, \text{P}_{\text{RFmax}} = 2.5\,\text{mW}. \tag{3.8}$$

Assuming a DC-DC conversion efficiency of 90% and rectification efficiencies of

$$\eta(P_{RFmin}) = 1\%, \eta(P_{RFmax}) = 20\%. \tag{3.9}$$

an average DC power output is obtained as

$$P_{DCmin} = 2\text{nW}, \text{P}_{\text{DCmax}} = 450\mu\text{W}. \tag{3.10}$$

The above estimated power levels can be recycled using this kind of a device. In another important application, batteryless sensors, this power is

used to transmit power from this sensor. There are two possible scenarios: (1) vary integration time to achieve fixed energy level, or (2) fix integration time and vary energy packet level. Following approach (1), the system would be capable of a fixed $10\,\mu$J operation at discrete intervals varying from 1.4 hours in the worst case to $20\,$ms in the best case. Thus if a simple sensor required one energy packet to perform the sensory function, and one packet to transmit data, it would be able to transmit new data around 20 times per second in the best case.

An example of this application is a manufacturing environment, where a large number of sensors occasionally transmit data such as stress, temperature, pressure, etc. A large number of such sensors with no batteries that need replacing (or recycling) can be charged with a low-power transmitter overnight. In such an indoor multipath propagation environment, the spatial distribution of polarization and power varies statistically [38]. The results of this paper show that it is possible to efficiently collect such energy by receiving and rectifying two orthogonal polarizations independently and adding the power upon rectification.

Chapter 4

DC–RF Conversion:

Microwave Oscillators

A design methodology for a high-efficiency, switched mode oscillators is presented in the context of present high frequency oscillators and switched mode amplifiers. This chapter seeks to provide the framework for a class-E *X*-band oscillator with maximized DC–RF efficiency without regard to circuit size, complexity, or phase-noise performance. Instead this chapter focuses on a measurement-based nonlinear design methodology for acheiving class-E performance. An external feedback topology is used in order to be able to compare the oscillator performance to well documented class-E amplifier performance. The goal is that future class-E oscillators using different devices or topologies can be designed and evaluated based on the methods and results of this work.

4.1 Microwave Oscillators

Present day power oscillators are used mostly for communication and radar systems [1]. These are typically made with Si BJTs, MESFETs, IMPATT diodes, or GUNN diodes depending on the frequency of operation, noise requirements, or desired output power. Microwave signals generated for frequency and phase purity are typically multiplied up from a MHz range crystal oscillator. Some oscillator needs require octave, or better, tuning in the microwave range. In each of these cases, power, signal purity, and tunability are one or more of the primary concerns and each comes at the expense of the DC–RF efficiency.

Transistor power oscillators have been implemented in planar circuits with some form of feedback mechanism. Feedback is necessary to make the transistor unstable, unlike two-terminal devices. Series feedback has been implemented with open lengths of transmission lines, utilizing the internal feed-back of the transistor; Parallel feedback can be used to directly connect two of the terminals RF-wise; Resistive feedback using lumped components is also commonly used as with the Colpitts and Clapp-Gouriet models [39, 1]. These types of oscillators are usually run in large signal mode and operate with compressed gain of the device. This helps achieve the maximum amount of output power from the device as well as lower amplitude noise. Improved phase noise in power oscillators is usually accomplished by increasing the Q of the circuit, typically by using a dielectric resonator, or phase locking to

a cleaner signal. The selection of the nonlinear device particularly affects the low-frequency phase noise characteristics. For instance, silicon devices have significantly lower flicker noise than GaAs devices and therefore exhibit superior phase noise performance [40].

In energy conversion applications, the DC–RF conversion efficiency becomes more important to the designer, but not at the expense output power which should remain high. DC–DC conversion typically uses a switched or pulse modulated oscillator to regulate a DC power source. In most cases the oscillator or pulse generator is desired to be a near lossless circuit element so that the DC-DC conversion is as efficient as possible. DC-DC conversion at microwave switching speeds is now receiving attention in applications ranging from low-transient voltage regulation [7] to satellite-to-earth power beaming [8]. In these cases phase noise and tunability are not important because usually only one frequency is of interest and it is not used as a signal carrier.

In another example, wireless devices can benefit from improved DC–RF conversion efficiency. In general, a higher oscillation efficiency leads to a longer battery lifetime. Furthermore, some applications may impose strict requirements on power consumption of the signal generator. Again, however, such requirements on the efficiency will put a strain on the achievable phase noise, tunability, and size, and therefore this trade-off must always be considered.

It is with this high-efficiency angle in mind that a class-E oscillator is

Table 4.1: Solid-state device selection based on output power and microwave frequency [1].

Device	Frequency Range:	Corresponding Max P_{out}:	Corresponding Max PAE:
Si BJT	1–5 GHz	500–20 W	$> 60\%$
GaAs MESFET	5–25 GHz	30–5 W	60–40%
IMPATT	25–200 GHz	5 W–30 mW	$<\sim 15\%$
(GUNN)	25–150 GHz	1 W–1 mW	

considered in this chapter. This focus limits the types of circuits to be considered. For instance the Colpitts and Clapp-Gouriet models suffer from too much loss in resistive elements to be be used in a high-efficiency design. A series feedback design is desirable for its simplicity, but provides less control over feedback level and class-E performance. The parallel feedback topology allows direct implementation of existing class-E amplifier topologies into the oscillator. Therefore, this circuit method is the main focus of this chapter. The following sections will discuss high efficiency class-E operation, methods for designing with this highly nonlinear mode, and a characterization of what to expect from a class-E oscillator in terms of output power and efficiency. Experimental results are given for a low-Q design and extensive considerations and design guidelines are posited for a higher-Q design.

4.2 Class-E Operation

The advantage of operating the active device in an oscillator in class-E mode lies in improved DC–RF efficiency and consequent increased battery lifetime. Using a switched mode of operation can have several drawbacks including increased phase noise, AM–PM conversion, and reduced tunability. In general, the output power is not compromised by using class-E. But for a class-E oscillator operating at 50% efficiency, the battery lifetime is twice that of a typical standard oscillator operating at 25% efficiency. Furthermore, half as much energy is lost and one third less is converted to heat.

4.2.1 Class-E Theory

This section discusses basic class-E theory as has been developed by Sokal and Sokal [12], Raab [41], Mader [16], and Pajić [42] for frequencies ranging from 3.9 MHz to 10 GHz. First introduced by the Sokals in 1975, Class-E uses a transistor in common base/source configuration with an AC input drive at the gate/emitter used to switch the drain-to-source impedance from a low to high resistance. The gate and drain bias and input tuning are set so that there is minimal transition time on the switch. The output tuning circuit is designed so that the stored energy in the circuit is not dissipated in the switch itself, but rather released to the load. Furthermore, the output tuning must also filter the harmonic content of the switch waveform so that the output is sinusoidal (and at the frequency of the drive). As outlined in

[16], the solution to the circuit problem of smooth switch-voltage turn off with no switch-current overlap is to present the impedance

$$Z_{net} = \frac{0.28}{\omega_s C_s} e^{j49°} \qquad (4.1)$$

to the output of the device at the fundamental. Here, C_s is the switch capacitance of the transistor which can be de-embedded from measured S-parameters. At 10 GHz, the second harmonic is presented with a transmission line open circuit, and the third harmonic is left unattended. The effects of using finite harmonic filtering is addressed in [17] where results suggested a lower achievable efficiency for a lower number of harmonics used.

Time domain waveforms on the theoretical switch are usually shown to demonstrate how the energy stored in the internal capacitance (mainly C_{gs}) is released before the switch closes [41]. Additionally, it useful to keep in mind the quasi-static IV characteristics of the device. Class-E requires a drive voltage large enough to force the transistor into pinch-off (no conduction) during a fraction of the period, while opening the gate for the remainder of the drive cycle. Ideally, the load line of a class-E operating circuit will move along the I_{ds} and V_{ds} axes so that the two are never simultaneously non-zero. This is equivalent to having no current and voltage overlap in the time-domain waveforms.

4.2.2 Figures of Merit

Amplifier efficiency is defined in terms of the input and output RF power, $P_{rf(in)}$ and $P_{rf(out)}$, and the DC power consumed, P_{dc}. The conversion of DC power to RF power, neglecting the amount of input RF used to drive the amplifier, is given by the drain efficiency, η_D:

$$\eta_D = \frac{P_{rf(out)}}{P_{dc}} = \frac{P_{rf(out)}}{V_{ds}I_{ds}}. \tag{4.2}$$

The overall efficiency η takes into account the RF input power and DC power to compute the ratio of available power to total input power:

$$\eta = \frac{P_{rf(out)}}{P_{rf(in)} + P_{dc}} = \frac{P_{rf(out)}}{P_{rf(in)} + V_{ds}I_{ds}}. \tag{4.3}$$

The power added efficiency, or PAE, indicates the ratio of RF power gained from DC to DC power consumed:

$$\eta = \frac{P_{rf(out)} - P_{rf(in)}}{P_{dc}} = \frac{P_{rf(out)} - P_{rf(in)}}{V_{ds}I_{ds}}. \tag{4.4}$$

For an amplifier modified with feedback to create an oscillator, the DC–RF efficiency is given by

$$\eta_{osc} = \frac{P_{rf(out)}}{P_{dc}} = \frac{P_{rf(out)}}{V_{ds}I_{ds}}. \tag{4.5}$$

Though equations are identical in form, η_{osc} is not analogous to the drain efficiency. From these descriptions the important result becomes evident that the oscillator DC–RF efficiency is tantamount to the amplifier PAE. In other

words, the amount of RF energy used to drive the oscillator, $P_{rf(in)}$ must be subtracted from the transistor output as feedback. Then the remaining RF, $P_{rf(out)} - P_{rf(in)}$ is the available power from the oscillator and the DC power is the only input power. Therefore, the maximum achievable PAE of an amplifier determines the maximum DC–RF conversion of an oscillator based on that amplifier.

4.2.3 Class-E Performance

Switched-mode operation has only been applied to transmission line microwave amplifiers and oscillators above 1 GHz since the 1990's. Table 4.2 summarizes the performance that has been achieved for various classes at various frequencies for both switched mode amplifiers and oscillators:

Table 4.2: Comparison of previous work in the field for high-efficiency amplifiers and oscillators. PSD refers to the power spectral denisty at a given offset from the carrier.

	circuit	class	f [GHz]	P_{out} [dBm]	η_{osc} [%]	PSD
Sokal [12]	amp	E	0.004	44	96	NA
Mader [16]	amp	E	1.0	30	73	NA
Pajić [42]	amp	E	10.0	20	57	NA
Bryerton [43]	osc	E	5.0	25	59	-70$\frac{\text{dBc}}{\text{Hz}}$ at 100 kHz
Prigent [44]	osc	F	1.6	24	67	NA
McSpadden [45]	osc	AB	14.5	12	60	NA

4.2.4 Diagnostic Tools for Class-E Behavior and Performance

Class-E theory has been somewhat experimentally verified using time domain photo-conductive sampling of X-band amplifiers [46]. In the case of the class-E oscillator, evidence of class-E performance is further blurred due to the increased number of unknowns over the amplifier. Therefore the oscillator cannot be analyzed solely in terms of a specific bias point, input power, and output matching: instead, these must be allowed to vary in the analysis. Nonlinear Harmonic Balance (HB) simulations have provided much insight on the behavior of this class-E amplifier and have produced good agreement with measurements. Its accuracy cannot compare with a measurement based analysis, however. A three-dimensional bias sweep of the gate and drain bias and input power can provide a significant amount of design information, as will be discussed in the next section. The class-E impedance as derived from Equation 4.1 is also an approximation which may not yield optimal results. A load-pull analysis can provide insight into how parameters such as efficiency and output power vary with load impedance. In this way a range of load (and source) impedances can be determined rather than a single point. In lieu of a load-pull measurement system at 10 GHz, the HB simulation can be used as convenient analysis tool [47, 18].

Simulated source and load-pull plots (Figure 4.1) show the sensitivity of the efficiency and output power to the impedances presented to the input
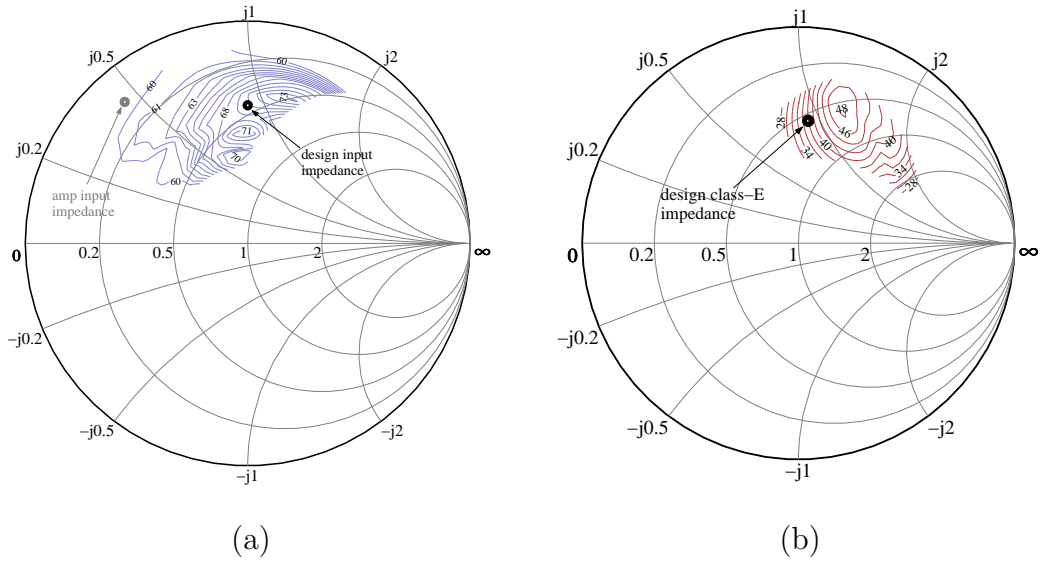
Figure 4.1: Simulated source-pull (a) and load-pull (b) performed on the TOM model of the Alpha AFM04P2 MESFET in *ADS* HB.

(source) and output (load) of the device. Additional load-pull diagrams for various input powers provided the insight that the optimal load reactance increases with input power, while the load resistance stays roughly constant. Such information was then used in the design to adjust the analytically derived class-E impedance. Furthermore, post production tuning of the input and output stubs is driven by the trends suggested by Figure 4.1.

4.3 Class-E Oscillator Design Based on Class-E Amplifier Measurements

The following study shows how a parametric analysis based on measurements can be used to help design the oscillator instead of relying on typical quasi-linear methods. The optimal bias point, feedback level, and output power are determined for highest DC–RF efficiency based on amplifier measurements. Each of these operating conditions depend on highly nonlinear phenomena stemming from driving the transistor in a switched-mode class and driving it into compression as well.

4.3.1 Amplifier Measurements for Oscillator Design

Transistors operated in Class-E mode have S-parameters which can be significantly different from small-signal values specified by the manufacturer. For instance, the S_{21} amplitude (amplifier gain) is typically much smaller in class-E compared to the small-signal class-A case. Furthermore, the impedance looking into a switch is much more difficult to characterize. For these reasons, the circular function

$$C = \frac{S_{11}S'_{11} + S_{21}S'_{12} - (S_{11}S_{22} - S_{12}S_{21})(S'_{11}S'_{22} - S'_{12}S'_{21})}{1 - S_{22}S'_{22} - S_{12}S'_{21}} \qquad (4.6)$$

(where S_{ij} refer to transistor S-parameters and S'_{ij} refer to loop-network S-parameters) is a poor approximation if small-signal transistor S-parameters are used. If large signal S-parameters are not available as a function of bias

and input power (as is the case here) then the following characterization becomes necessary to be able to select the optimal operating point, and to design the loop-network.

A 10-GHz class-E amplifier using the AFM04P2 MESFET transistor produced by Alpha Industries Inc. has been designed and optimized by Srdjan Pajić in [42]. One of the Pajić amplifiers was then characterized in light of this work by performing a three-dimensional sweep over gate bias, drain bias, and input power. The ranges used were -1 to -2 V for the gate voltage, 2 to 5 V for the drain, and -8 to 15 dBm for the input power. At each sweep level, the PAE, P_{out}, G, and P_{refl} were measured.

The results are summarized in two ways: The contour plot of Figure 4.2 (a) shows how the PAE and P_{out} vary with bias point for one particular input power level. The accompanying plot of Figure 4.2 (b) demonstrates how that power level was chosen, i.e. it was chosen where the PAE is maximum. Figure 4.2 (b) also demonstrates the important result that the PAE reaches a maximum at a point where P_{out} is still expanding. Furthermore, the optimal PAE occurs at a different bias point than the optimal output power. Therefore, if output power is a concern, a compromise can be made by allowing more gain and using a bias point between the two optimal points.

The oscillator design then begins with the following specifications based on Figure 4.2 (a) and (b): The optimal bias is expected to occur at $V_{gs} = 1.4$ V and $V_{ds} = 3.8$ V (note that this can be a different bias point than would be considered optimal for the amplifier). At the same time, it is desired

79
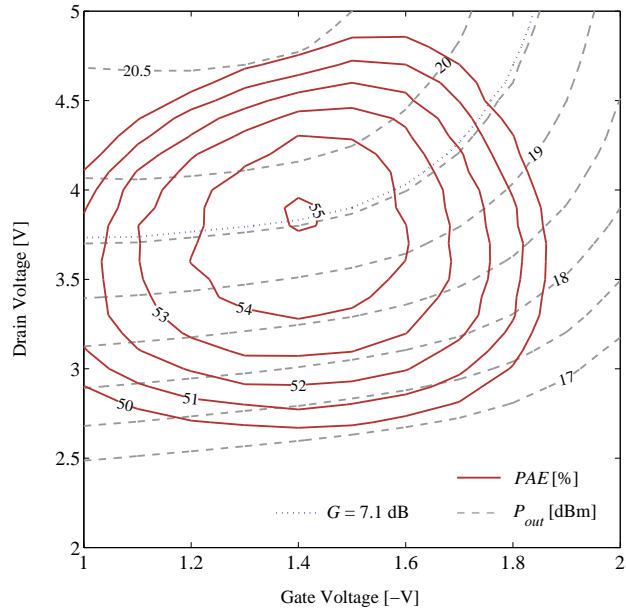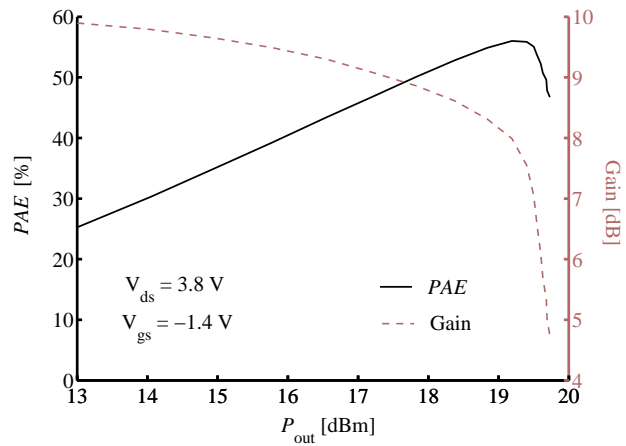
Figure 4.2: Measured 10-GHz class-E amplifier contours for PAE and P_{out} over bias voltage (a) and PAE along with G versus output power (b).

that the amplifier gain be near 7 dB. Therefore, the feedback network should be designed to couple near 7 dB back to the input of the amplifier, while P_{out}=-0.97 dB is delivered to the output load. The feedback coupler should maintain the power level associated with the maximum PAE by maintaining the correct amount of amplifier gain, given that the loop phase is also correct.

It must be stressed that the class-E oscillator cannot be operated with sets of parameters different from those measured in the class-E amplifier. For instance, a gain of 10 and 50% PAE will not be possible simultaneously with 18 dBm input power at the optimal bias point for PAE. Each parameter (bias, feedback, anticipated frequency, output power and efficiency) must be chosen together based on what the amplifier measurements predict is possible. To summarize, the predicted best case oscillator performance based on amplifier measurements is η_{osc} =56% with P_{out} =18.5 dB and $G = 7.1$ dB.

4.4   A low-Q X-Band Class-E Oscillator

A preliminary design for a 10-GHz oscillator was designed and tested using a simplified low-Q feedback circuit. In this approach, a tee-junction is used to split the feedback and output paths from the amplifier circuit. Since this three-port junction cannot be matched, lossless, and reciprocal, the mismatch is incorporated into the class-E load. Furthermore, the line length of the feedback loop and input matching are adjusted for the $2\pi n$ loop electrical path-length and for approximately 7 dB coupling. Designing the oscillator

in this manner avoids the use of a 4-port coupler and allows for a relatively short feedback loop. However, the Q of the feedback loop is determined only by the input and output matching stubs and the path length. Furthermore, the amount of feedback is sensitive to the loading of the tee-junction. This means that variations in input and output impedance of the device, which depend on bias and RF power levels, create varying feedback levels. For these reasons the phase and amplitude noise of this oscillator are expected to be poor. In addition, it is expected that the class-E impedance will be hard to obtain simultaneous with proper biasing and input power.
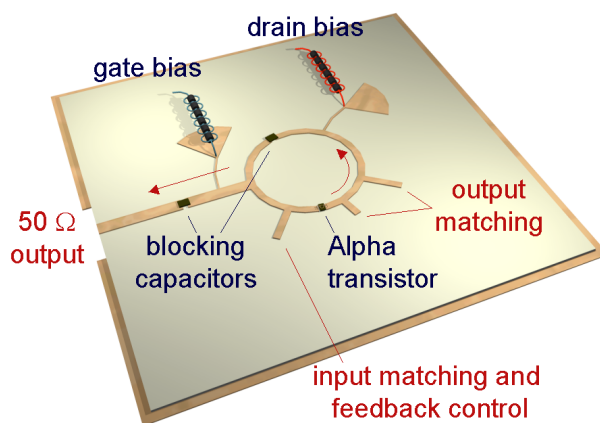
Figure 4.3: Drawing of the low-Q 10-GHz oscillator prototype. This feedback oscillator is more compact than the subsequent design but suffers from poor phase and amplitude noise.

This oscillator achievs 17.6 dBm output power at 10.35 GHz and 29% DC–RF efficiency at its high-power bias point, $V_{ds} = 5$ V and $V_{gs} = -1.2$ V. At the anticipated optimal bias point, $V_{ds} = 3.8$ V and $V_{gs} = -1.4$ V, 15.9 dBm

82

output power is available at 30% efficiency. Figure 4.4 demonstrates the power and efficiency performance for other bias levels and Figure 4.5 shows additional characterizations in terms of current draw and efficiency relavent to assessing class-E behavior. Since the efficiency levels are below what is anticipated for class-E behavior, it is concluded that the class-E impedance is not reached in this circuit. More likely the oscillator was operating in a class similar to class-AB.
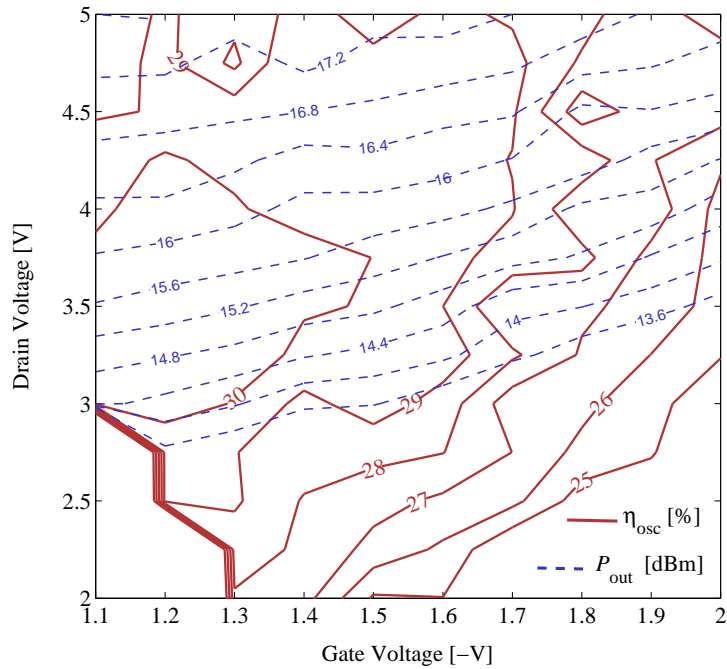
Figure 4.4: Contours for output power (a) and efficiency (b) versus gate and drain bias levels for the low-Q feedback oscillator prototype.

Based in simulation, the Q of the circuit is thought to be on the order of 20. The use of radial stubs helped to ground low frequency modes of oscil-
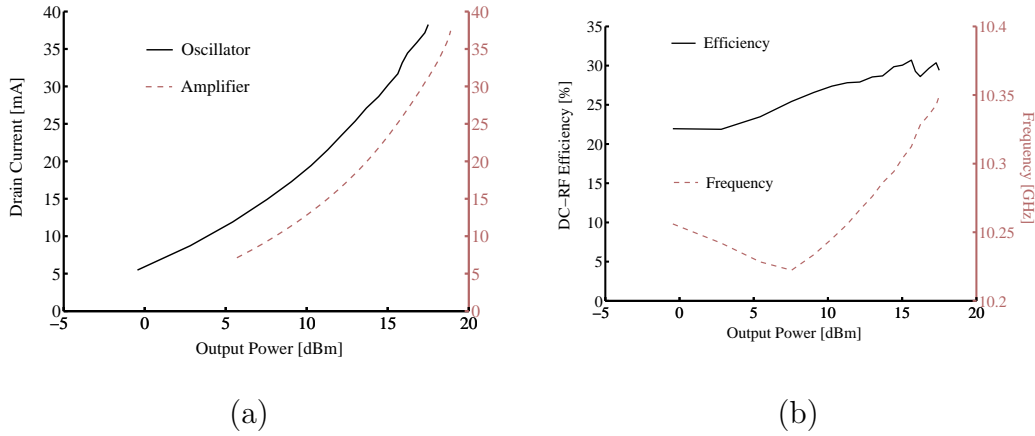
Figure 4.5: Comparison of measured oscillator drain current vs. output power with comparable class-E amplifier current draw (a). In (b) the frequency of oscillation and efficiency are plotted versus output power.

lation, allowing for a fairly stable 10-GHz signal in free-run mode. However the amplitude noise is so poor for this low-Q oscillator that phase noise is impossible to extract. The reason for the poor noise performance is that low-frequency phase variations, with causes ranging from flicker frequency noise to slowly varying bias drift, are not stabilized in the low-Q circuit so that frequency fluctuations translate into matching and feedback coupling fluctuations which cause amplitude variation. To address these problems, a more reliable coupling mechanism and higher-Q filtering are added to the design, as discussed in the following section.

4.5 Improved class-E Oscillator Design

To gain more control on parameters such as feedback coupling ratio and oscillation frequency, the previous low-Q design is modified in five important ways: 1) A well characterized 4-port coupler is used for the feedback; 2) A resonator with Q on the order of 150 is added to the circuit; 3) The oscillator is designed around an independent amplifier design; 4) The oscillator is modeled as two back-to-back amplifiers; 5) Measurements of the nonlinear phase through the transistor are used to design the closed-loop path length.

4.5.1 Asymmetric Branch-line Coupler

A coupler is desired which can provide low return loss and specific coupling over the bandwidth of potential oscillating frequencies. The tee-junction used in the previous section was seen to contribute to amplitude noise due to its frequency sensitive coupling characteristics. In this section a branch-line coupler is investigated as an alternative which requires an isolated port but also provides a good handle on the feedback mechanism in the oscillator.

Since a specified amount of coupling is desired, a convenient design for an asymmetric 4-port branch-line coupler is used. The coupler is designed according to guidelines given in [48] by using the following equations:

$$Z_a = 50\frac{|S_{21}|}{|S_{31}|} \quad \text{and} \quad Z_b = 50\sqrt{\frac{|S_{21}|^2}{|S_{21}|^2 + |S_{31}|^2}} \tag{4.7}$$

where Z_a is the characteristic impedance of the series sections of the
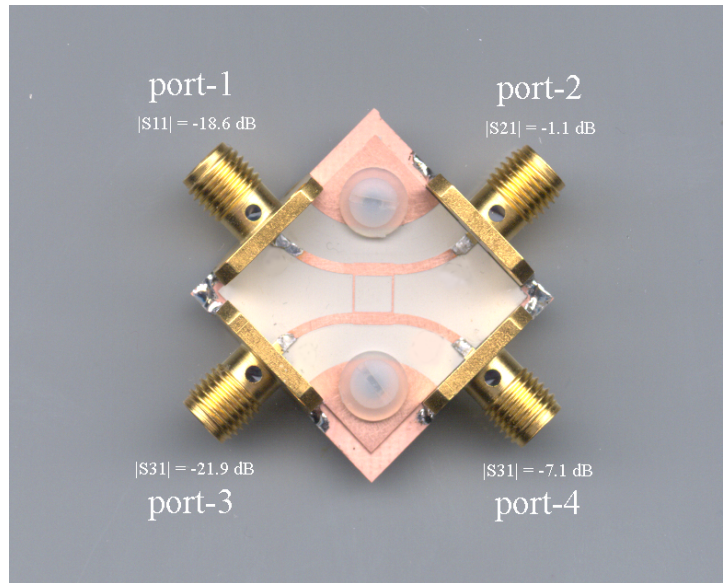
Figure 4.6: Photograph of the asymmetric branch-line coupler designed for -7.4 dB coupling (S_{31}).

branchline coupler and Z_b that of the shunt sections: S_{21} refers to scattering to the through port and S_{31} to the coupled port referenced to the input port.

Based on the analysis of optimal feedback level performed earlier, a coupling ratio of -7.1 dB was designed for. A photograph of the resulting coupler is shown in Figure 4.6. For -7.1 dB coupling from port-1 to port-3 in Figure 4.6, 106 Ω and 45.2 Ω lines were required. Measurements on the coupler

yielded the following results for $20 \log_{10}|S_{ij}|$:

$$
S_{ij}(meas) = \begin{bmatrix}
-\mathbf{18.6} & -1.07 & -21.8 & -7.06 \\
-\mathbf{1.12} & -19.0 & -7.12 & -22.3 \\
-\mathbf{21.9} & -7.03 & -15.4 & -1.23 \\
-\mathbf{7.10} & -22.1 & -1.15 & -15.1
\end{bmatrix}
$$

The numbers in bold in the first column are chosen to summarize the important results as they pertain to the oscillator: -18.6 dB input matching to the coupler (representing the load to the amplifier stage), -1.12 dB coupled to the output (output of the oscillator), -21.9 dB showing up at the isolated port, and -7.10 dB coupled to port-3 (as feedback to the amplifier stage). With these numbers (which do not include connector loss) over 98% of the power is accounted for. MoM simulations performed in Agilent ADS predict -7.7 dB coupling, a disagreement which was to be expected due to the inaccuracy in milling the 0.16 mm 106 Ω lines.

4.5.2 Resonator Design

Increasing the Q of the closed-loop path not only improves the phase noise of the oscillator but also helps suppress spurious modes of oscillation. While dielectric resonators have been used with Q-factors in the hundreds to thou-

sands, a more convenient microstrip ring coupler is used here as implemented by [49, 50, 51]. What is more, the coupling arms to the ring can be adjusted (using an *x-acto* knife) to tune the resonance frequency and, in turn, the closed-loop phase. Therefore the ring coupler is used as the primary post-production tuning mechanism. The layout of the ring coupler is shown as it was used in the oscillator in Figure 4.7.
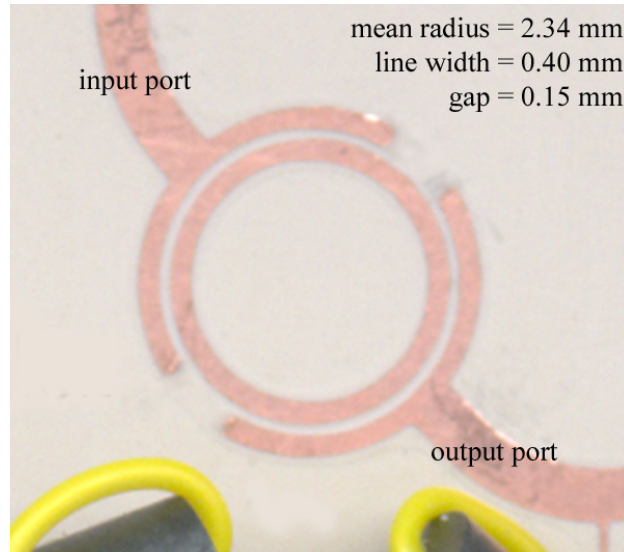
Figure 4.7: Photograph of the two-port microstrip ring resonator with coupling arms.

Based on measured results, the loaded Q of the ring coupler was approximately 100. It was also found that frequency and phase can be tuned from 10.1 GHz down to 9.97 GHz ($\Delta f = -40\,\text{MHz}$) with a *thru*-phase change of $\Delta \phi = -38°$ by shortening the coupling arms 16° (from the center of the ring). By comparison, a 50 Ω line on this substrate changes by $\Delta \phi = -10.4°$

over the same frequency span. The *thru* loss, or S_{21}, of the coupler was measured to be -0.5 dB before tuning. The loss increases as much as 1.2 dB as the arms are shortened by 70°. Not unimportantly, the coupled lines to the ring also provides isolation from DC to 10 GHz between its input and output ports, both helping to block low frequency oscillations and serving to replace a dc-blocking capacitor.

4.5.3 Two-stage Amplifier Analysis

The class-E amplifier is placed in the environment of an oscillator by presenting its output with the coupled input of an identical amplifier operating under the same conditions. By doing this, it is possible to draw several conclusions about theoretical oscillator performance before building the oscillator itself. In fact every aspect of the oscillator is determined except for the phase path (length of 50 Ω required for the oscillation condition) and additional resonator.

The design layout of Figure 4.8 shows the feedback oscillator divided into two parts: the active amplifier stage with matching networks and the passive 4-port coupler consisting of input (1), output (2), isolated (3), and coupled(4) ports. The design procedure addresses the following questions and unknowns:

1) Can the amplifier, operating in the nonlinear class-E mode, be modeled as a 50 Ω Thévenin source to drive the coupler at $b1$.

2) Is the input impedance of the amplifier sufficiently matched to 50 Ω to

Figure 4.8: Schematic of the class-E oscillator with ports labeled for comparison to the two-stage circuit. Ports a1 and b1 relate to the input and output ports shown in Figure 4.9, while the output refers to P_{sigh}. The unknown will remain the phase lengths l.

properly load the coupler at $a1$.

3) If not well matched, how much power is then lost in the isolated port.

4) How much output power and what DC–RF efficiency can we expect from the oscillator.

5) Are there any spurious oscillations due to amplifier S_{12} or other reasons.

The phase through the amplifier and through the coupler will be measured separately using a Network Analyzer. The remaining path length needed for $2\pi n$ total phase will be estimated using MoM simulations together with additional Network Analyzer measurements.

Figure 4.9: Photograph of the two-stage amplifier with identical class-E amplifiers and asymmetric branch-line coupler.

The two stages behave differently when the gain of the first stage deviates from 7.1 dB, i.e. the input power to the second stage is different from the input power to the first stage. Therefore we are interested in the instances where the gain of both stages are near 7.1 dB for the same bias point on each amplifier. After locating a set of operating points (bias point and input power) where the two gains are equal, the power levels at the various ports must be compared. If they are roughly equal, then we can confirm the assumption that the two-stage amplifier is operating in an equivalent environment to an oscillator. Table 4.3 shows five cases where the gains of each stage are equal.

To extend these results to a hypothetical oscillator, the oscillator output power corresponds to P_{sig} and the DC–RF efficiency corresponds to (either)

Table 4.3: Summary of the two-stage test (refer to Figure 4.9)

bias	G_1 dB	G_2 dB	P_{out1} dBm	P_{out2} dBm	P_{in1} dBm	P_{in2} dBm
$V_{ds} = 3.8\,\text{V}$ $V_{gs} = -1.2\,\text{V}$	7.06	7.01	18.4	18.3	11.3	11.3
$V_{ds} = 3.9\,\text{V}$ $V_{gs} = -1.3\,\text{V}$	7.08	7.04	18.4	18.3	11.3	11.3
$V_{ds} = 4.3\,\text{V}$ $V_{gs} = -1.4\,\text{V}$	7.11	7.14	18.9	18.9	11.8	11.8
$V_{ds} = 4.1\,\text{V}$ $V_{gs} = -1.5\,\text{V}$	7.02	7.12	18.3	18.3	11.2	11.3
$V_{ds} = 3.9\,\text{V}$ $V_{gs} = -1.6\,\text{V}$	7.07	7.25	17.4	17.6	10.3	10.3

bias	PAE_1 %	PAE_2 %	P_{sig} dBm	P_{iso} $\text{dB}_{P_{out1}}$	P_{refl} $\text{dB}_{P_{in1}}$
$V_{ds} = 3.8\,\text{V}$ $V_{gs} = -1.2\,\text{V}$	43.8	44.9	17.2	-13.1	-13.4
$V_{ds} = 3.9\,\text{V}$ $V_{gs} = -1.3\,\text{V}$	44.4	46.1	17.3	-13.7	-14.8
$V_{ds} = 4.3\,\text{V}$ $V_{gs} = -1.4\,\text{V}$	43.7	46.7	17.8	-14.2	-15.5
$V_{ds} = 4.1\,\text{V}$ $V_{gs} = -1.5\,\text{V}$	44.2	47.8	17.2	-14.8	-16.6
$V_{ds} = 3.9\,\text{V}$ $V_{gs} = -1.6\,\text{V}$	43.8	48.8	16.3	-15.7	-15.9

PAE. The best case scenario found in these measurements is a $P_{sig} = 17.8 \, \text{dBm}$ at roughly 45% efficiency. As mentioned before, higher PAE can result by allowing higher gain. This is done by altering the coupler for less coupling ($S_{31} < -7.1 \, \text{dB}$) which will also allow more output power P_{sig}.

The result that more gain is needed is part of what this design test was meant to reveal. It has also been shown that we can observe class-E behavior in an oscillator environment. These results can then be used together with a phase path study to finish the oscillator design.

4.5.4 Phase Measurements

The closed loop phase of the oscillator must be $2\pi n$ to optimize the oscillation condition. This is equivalent to setting the reactance of the output of the transistor to the negative of the transistor reactance. The phase (reactance) of the transistor, however, is a function of input power to the device and bias level. Therefore a characterization of the *thru* phase is in order. The phase through the same class-E test amplifier is measured as a function of gate bias, drain bias and input power (Figure 4.10). The result is used for design of the excess transmission line path length and for post fabrication fine tuning.
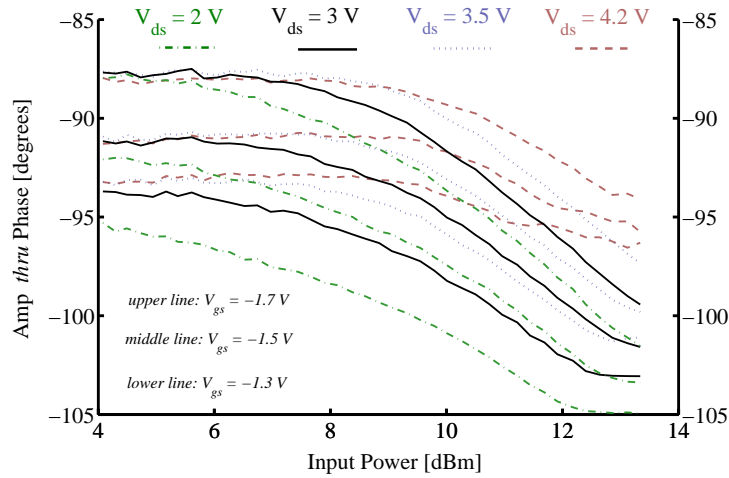
Figure 4.10: Measurements of nonlinear amplifier phase response.

4.5.5 Mid-Q Oscillator

The stand alone class-E oscillator, asymmetric branch-line coupler and microstrip ring resonator are incorporated into a class-E oscillator design (Figure 4.11. To date, two iterations of the oscillator have not produced 10-GHz oscillations. The immediate culprit is the path length of the feedback loop. Since 90° at 10 GHz in this substrate is x mm, and the overall path length is y mm, the room for fabrication error turns out to be substantial. The best solution appears to be to build several oscillators each with graded path lengths (rather than adding a lossy tuning mechanism). As mentioned before, tuning the ring couplers coupling arms provides 20° or more of tuning, therefore a limited number of iterations should find the proper phase.

While 10-GHz oscillations proved elusive after two iterations, the fact

94
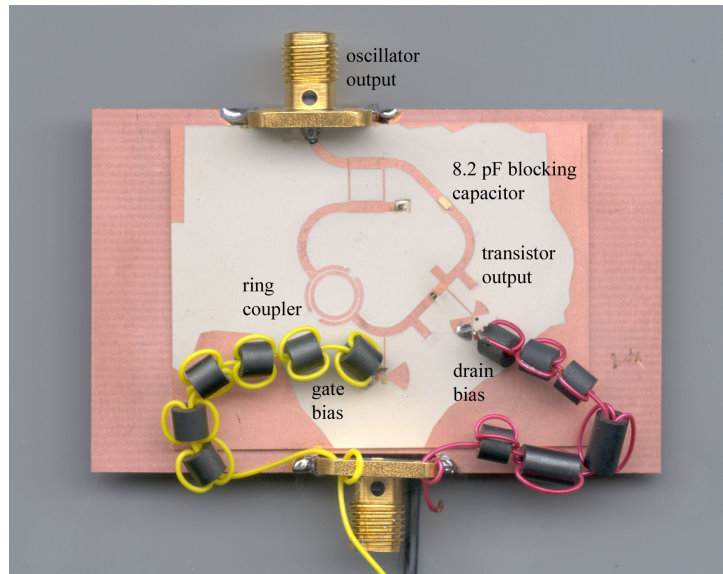
Figure 4.11: Photograph of the oscillator design with implementation of the stand alone class-E amplifier, asymmetric branch line coupler, and ring resonator.

that the circuit did not oscillate *anywhere* is a promising result. This proves that the Q of the circuit is high enough to block oscillations at all frequencies except at its resonance frequency, and possibly harmonics of that frequency. However since an open circuit at $20\,\mathrm{GHz}$ is presented at the output of the device, and since the device can support little gain at $30\,\mathrm{GHz}$, oscillations at these frequencies are not anticipated.

As a sanity check, a coaxial probe was used to inject the circuit with power near $10\,\mathrm{GHz}$. It was concluded that the biased device successfully amplified this injected power. However, since no oscillations could be coaxed, the conclusion was further substantiated that the feedback was destructive.

Chapter 5

DC–Radiated RF Waves:

A Self-Oscillating Annular Ring

5.1   Motivation

Free-space power combining of distributed oscillating elements presents a
high-efficiency solution to microwave dc-rf conversion. By distributing sources
in an array, transmission lines, combiners, and associated losses can be re-
duced or eliminated. Furthermore, the circuit size of the individual oscillat-
ing elements can be greatly reduced by incorporating the antenna element
directly as a resonator and feedback circuit. Early designs have combined
the radiating element as a load with a stand-alone oscillator and separate
feedback loop. More recent designs have used rectangular patches as a radia-
tor in the feedback path [54, 55, 56]. FETs were also directly integrated into

the radiating element using modified antenna geometries for direct matching [57, 58]. Similarly a 100-MESFET grid oscillator capable of high output power and gain was first reported in [59].
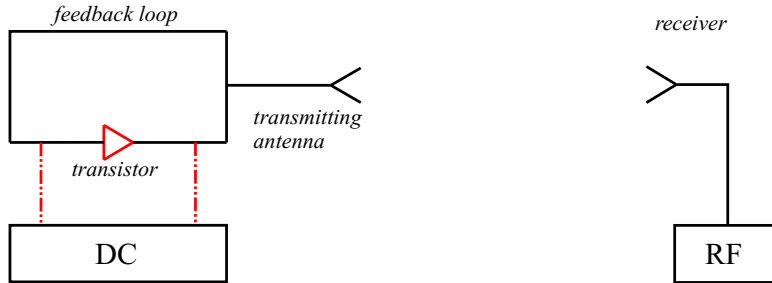
Figure 5.1: Diagram of a self-oscillating antenna with DC supply and radiation mechanism. The amount of RF available to the receiver system is described by the ERP. The efficiency at which the DC is converted to the received RF is described by the isotropic conversion gain, G_{iso}.

In this chapter, the advantages of using a compact single layer, high gain, switched mode integrated oscillating antenna are investigated. The performance of the unit cell is then assessed as an element for a high-efficiency power combining array. A microstrip annular ring has been chosen to improve the radiation characteristics and to reduce microstrip circuitry over conventional designs. The entire circuit is enclosed inside the ring allowing for straight-forward, compact array design. High-efficiency is afforded by switched mode transistor operation, high antenna gain, and potential for high array packing density.

The fundamental role of self-oscillating antennas is to convert as much

available DC energy to RF at a distant receiving aperture. Applications include short range free space power beaming as in [20] and long range systems as in the Space Power System (SPS) [8] where sunlight is converted to DC on a satellite, then converted to RF and beamed to a ground-based collector site. Another application is Doppler sensing as in [60]. As will be shown, the linear frequency tuning of the oscillator allows for local mixing of a reflected signal. Interestingly, neither application requires low phase noise. In fact, a tunable oscillator must have higher phase noise for a greater tuning range. The ring presented here is a low-Q resonator for the oscillator and no attempt is made in this work to improve the phase noise.

5.2   The Active Ring

5.2.1   Analysis Tools

To aid in the design of the active ring antenna, analytical equations and method of moments (MoM) solvers (for antenna design), linear and non-linear circuit solvers (ADS and Momentum), and measurement-based models (from switched-mode amplifiers) were used. A modal analysis of the ring structure was performed by solving the transcendental equation

$$J_n'(kb)Y_n'(ka) - J_n'(ka)Y_n'(kb) = 0 \tag{5.1}$$

where the mth zero of the nth order Bessel function corresponds to the resonant frequency of the TM_{nm} mode and b and a are the outer and inner
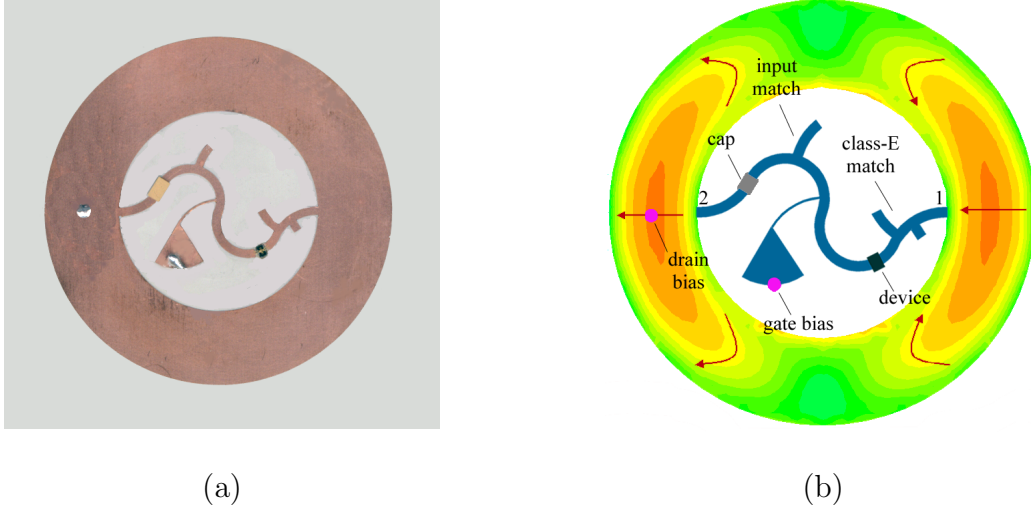
Figure 5.2: Photograph of the 10-GHz active ring (a) and simulated depiction of the total current density distribution for the TM_{12} operating mode (b).

radii of the annulus. Equation 5.1 and the equations for the E and H–plane radiation given by

$$E_\theta = j^n \frac{2E_o}{\pi k_{nm}} \frac{e^{-jk_o r}}{r} k_o h \left[J_n'(k_o a \sin\theta) - \frac{J_n'(k_{nm}a)}{J_n'(k_{nm}b)} J_n'(k_o b \sin\theta) \right] \cos n\phi \quad (5.2)$$

$$E_\phi = -nj^n \frac{2E_o}{\pi k_{nm}} \frac{e^{-jk_o r}}{r} k_o h \left[\frac{J_n(k_o a \sin\theta)}{k_o a \sin\theta} - \frac{J_n'(k_{nm}a)}{J_n'(k_{nm}b)} \frac{J_n(k_o b \sin\theta)}{k_o b \sin\theta} \right] \sin n\phi \cos\theta \tag{5.3}$$

are derived from a cavity model of the annular ring [61]. More accurate solutions for input impedance, radiation patterns, and two-port behavior of the ring were performed using Zeland *IE3D* and Ansoft *Ensemble* MoM solvers. The linear circuit solver and nonlinear harmonic balance solver from Agilent *ADS* were also used to simulate the integrated antenna and transistor. In

99

addition to simulation, the ring design is also heavily based on measurements of passive rings and class-E amplifiers, as done in Chapter 4.

5.2.2 Figures of Merit

Figures of merit for the active ring fall into the following three categories:

- *Oscillator performance:*

P_{out}: the output power in the fundamental frequency leaving the device.

$\eta_{osc} = P_{out}/P_{dc}$: DC–RF efficiency where $P_{dc} = V_{ds}I_{ds}$.

- *Antenna performance:*

P_{lat}: lateral radiatied power in the E–plane normalized to broadside.

G_{ant}: the antenna gain.

- *Integrated performance*

$ERP = \frac{(4\pi R)^2 \cdot P_{rcv}}{\lambda^2 G_{rcv}} = P_{out}G_{ant}$: effective isotropic radiated power.

$G_{iso} = ERP/P_{dc} = G_{ant} \cdot \eta_{osc}$: the isotropic conversion gain.

The effective radiated power and DC power are the directly measurable quantities. Their quotient, G_{iso}, is a measure of how efficiently DC power has been converted into a directed, linearly polarized beam. The isotropic conversion gain is the most important parameter for an active antenna whose goal is efficient power transfer.

5.3   Antenna Design

The microstrip annular ring, operating in the TM_{12} mode is chosen primarily for its convenience as a two port coupling mechanism and the ease with which its radiation pattern can be controlled. Analysis of the antenna as a two-port is addressed in the following section while the design and characterization of a passive one-port annular ring are the topics of this section.

5.3.1   Lateral Radiation

In order to operate in a densely packed array, the single element is designed for minimal lateral radiation. Lateral radiation is defined as the radiated power at the angels $\theta = -90°, +90°$ (also radiation in the azimuth plane). In fact it has been shown that lateral radiation is a greater contributer to mutual coupling between nearest neighbors than surface wave excitation [62]. At the same time, the two are related by the patch geometry and suppression of one leads to suppression of the other. In most patch antennas, lateral radiation and surface wave excitation are not easily suppressed without elaborate designs [63]. However, operating the annular ring in the TM_{12} mode allows for optimization of the b/a ratio (outer/inner ratio) for minimal lateral radiation, P_{lat}. Furthermore, reducing P_{lat} leads to an increase in antenna gain and therefore, improved G_{iso}.

The lateral co-polarized radiation in the H–plane is theoretically null, and is therefore typically very low (30 to 40 dB down from the broadside
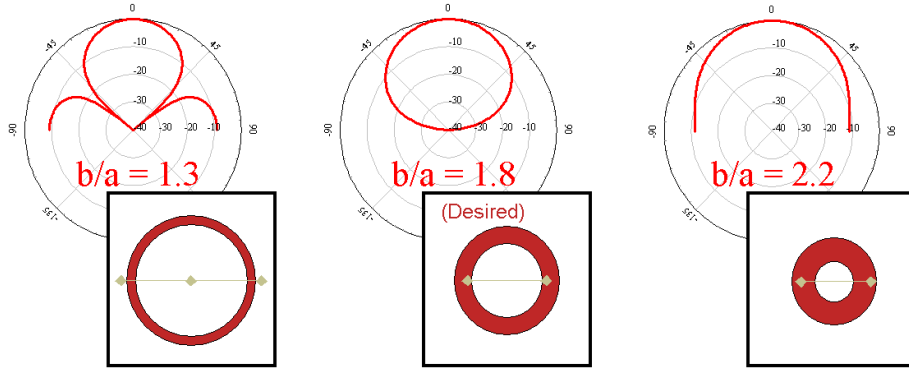
Figure 5.3: Calculated E–plane radiation patterns from Equation 5.2 as a function of b/a ratio.

radiation) in practice. The lateral co-polarized E–plane radiation, however, is directly dependent on the ring geometry, as is evident from Equation 5.2. This can also be understood from Figure 5.2 (b) which shows that the two regions of current maxima form an effective two-element array. If the array is spaced properly, then lateral nulls can be achieved in the E–plane as well with greatly reduced radiation in all other lateral directions including cross-polarized radiation (which is a concern for the TM_{12} mode).

The three cases shown in Figure 5.3 illustrate how the E–plane radiation pattern changes with ring geometry (a change in b/a ratio requires rescaling to maintain resonance at the same frequency). The level of P_{lat} in the E–plane is computed as a function of b/a using Equation 5.2 and the chosen substrate parameters and plotted in Figure 5.4. The curves of Figure 5.4 are specific to the substrate parameters chosen, in this case the Rogers TMM10i
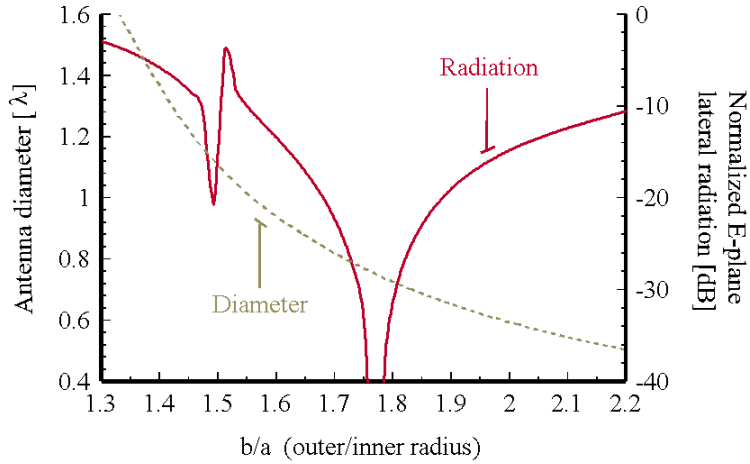
Figure 5.4: Calculated radiated power in the azimuth direction of the E-plane normalized to the broadside radiation.

substrate with $\epsilon_r = 9.8$ and $h = 0.381\,\text{mm}$. This choice of substrate also depends on proper mode separation as discussed in the next section. For the analysis of lateral wave excitation, it is presumed that the geometry with the lowest P_{lat}, $b/a = 1.743$, will be the optimal choice for minimal mutual coupling in a hypothetical array of annular rings.

5.3.2   Modal Analysis

A modal analysis can be performed on the ring as a function of b/a ratio given the substrate parameters. Such an analysis is important because unwanted resonant modes can potentially overlap in frequency with the TM_{12} mode and degrade both the desired active performance and radiation pattern.

The two classes of modes of concern here are the TM_{n1} and TM_{n2} modes.
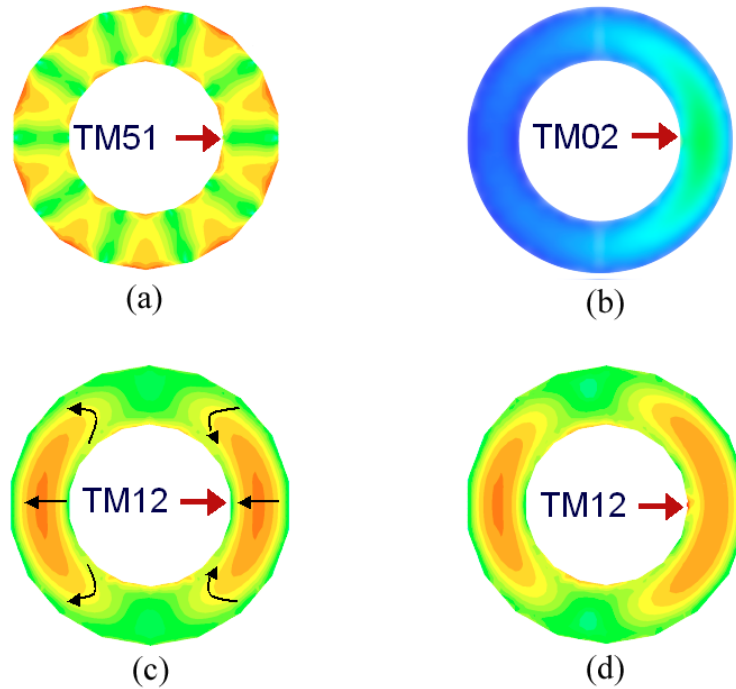
Figure 5.5: Simulated current distributions for various modes of concern in the annular ring. The amplitude of the total surface current density is plotted along with arrows indicating the feed points.

The surface current distributions of the four most important cases are shown in Figure 5.5 with the locations of the inner-radius edge-feeds. The TM_{51} mode is shown as an example of a TM_{n1} that can occur degenerately with the TM_{12} mode. These modes vary more dramatically with the radius of the ring than the TM_{n2} modes, which causes the overlapping. The TM_{02} mode occurs very close to the TM_{12} mode but can easily be avoided in the design of the active circuit. The TM_{12} mode is shown at resonance and slightly off resonance. As will be shown, side-lobes in the measured patterns are a result

of this asymmetry in the current distribution when the oscillation frequency is slightly off the ring's resonant frequency.
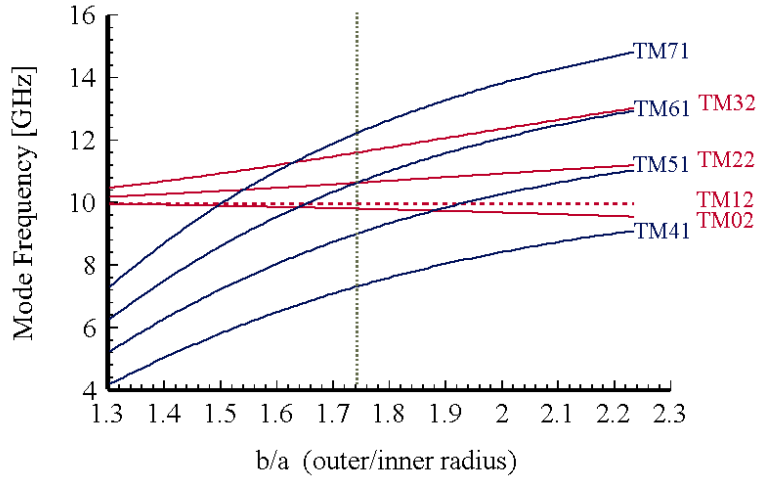
Figure 5.6: Mode chart for the annular ring specific to the Rogers TMM10i substrate. TM_{n1} modes of interest are shown in dark blue and TM_{n2} modes are shown in red. Each b/a geometry is scaled properly so that the TM_{12} mode (the red dotted line) is resonant at 10 GHz. The vertical dotted line shows the chosen b/a ratio for optimal lateral radiation performance.

The mode dependence on b/a ratio can be found from Equation 5.1 and is shown in Figure 5.6. Again, each geometry must be scaled so that the TM_{12} mode resonates at 10 GHz. This set of curves is also dependent on the substrate parameters and is shown here for the TMM10i substrate. As can be seen, there are a set of geometries where the TM_{12} mode occurs at the same frequency as a TM_{n1} mode. Therefore, the TMM10i substrate is chosen in part so that the optimal b/a ratio in Figure 5.4 also allows sufficient mode separation in the frequency response. This is demonstrated by the vertical

105

dotted line in Figure 5.6 which represents the optimal b/a for minimal lateral radiation.

A third consideration for substrate choice is the electrical size of the antenna. The thin substrate allows for additional suppression of substrate modes while the high dielectric constant and the chosen b/a ratio lead to a ring whose diameter is approximately $0.75\lambda_o$.

5.3.3 Passive Measurements

The design of the ring is based on minimized lateral radiation, mode separation, and convenient circuit and array size. The design is shown in Figure 5.2 and is summarized in Table 5.1.

Table 5.1: Summary of design parameters for the passive ring. The substrate parameters are relative dielectric, ϵ_r, substrate thickness, h, and metalization layer thickness, t. The physical parameters of the ring are defined by b and a, the outer and inner radii.

ϵ_r	h	t	b	a	b/a
9.8	25 mil	$9\,\mu$	$10.79\,\mathrm{mm}$	$6.19\,\mathrm{mm}$	1.743

The measured frequency response of the passive ring compares well with the predicted results of Figure 5.6 and with MoM simulations as shown in Figure 5.7. Adequate separation of the TM_{51} and TM_{61} modes is achieved and TM_{12} resonance occurs at $9.95\,\mathrm{GHz}$.

Radiation patterns were taken in a 4-m anechoic chamber and again compared with MoM simulations. The results, displayed in Figure 5.8, show the
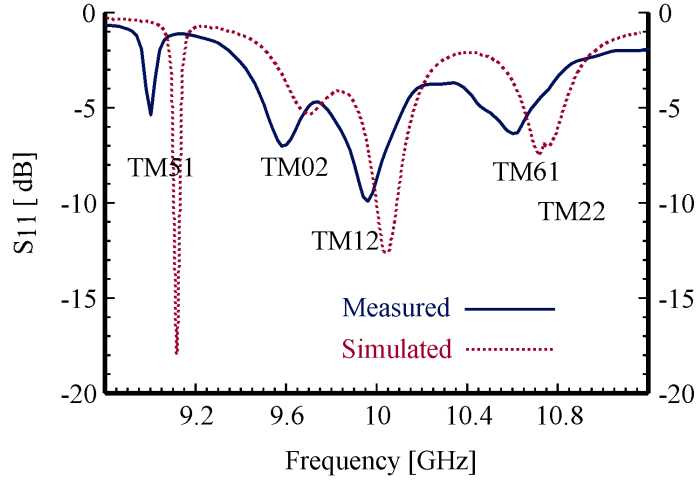
Figure 5.7: Measured and simulated return loss of the passive annular ring.

predicted behavior of minimized E–plane lateral radiation. The small side-lobe in the E–plane is predicted by simulations and is due to the asymmetry in current distribution shown in Figure 5.5 (d). The antenna parameters of interest to the active performance are summarized in Table 5.2.

Table 5.2: Summary of measured parameters for the passive ring.

f_o	G_{ant}	P_{lat} at -90°,+90°	polarization	cross-pol
9.9 GHz	9 dB	-30,-40 dB	linear	-25 dB

5.4   Antenna and Amplifier Integration

The ring antenna is now analyzed as a two-port antenna for integration with the class-E amplifier. This analysis is very similar to that of Chapter 4

107

(a)   (b)
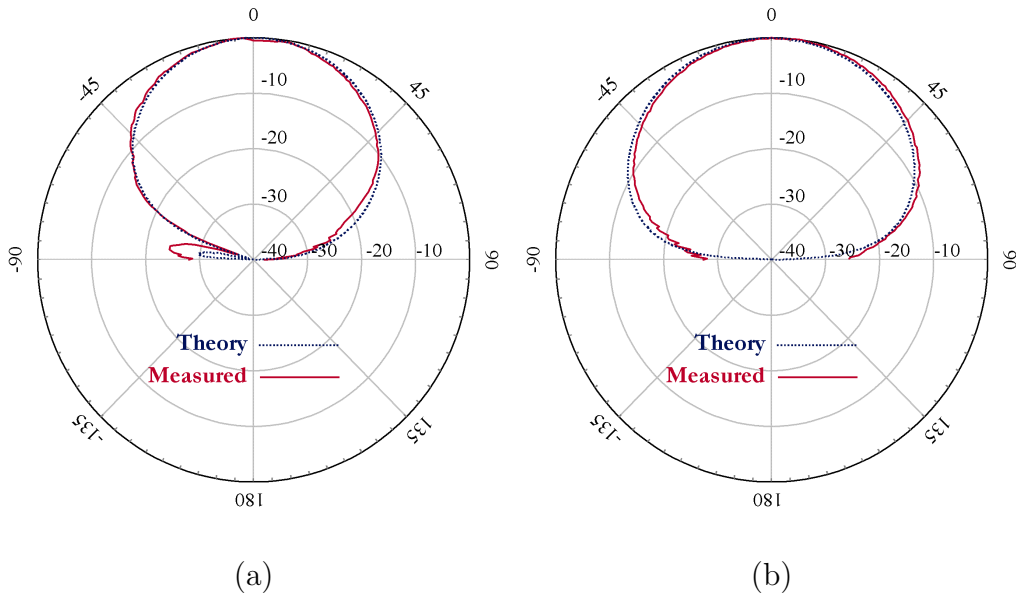
Figure 5.8: Measured and simulated radiation patterns in the E–plane (a) and H–plane (b) for the passive annular ring.

with the exception that the ring antenna is used in place of the asymmetric branch-line coupler.

5.4.1 Class-E Oscillation

As in Chapter 4, a stand-alone class-E amplifier with 50-Ω input and output impedances is swept over a large range of bias levels and input powers. The measured P_{out}, G_{amp}, return loss (RL), and PAE over the swept values provided significant insight into the anticipated class-E oscillator performance. The two plots of Figure 5.9 show how P_{out} and η_{osc} vary with bias and feedback level. While Chapter 4 deals with varying feedback levels for a small

range of bias points, Figure 5.9 shows how the efficiency varies beyond the standard class-E bias point. The design and fabrication steps for the active ring are much more difficult than those for the planar oscillator, and therefore the actual feedback level is harder to pinpoint. Therefore, these two additional graphs are an important tool not only for the design, but also for diagnosing sub-optimal performance. Essentially, Figure 5.9 shows that an optimal feedback region between -6 and -9 dB can be used provided the correct bias.

5.4.2   Port Matching

The class-E oscillator in Chapter 4 uses a four-port coupler with 50-Ω input, coupled, isolated, and output ports. Here, the ring can be considered as a three-port coupler with *unmatched* input, coupled, and output ports where the output port is free-space radiation. The two-port antenna, shown in Figure 5.10, must provide the proper coupling ratio from port-1 to port-2 while presenting the proper load at port-1 for class-E operation. The design process is necessarily iterative and only the final result will be shown here. Figure 5.10 (b) and Figure 5.11 (b) will be used to show how the microstrip circuitry connecting the transistor to the antenna are used together with the antenna to force the desired coupling and class-E match.

As described in Figure 5.10 (b), the port-1 impedance looking into the antenna is known, approximately, from measurements and simulation, but also depends on the port-2 load. The region is in effect a region on the Smith

109
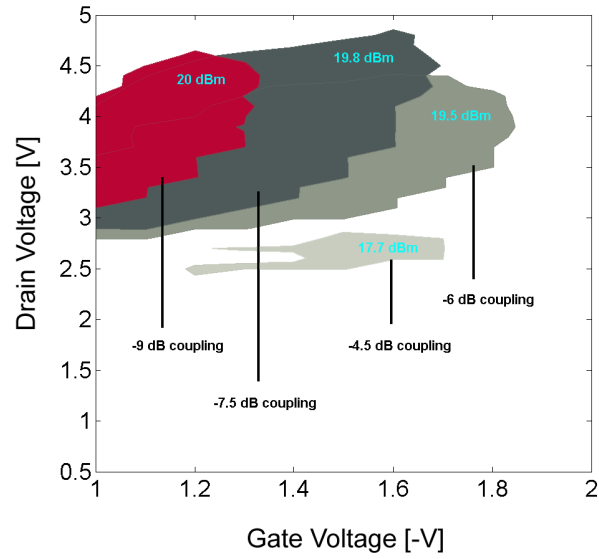
(a)
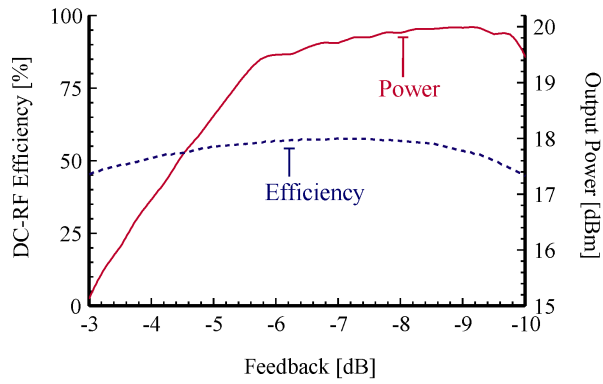
(b)

Figure 5.9: Bias regions for various feedback levels where predicted 50% efficiency and within 3 dB of the maximum power (indicated) occur together (a). Maximum efficiency and associated power for any bias point as a function of feedback (b).

(a)   (b)
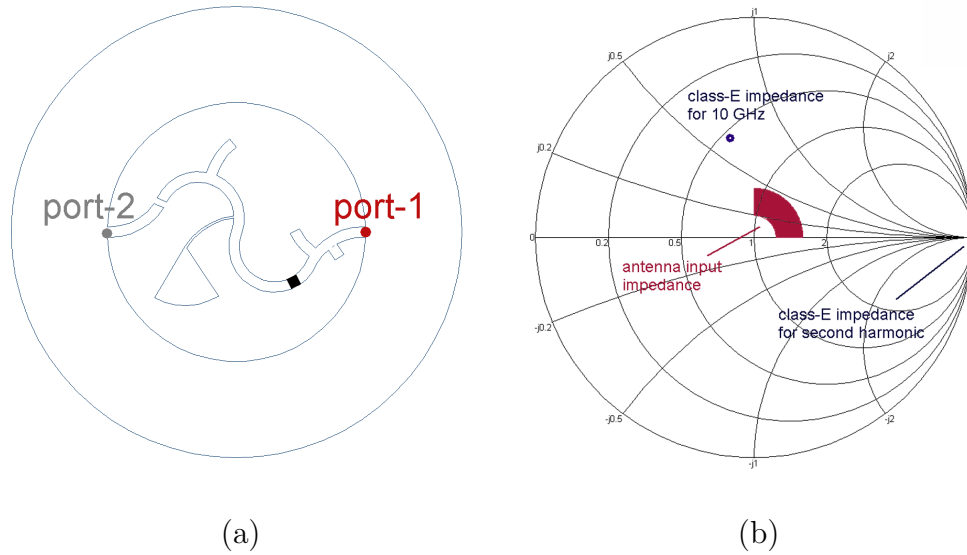
Figure 5.10: The impedance looking into port-1 of the antenna (a) is known to be in the red solid region on the smith chart in (b). The actual location of the impedance depends on the subsequent loading of port-2. The impedance of port-1 is transformed by the tuning stubs on the output side of the transistor to the class-E impedances at the first and second harmonics.

chart that moves as a function of the port-2 loading and which can be transformed with the transistor output stubs to the class-E output impedance.

The Smith chart of Figure 5.11 (b) represents the possible impedance transformations of the transistor input (gate). This is simulated by finding the two-port S-parameters of the ring with MoM solvers and simulating a source and load-pull over the Smith chart on the two ports. Figure 5.11 (b) primarily demonstrates the resulting coupling factor as a function of the port-2 load. It can be seen that the desired coupling factor (around -7 dB in this case) can be achieved for a set of transformations forming a ring on

111

desired region
for port-2 load

resulting S11
with magnitude
less than −12 dB

transistor input
impedance

port-2 loads leading
to desired feedback
levels

(a)   (b)
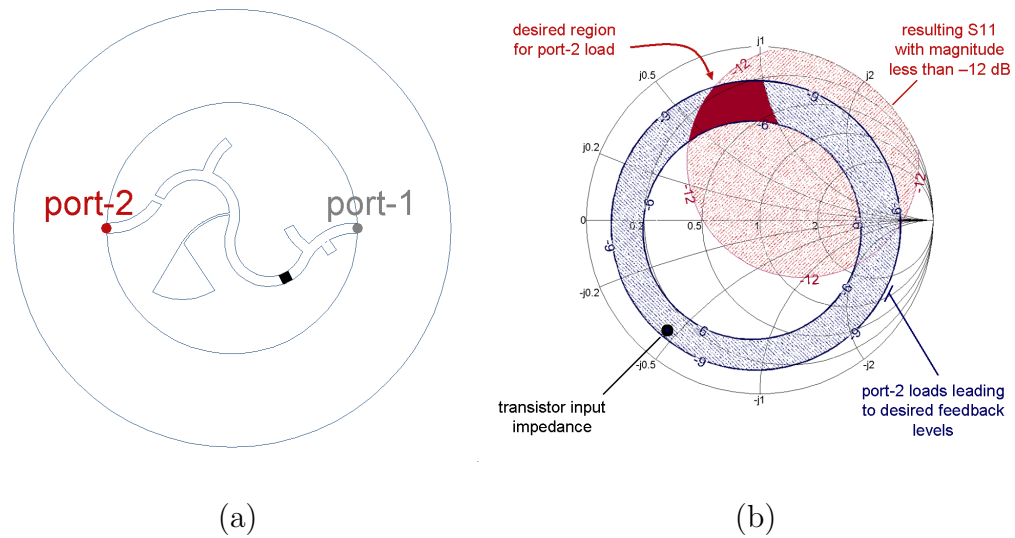
Figure 5.11: The input impedance of the device is transformed such that it presents a load to port-2 of the antenna (a) leading to the desired amount of coupling and desired input impedance (b). The solid red region is chosen for coupling between -6 and -9 dB and resulting port-1 impedance corresponding to the region anticipated in Figure 5.10 (b).

the Smith chart, each leading to a unique port-1 impedance. This load-pull on port-2 is performed with a $50\,\Omega$ source at port-1, as justified in Chapter 4. The resulting input match looking into port-1 for this load-pull is from -12 dB to -∞ inside the red shaded circular region. The solid region marked in Figure 5.11 (b) shows the intersection where the transistor input has been transformed to the correct region of -6 to -9 dB coupling and where the resulting input impedance is nearly the same region as that shown in Figure 5.10 (b), i.e. between -12 and -15 dB at 0 to 90°.

Using the previous analysis, the gate impedance of the transistor is transformed via microstrip transmission line and tuning stub to the colored region

on the Smith chart in Figure 5.11 (b). Subsequently, the resulting impedance looking into the antenna at port-1 can be transformed in the same way to present the class-E match at the output of the transistor. The second harmonic impedance seen by the transistor output should be an open circuit and is accomplished using an open stub (the stub nearest the device). This section has addressed the matching necessary to connect the antenna with the active device. The following section completes the design considerations and summarizes the three-port active behavior.

5.4.3   Loop Analysis

A loop analysis is performed in order to test the integrated antenna and amplifier as a potential oscillator. The loop gain is set by the amount of feedback designed into the passive structure. The loop phase must now be designed for $2\pi n$ radians in order to meet the oscillation condition. This is done with the circuit simulator in ADS by first breaking the loop after the device, as shown in Figure 5.12. The simulation is then performed on the microstrip lines and S-parameter blocks representing the two-port device and two-port antenna. The microstrip lines are designed to simultaneously provide the matching required by the previous section and the $2\pi n$ round-trip phase. A solution for the microstrip layout favorable for the amount of room inside the ring is subsequently realized using meander lines and open stubs.

The loop simulation can also provide some insight into the loop behavior

(a)   (b)
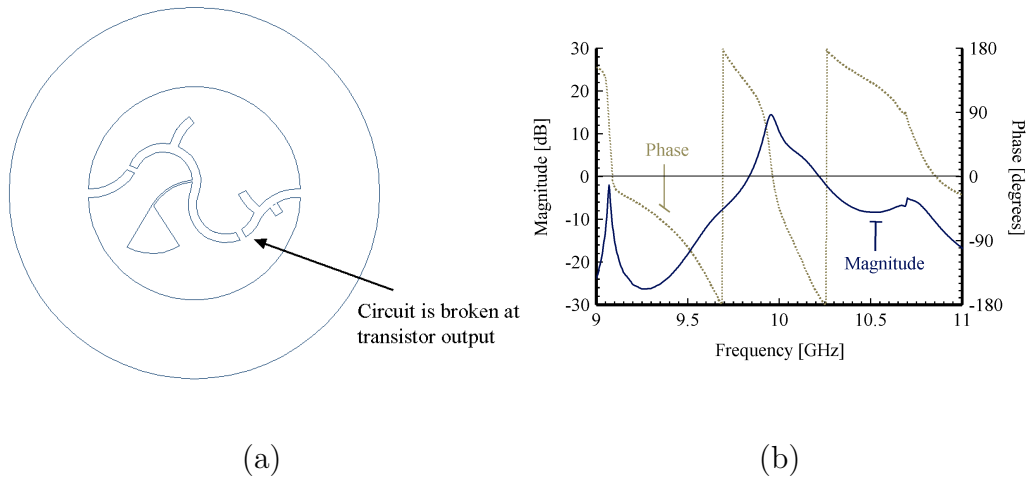
Figure 5.12: The loop gain and phase described by the path in (a) is analyzed
by breaking the circuit at the output of the device and driving it with a test
voltage (using ADS). The result of the loop $S21$ (b)can be compared with
Figure 5.7 to see how the TM_{12} mode is excited while other modes can not
support oscillations. The flow of power in (a) is from left to right in the
microstrip lines, then right to left around the upper and lower arcs of the
ring.

as a function of frequency, as shown in Figure 5.12 (b). It should be noted

first, however, that the gain and phase through the transistor are approximate

because the given S_{21} was originally measured under small-signal conditions

for one particular bias. Still, it can be seen how adjacent modes (compare to

Figure 5.7) are filtered and kept from oscillating, while there is positive loop

gain and proper phase within the TM_{12} mode.

114

5.5 Measurements

The ring is made using a milling machine and the transistor mounted with conductive epoxy and connected using a pair of wire bonds each on the gate and drain pads. As can be seen in Figure 5.2, a radial stub with via is used to bring in the gate bias. An 8.2 pF high-frequency capacitor is used as a DC-block from the drain bias which is supplied by a second via at the location of a current maximum on the ring. This location is chosen as a secondary measure to filter out other ring modes while leaving the TM_{12} mode relatively unperturbed. Finally, the ring is mounted on a circular ground-plane with 30 cm diameter.

Measurements were taken in a computer controlled anechoic chamber with 4 m range. The DC-bias, RF-spectrum analysis, and antenna position were controlled and monitored using *Matlab*. In this way the quantities f_{osc}, P_{rcv}, and I_{ds} were recorded as a function of V_{gs} and V_{ds} or as a function of θ, ϕ to measure the oscillation performance or antenna patterns, respectively.

5.5.1 Oscillator Performance

The bias voltages, V_{gs} and V_{ds}, are the only inputs to the self-oscillating active ring. The oscillation frequency as a function of V_{gs} and V_{ds} is shown in Figure 5.13. Each voltage is incremented in steps of 0.1 V, and the measurement represents 648 data points. The ring oscillates in the TM_{12} mode for all bias points except for the region of very low V_{gs} where the gate was pinched
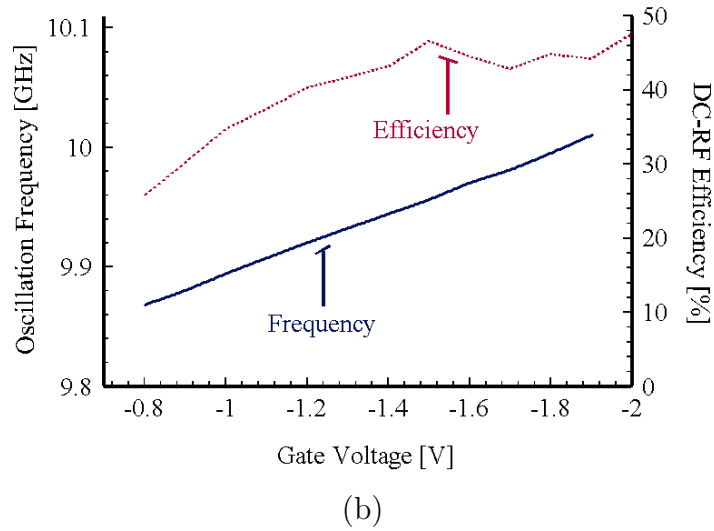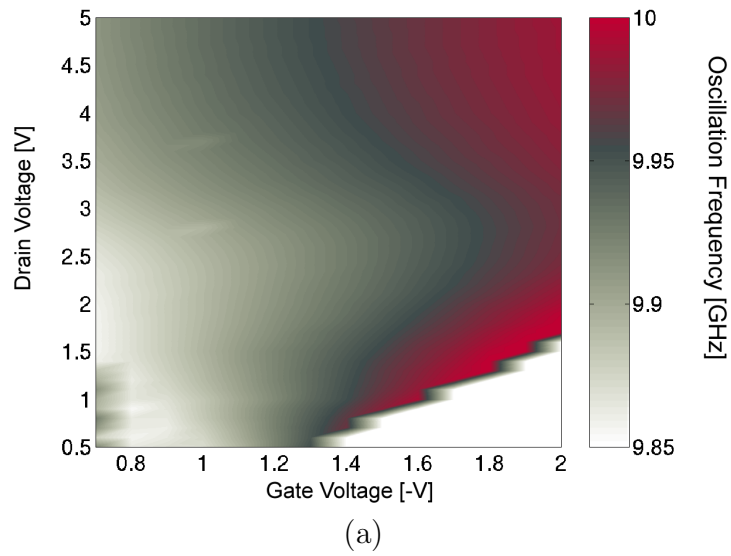
(a)

(b)

Figure 5.13: Measured frequency of oscillation vs. applied gate and drain bias (a) with cross-section for $V_{ds} = 1.5\,\mathrm{V}$ (b). The range of frequencies on the color chart (9.88 to $10\,\mathrm{GHz}$) all fall within the TM_{12} mode.

off and no current drawn. The range of oscillation frequencies spanned from 9.86 to 10.0 GHz, a tuning range of 1.4% which fits safely in the bandwidth of the TM_{12} mode (*c.f.* Figure 5.7).

The resulting P_{out} and η_{osc} are backed out from the measured P_{rcv} and G_{ant} as discussed previously. The color plot of Figure 5.14 shows the optimal region for efficiency over the same bias with additional contours for P_{out}. The output power increases with drain voltage as expected. However, as will be discussed, the high-efficiency region (dark-red region) coincides with the lower power levels.

The plots of Figure 5.13 and Figure 5.14 reflect the amount of coupling and quality of impedance matching, or how well the ring works as an oscillator. They do not represent, however, any of the radiative properties of the integrated antenna.

5.5.2   Antenna Performance

The active antenna patterns are investigated in order to characterize the lateral radiation, analyze polarization, and compare the patterns to those of the passive ring. The E–plane and H–plane cuts shown in Figure 5.15 are taken for the active ring oscillating at 9.9 GHz along with corresponding patterns for the passive ring, driven at the same frequency. Lateral radiation in the E–plane is contained to -34 dB on one side of the antenna, but only to -18 dB on the other. The most likely reason for this is that the via in the patch used to bring in the drain bias not only radiates, but also perturbs

117

(a)

(b)
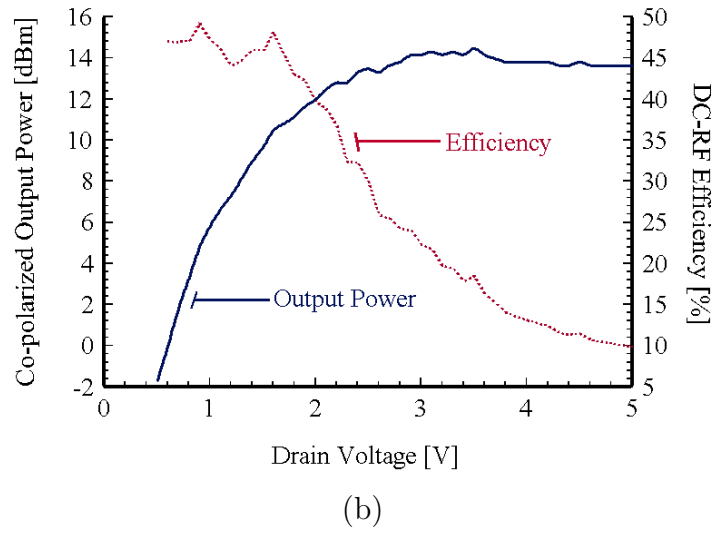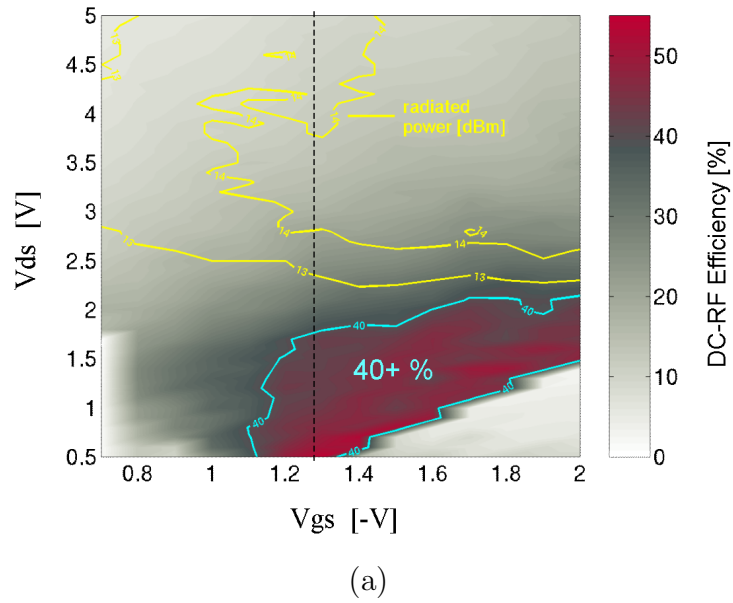
Figure 5.14: Color plot of the measured DC-RF efficiency with contours for the associated output power (a). A cross-section of η_{osc} and P_{out} for $V_gs = -1.3\,\mathrm{V}$ is shown in (b).
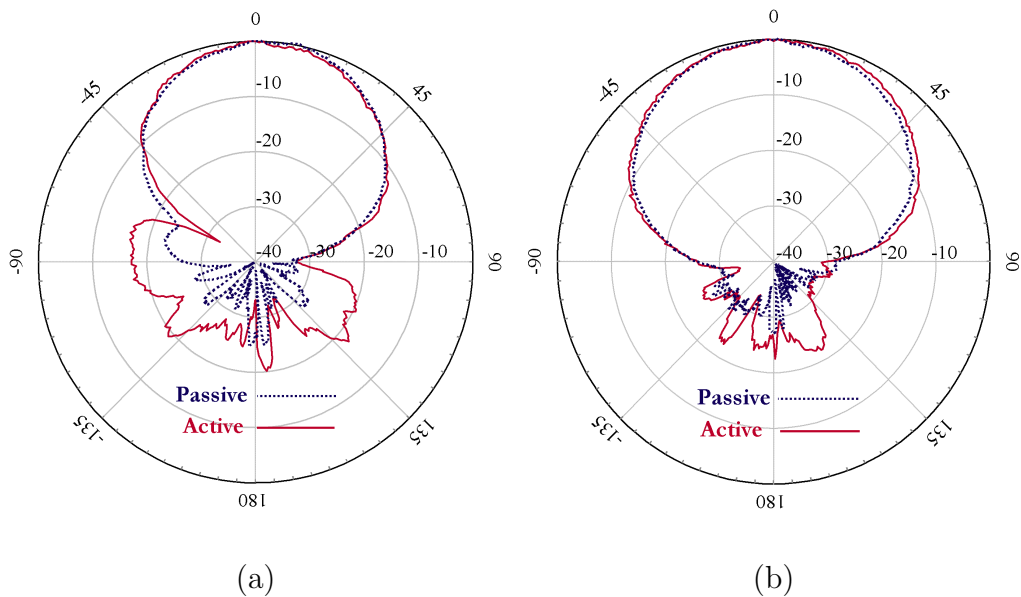
Figure 5.15: Measured E–plane (a) and H–plane (b) radiation patterns at 9.95 GHz compared to the passive patterns taken at the same frequency.

the currents more than was intended. Nevertheless, the agreement between active and passive patterns is very close. This important result permits the assumption that $G_{ant}(active) = G_{ant}(passive)$, and consequently that $P_{out} = ERP/G_{ant}(passive)$. Back-scattering is also increased for the active ring due to bias, however still kept under -18 dB.

Three-dimensional patterns are taken by allowing the active ring to rotate in both the θ and ϕ directions of a spherical coordinate system given by (θ, ϕ, r). The receiving horn is also turned simultaneously in ϕ so that a complete co or cross-polarized pattern can be taken over a hemisphere. Mercator-type projections of the normalized $3D$ radiation patterns with color-scale in

119
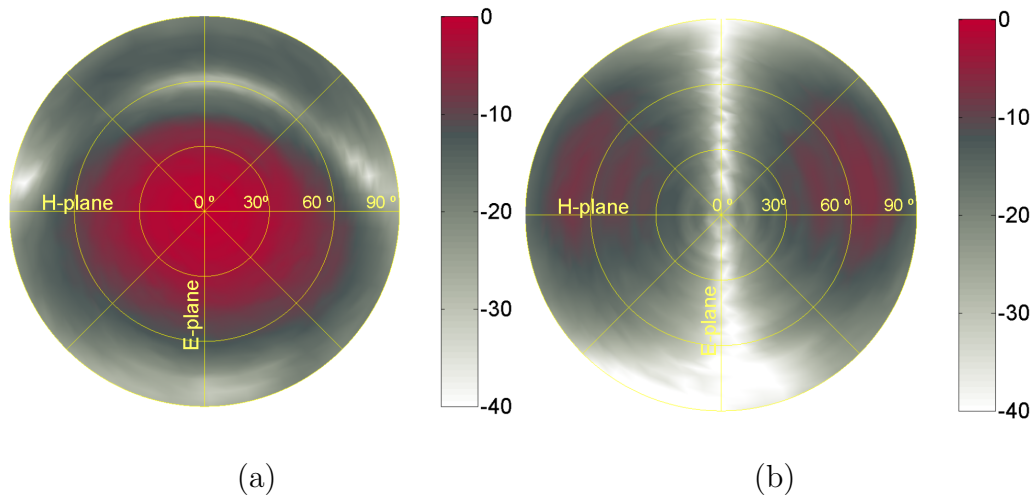
Figure 5.16: Measured co-polarized (a) and cross-polarized (b) radiation patterns taken over a hemisphere of radiation shown in a Mercator-type projection.

Figure 5.17: Measured co-polarized (a) and cross-polarized (b) radiation patterns taken over a hemisphere of radiation shown in a three-dimensional orthographic projection.

dB are shown for both polarizations in Figure 5.16. For comparison purposes, an orthographic projection in the (θ, ϕ, r) coordinates is given in Figure 5.17 where color and r both represent the dB-normalized radiation. Both styles of display show how the lateral radiation is well contained at -20 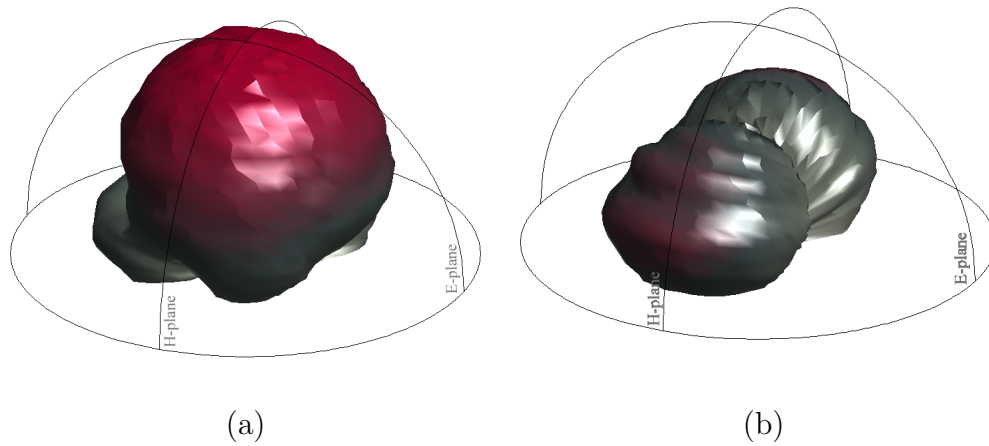dB or lower except for cross-polarized radiation in the H–plane. Furthermore, it can be seen that while the main beam is linearly polarized, a significant amount of energy is lost to cross-polarized radiation off boresite. The antenna parameters are summarized in the following section.

5.5.3   DC–Radiated RF Performance

The combined performance of the class-E oscillator and antenna is summarized in Table 5.3. The table lists three bias points: one for the point of maximum output power (or ERP), another for maximum efficiency (or G_{iso}), and a third point compromising between the two. A fourth instance is given for what is believed to be attainable for this design. Among the numerous references on active antennas mentioned previously, the following listed in Table 5.4 standout as a basis of comparison.

The active ring combines a high gain antenna (8.1 dB) with high DC–RF conversion (-3.1 dB) to achieve 5 dB isotropic conversion gain in a compact element. Using the ring in the TM_{12} mode sacrifices increased physical area for antenna gain; however, the larger antenna size is made up for by the compact nature of the microstrip circuitry. Therefore, this active antenna design has the highest recorded isotropic conversion gain at 10 GHz or above.

Table 5.3: Active ring performance for a high-power bias point, high-efficiency point, compromise between the two, and theoretically attainable performance.

bias [V]	f_{osc} [GHz]	P_{out} [dBm]	η_{osc} [%]	G_{ant} [dB]	P_{lat} [dB]	ERP [dBm]	G_{iso} [dB]	DC [mW]
$V_{ds} = 3.5$ $V_{gs} = -1.6$	9.96	15	22	8	-17,-35	23	2.0	145
$V_{ds} = 1.8$ $V_{gs} = -1.4$	9.95	11	45	8	-17,-35	19	4.5	28
$V_{ds} = 2.0$ $V_{gs} = -1.1$	9.96	13	35	8	-17,-35	21	3.4	57
attainable:								
$V_{ds} = 4.3$ $V_{gs} = -1.4$	10.0	17.8	45	9	-30,-40	26.8	5.5	134

Table 5.4: Comparison of previous work in the field for oscillator and amplifier elements and arrays. The parameter *class* refers to the class of operation in the amplification stage. References marked * are amplifiers. The last two rows refer to the theoretical 24 element array mentioned below based on the class-E annular ring single element measurements(†) and theoretically attainable results(‡) as given in Table 5.3.

	class	f_{osc} [GHz]	P_{out} [dBm]	η_{osc} [%]	G_{ant} [dB]	P_{lat} [dB]	ERP [dBm]	G_{iso} [dB]
Martinez [55]	C	10	NA	45	NA	-10	26.1	NA
Ho [58]	A	7.7	13.3	18	7.5	-13	20.8	0.1
Birkland [64]	A	6	NA	NA	NA	-26	44.5	9.9
Popović [59]	NA	5	27.2	20	16	NA	43.2	9
Radisić* [65]	F	2.6	24.4	63	5.8	-10	30.2	3.8
Pajić* [42]	E	10	32.3	52	19.8	-26	52.1	16.8
Array†	E	10	24.8	45	20.5	< -20	41.8	17
Array‡	E	10	31.6	45	20.5	< -30	52.1	17
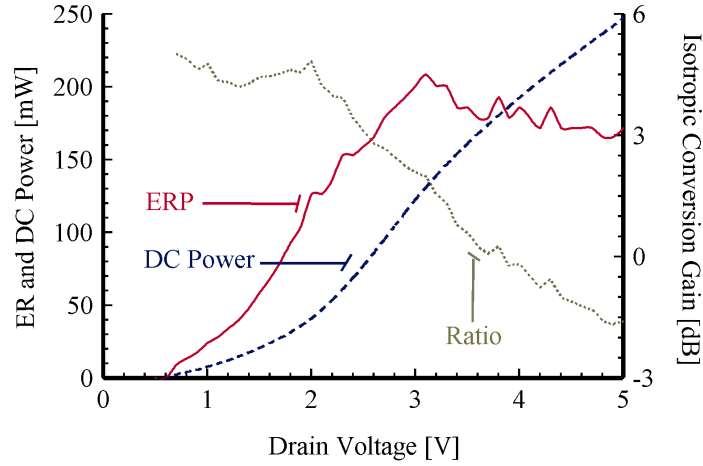
Figure 5.18: ERP and G_{iso} vs. V_{ds}.

Figure 5.18 demonstrates the behavior of ERP and G_{iso} over drain bias. As mentioned previously, if designed properly these two parameters should reach the same peak at roughly the same drain bias. The fact that they do not indicates that the either the coupling factor or the class-E match was substantially off. In Figure 5.19, the amplifier measurements are used to diagnose the problem by attempting to match the measured response of the ring with various coupling scenarios. It was found that the ring measurements agree well with a -3 dB coupling factor over a large bias region in terms of output power, efficiency, and drain current. While this analysis assumes that the class-E match for the ring was relatively close, the result that the oscillator was over-coupled is plausible. It is in fact likely that the microstrip lines and ring coupled more than anticipated. A -3 dB coupling ratio would lead to deep compression levels at higher drain biases, accounting

123
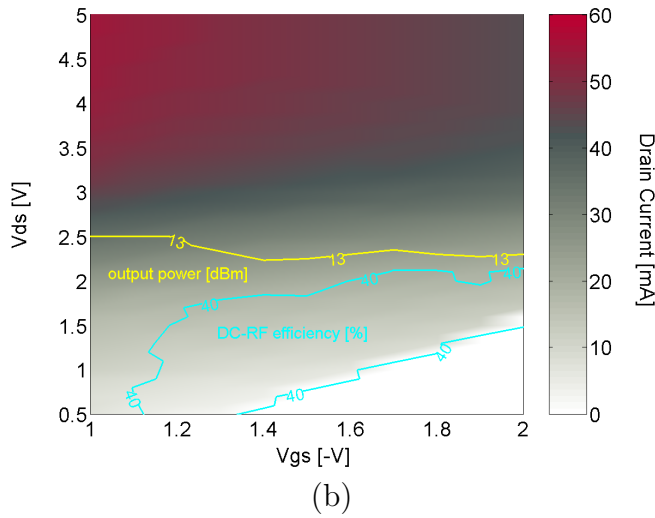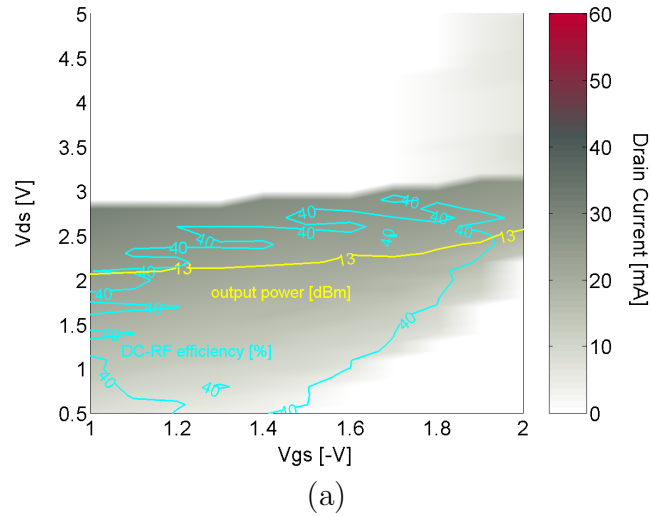
Figure 5.19: Predicted DC–RF efficiency, output power, and drain current for the class-E amplifier with gain of 3 dB (a). Measured values of the same parameters for the active ring (b). This comparison indicates that the ring is oscillating in a highly compressed (over-coupled) mode.

for the lower efficiency at those levels. The coupling problem is addressed in Chapter 6 (future and related work).

5.5.4   A Proposed Active Ring Array
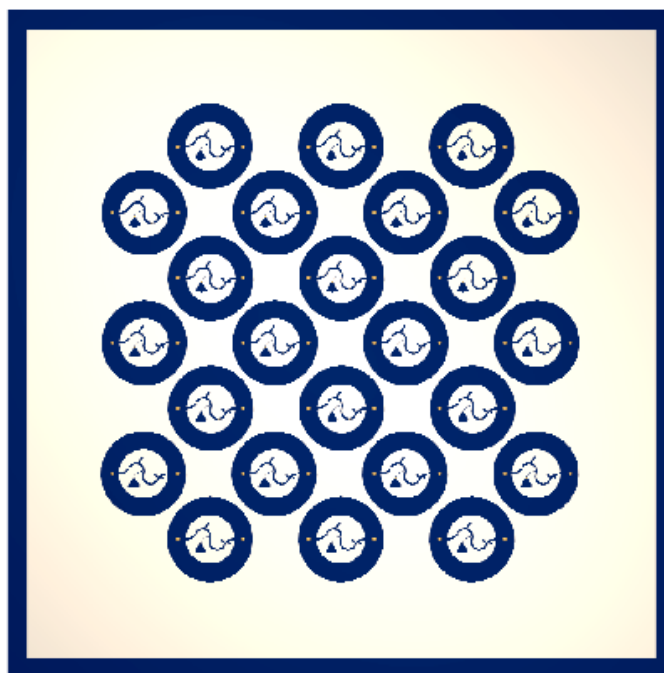
Figure 5.20: Depiction of a proposed phase-locked array of ring oscillators for a focused beam application.

The results shown above are a culmination of several fabrication attempts at the same design. While fabrication tolerances can be a significant source of error, MoM simulations should also be performed on both the ring and microstrip structures together to test for unintended coupling mechanisms. It has been shown, however, that the ring can be used as a high-gain antenna

and two-port coupler appropriate for a high efficiency, self oscillating antenna. Furthermore, the active appears to be a good candidate for an array based on its reduced lateral radiation.

A proposed 24-element array, depicted in Figure 5.20, would require proper phasing between the elements in order to focus the radiated energy to a broadside beam. The reason for limiting the lateral radiation in the single element was not only to increase the antenna gain, but also to allow for controlled inter-element coupling. Inter-element coupling will allow the individual rings to injection lock with a given phase delay. Surface-wave or lateral-wave coupling does not allow precise control of the relative phase differences. The addition of microstrip lines between the elements could provide good control. However, the coupling carried by the microstrip lines must be greater than the lateral wave coupling. Therefore, the lower the lateral wave excitation, the better. The feasibility and application of such an array is discussed further in Chapter 6.

Chapter 6

Related and Future Work

6.1 Microwave Rectification

On the topic of optimal RF–DC conversion efficiency using harmonic terminations, it was shown in Chapter 2 how the reverse breakdown voltage is an impediment for certain rectification modes while the series resistance is a greater factor in other modes. Therefore, the first major challenge for high efficiency microwave rectifiers lies in selecting a diode with optimal parameters for the chosen class of operation. While semiconductor limitations are always a convenient culprit for degraded efficiency performance, proper semiconductor diode choice based on the Chapter 2 conclusions (Table 2.1) can make a significant difference in rectifier performance.

A second challenge is fabrication related: Switched-mode rectifiers are only as efficient as the number of harmonic terminations that can be made

in the circuit [17]. However as a higher number of harmonic terminations are required, the more difficult the fabrication and sensitive the impedance value. Furthermore, physical space for transmission line terminations becomes crowded as the physical length of a quarter-wave section for a given harmonic nears the cross-sectional size of the transmission line. In this case, lumped-element terminations may become necessary.

6.2   Low-Power Rectenna Arrays

Unlike the high-efficiency rectifiers discussed in Chapter 2, Chapter 3 dealt with low-power RF-DC conversion of free-space waves with limited conversion efficiency. While choice of the diode is an area of future concern, the choice of the antenna element will make the most dramatic difference efficiency numbers. While the spiral has many advantages for the application of ambient energy recycling in planar form, it may be possible to optimize a non-frequency independent geometry for a chosen diode over a certain frequency band. As was stated in Chapter 2 the antenna can be optimized separately once the diode has been characterized over the frequencies and power of interest.

In addition to the antenna element, a study should be done to optimize the effective aperture of a unit-cell relative to the range of wavelengths considered. This is tantamount to optimizing the number of diodes per center-wavelength. For instance, if the surface of the rectenna array is divided into

too many rectifying elements, the response at lower band of interest will suffer from aperture efficiency while the upper band will suffer from too little input power per diode. If the antenna size is increased so that the number of elements per surface area is small, then the aperture efficiency at the higher frequencies will suffer, again resulting in too little input power. The optimal solution is likely an array of graduated-sized antennas which make best use of aperture efficiency and received power per diode.

6.3   Microwave Oscillators

The class-E oscillator presented in Chapter 4 was carried out with limited success. Oscillations in class-E mode were never reached, which can be proved by comparison with the predicted results. Instead a *suboptimal* class-E mode was attained where the output power suffers slightly but the efficiency reached was 30% rather than the anticipated 50%. On the other hand, a significant amount of progress was made towards optimizing a 10-GHz oscillator for efficiency using the class-E mode. It was shown how proven high-efficiency performance in the class-E amplifier can be transferred to oscillator performance by correct choice of the bias level in conjunction with the correct feedback level. In addition, it was shown how the nonlinear phase response of the transistor can be taken into account.

The major problem with the topology chosen here was the sensitivity to path length in the feedback loop. Therefore, it is proposed that a dif-
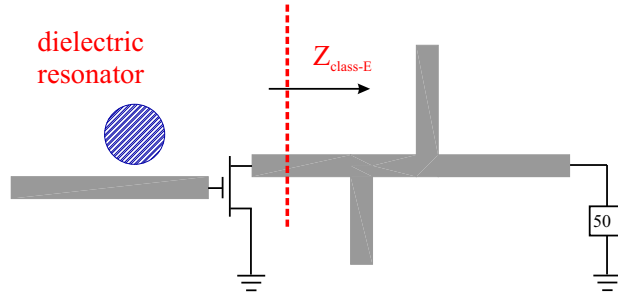
Figure 6.1: Proposed class-E oscillator with series feedback. In this model, the source of the transistor is grounded, the gate is connected to an open-ended line, and the drain is loaded with the class-E impedance, Z_{net}, and open circuit at the second harmonic. Phase stability and frequency tuning can be introducing a dielectric resonator at the gate.

ferent topological structure, one with series feedback, be used in the future (Figure 6.1). While this design will limit control over the feedback level (transistor gain), it will heighten control over the feedback phase. Furthermore, the introduction of a high-Q resonator is more straightforward, as shown in the figure. Post-production tuning can then be done by shortening or extending open ended microstrip lines, or changing the placement of the external resonator. In the parallel feedback design of Chapter 4, tuning was only possible by altering the lengths of the coupling arms in the ring resonator. Nevertheless, the results provided for optimal DC–RF conversion efficiency and output power will be useful in determining whether a given class-E oscillator, in series or parallel feedback mode, and regardless of the device used, has met its full potential.

6.4　Oscillating Antenna Arrays

In Chapter 5, an integrated class-E oscillating annular ring was demonstrated with 4.5 dB isotropic conversion gain. However the true advantages of using using a high-efficiency, self-oscillating antenna manifest when the elements are used in an array. The reason for this stems from the fact that the isotropic conversion gain can be broken up into the product of DC–RF efficiency and antenna gain. In an array it is possible to increase the overall antenna gain dramatically with no effect on the DC–RF conversion rate. This is not true of power combining amplifier arrays using spatial or corporate feeds [69, 70]. In those cases, losses increase with number of elements. Conversely, oscillating arrays have no RF input, do not suffer from feed losses, and power-combining is done purely spatially.

The drawback in using a large number of self-oscillating elements in a power combining array (Figure 5.20) is the complexity of phase-locking the outputs in unison. Each oscillating antenna must be operating at the same frequency and with relative phase shift designed to direct the main beam in the desired direction. This can be done by introducing coupling between adjacent elements so that, in effect, one element injection locks the other. This will allow all coupled elements to operate at the same frequency, but does not ensure the correct phase. If the phase was of no concern, then coupling mechanisms such as surface-wave coupling could be used. Instead, it is proposed that coupling be introduced by microstrip lines connecting

131

the elements. In this way the amount of coupling, and phase can be controlled by tuning stubs, meander lines, and/or location of the feed to the ring. It is estimated that coupling should be on the order of -15 dB; and for this reason special attention was given to radiation in the lateral directions, so that intentional coupling would be much greater in magnitude than the unintentional mutual coupling between elements.

The integrated annular ring has demonstrated the highest isotropic conversion gain for a single element at X-band found in the literature. It has great potential for high-efficiency power beaming with compact size. While an array of the active rings has not been tested yet, a number of array design considerations have been built into the single element design. While there remains some room for improvement in the class-E performance (it is believed that the efficiency could be raised by 5 to 10%), the logical next step for this research is to test the performance of an array.

6.5 DC–DC Conversion

A useful application of growing interest for both the high-efficiency rectifiers and high-efficiency oscillator is a microwave DC–DC converter. This was first presented in [7] at 4.5 GHz. The motivation for this work was to create a converter with size requirements less than the standard kHz to MHz DC–DC converters which typically use bulky ferrite components. The ferrite cores use in the low frequency converters are also responsible for their upper

frequency limit. The microwave DC–DC converter gets around the use of ferrite components by using electromagnetic coupling for Galvonic isolation and planar microstrip layouts.

The prototype DC–DC converter of [7] claims a DC–RF efficiency of up to 86% at 4.5 GHz and an RF–DC overall efficiency of 77%. It should also be noted that the DC–RF conversion was defined as the PAE of a class-E amplifier that drove the rectifier (not an oscillator). Therefore, approximately 10 to 20 mW of RF power were necessary along with the DC input. Ideally the combined performance of the two should have yielded 66% DC–DC conversion efficiency. However the two combined stages produced only a DC–DC conversion rate of only 50%.

At 10 GHz, the anticipated efficiency numbers drop significantly. The highest measured PAE for the class-E amplifier presented in [42] was 57%, and the highest recitification efficiency measured for this thesis at 10 GHz was 30% (Figure 6.3). For this 10-GHz rectifier, an attempt was made at switched mode behavior using a tunable section of transmission line as in the class-Ei circuit presented in Chapter 2. This means that a maximum anticipated DC–DC conversion efficiency would be 18.2% with only 20 mW output power. A drawing of a proposed DC–DC converter design is shown in Figure 6.2. Using the results of the low-Q oscillator presented in Chapter 4, and the rectifier presented in this section, a plot of computed DC–DC conversion efficiency is made as a function of V_{in} (V_{ds} of the oscillator) and V_{out} (the rectified voltage measured across a variable resistor). The result (Figure 6.3)(b) shows that
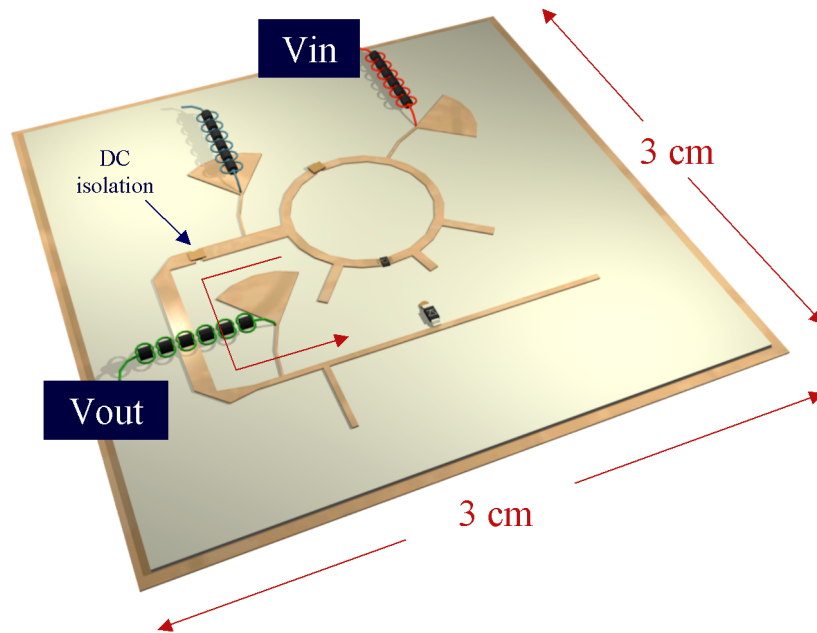
133

Figure 6.2: Drawing of a proposed 10-GHz DC–DC converter using the successfully tested oscillator from Chapter 4 and a 10-GHz rectifier characterized below. The DC input is the drain voltage to the oscillator and the DC output is the rectified voltage separated from the input by a dc blocking capacitor. The direction of RF power flow is indicated by a red arrow.

voltage regulation can not be achieved over a broad range of V_{out}/V_{in} with the optimal efficiency of the converter.

Operation at such a high frequencies with mostly distributed circuit components limits the operational flexibility of the converter. Therefore the ranges of voltage regulation achieved by standard converters can not necessarily be approached by the proposed microwave converters which operate 3 to 4 orders of magnitude higher in frequency. However, there may be still other uses for such converters: The high switching speed of the converter may
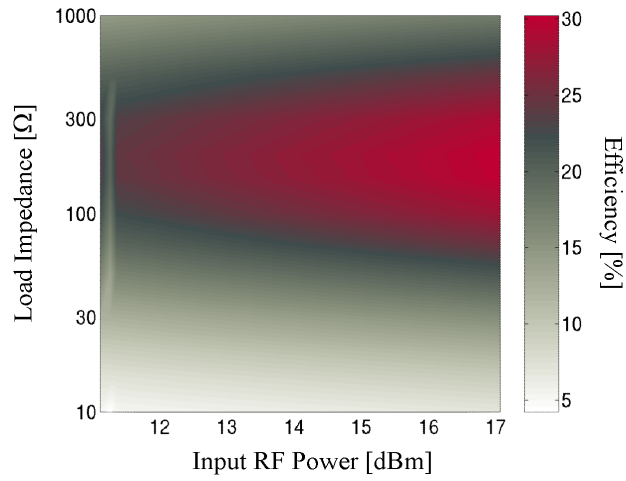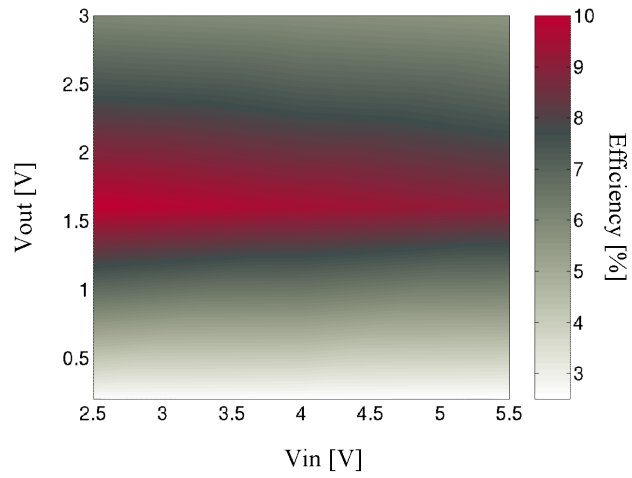
Figure 6.3: Plot of rectification efficiency for a 10-GHz rectifier as a function of RF input power and DC load resistance (a). The results of this plot can be used together with the results of the low-Q oscillator from Chapter 4 to predict the overall DC–DC performance of the converter proposed in Figure 6.2. The computed results in terms of V_{out} and V_{in} are shown in (b).

allow for transient responses significantly faster than previously achieved. In some low power applications, [71], the converter is called upon to switch between *active* and *sleep* modes. The transient response between the two modes can, in some cases, be deemed more important than the DC–DC conversion efficiency during the *active* time period. As an area of interest for future work, a study could be made of the transient behavior of a microwave DC–DC converter with switched drain or gate bias at the rate of 1 MHz and higher to turn the oscillator on and off. HP 547580A Digitizing oscilloscope 54752A 50-GHz module could be used to generate eye diagrams, a useful way of qualifying the switch response of the converter. Such a demonstration of transient response at MHz frequencies would prove the worth of the microwave DC–DC converter more convincingly than the size or efficiency arguments.

Bibliography

[1] E. L. Holzman and R. S. Robertson, *Solid-State Microwave Power Oscillator Design*, Artech House, Boston, MA, 1992.   xiii, 7, 69, 71

[2] Steve C. Cripps, *RF Power Amplifiers for Wireless Communications*, Artech House, Boston MA, 1999.   5

[3] Herbert L. Krauss, Charles W. Bostian, and Frederick H. Raab, *Solid State Radio Engineering*, chapter 14, pp. 432–476, John Wiley, New York, 1980.   5

[4] Thomas B. Mader, *Quasi-Optical Class-E Power Amplifiers*, Ph.D. thesis, Univ. of Colorado at Boulder, Boulder, CO, 1995.   7

[5] Stephan A. Maas, *Nonlinear Microwave Circuits*, chapter 3, IEEE press, New York, NY, 1997.   7

[6] James O. McSpadden, *Rectifying and Oscillating Integrated Antennas*, Ph.D. thesis, Texas A&M University, College Station, TX, 1998.   7, 8

[7] S. Djukic, D. Maksimovic, and Z. Popovic, "A planar 4.5 GHz dc-dc power converter," *IEEE Transactions on Microwave Theory and Techniques*, vol. 47, no. 8, pp. 1457–1460, Aug. 1999. 9, 70, 132, 133

[8] N. Shinohara and H. Matsumoto, "Experimental study of large rectenna array for microwave energy transmission," *IEEE Transactions on Microwave Theory and Techniques*, vol. 46, no. 3, pp. 261–267, Mar. 1998. 9, 38, 39, 70, 98

[9] L.W. Epp, A.R. Khan, H.K. Smith, and R.P Smith, "A compact dual-polarized 8.51-GHz rectenna for high-voltage (50 V) actuator applications," *IEEE Transactions on Microwave Theory and Techniques*, vol. 48, no. 1, pp. 111–120, Jan. 2000. 9, 39, 40

[10] R.H. Rasshofer, M.O. Thieme, and E.M. Biebl, "Circularly polarized millimeter-wave rectenna on silicon substrate," *IEEE Transactions on Microwave Theory and Techniques*, vol. 46, no. 5, pp. 715–718, May 1998. 9

[11] J.A Hagerty, F.B. Helmbrecht, W. McCalpin, R. Zane, and Z. Popović, "Recycling ambient microwave energy with broadband rectenna arrays," *Submitted to IEEE Transactions on Microwave Theory and Techniques, March 2003.* 9

[12] N. O. Sokal and A. D. Sokal, "Class-E - A new class of high efficiency tuned single-ended switching power amplifiers," *IEEE Journal of Solid-State Circuits*, vol. SSC-10, pp. 168–176, June 1975. 17, 72, 75

[13] W. A. Nitz, W. C. Bowman, F. T. Dickens, and F. M. Magalhaes, "A new family of resonant rectifier circuits for high-frequency dc-dc convert-

ers applications," *Applied Power Electronics Conference and Exposition, Conference Proceedings*, pp. 12–22, Feb. 1988.   17

[14] M. K. Kazimierczuk and J. Jóźwik, "Analysis and design of class e zero-current-switching rectifier," *IEEE Transactions on Circuits and Systems*, vol. 37, no. 8, pp. 1000–1009, Aug. 1990.   17

[15] M. K. Kazimierczuk, B. Tomescu, and A. Ivascu, "Class e resonant rectifier with a series capacitor," *IEEE Transactions on Circuits and Systems-I: Fundamental Theory and Applications*, vol. 41, no. 12, pp. 885–890, Dec. 1994.   17

[16] T.B. Mader and Z. Popović, "The transmission-line high efficiency class-e amplifier," *IEEE Microwave and Guided Wave Letters*, vol. 5, no. 9, pp. 290–292, Sept. 1995.   17, 72, 73, 75

[17] F. H. Raab, "Class-E, class-C, and class-F power amplifiers based upon a finite number of harmonics," *IEEE Transactions on Microwave Theory and Techniques*, vol. 49, pp. 1462–1468, Aug. 2001.   18, 73, 128

[18] W. McCalpin, "1 ohm broadband impedance matching network design methodology for hpas," *IEEE Topical Workshop on Power Amplifiers for Wireless Communications, http://paworkshop.ucsd.edu/*, Sept. 2002. 36, 76

[19] W.C. Brown,   "The history of power transmission by radio waves," *IEEE Transactions on Microwave Theory and Techniques*, vol. 32, no. 9, pp. 1230–1242, Sept. 1984.   38

[20] J.O. McSpadden, F.E. Little, M.B Duke, and A. Ignatiev, "An in-space wireless energy transmission experiment," *IECEC Energy Conversion Engineering Conference Proceedings.*, vol. 1, pp. 468–473, Aug. 1996. 38, 39, 40, 98

[21] T. Yoo and K. Chang, "Theoretical and experimental development of 10 and 35 GHz rectennas," *IEEE Transactions on Microwave Theory and Techniques*, vol. 40, no. 6, pp. 1259–1266, June 1992. 38, 39, 44, 63

[22] Y. Fujino, T. Ito, M. Fujita, N. Kaya, H. Matsumoto, K. Kawabata, H. Sawada, and T. Onodera, "A driving test of a small DC motor with a rectenna array," *IEICE Trans. Commun.*, vol. E77-B, no. 4, pp. 526–528, Apr. 1994. 39

[23] W.C. Brown, "An experimental low power density rectenna," *IEEE MTT-S International Microwave Symposium Digest*, pp. 197–200, 1991. 39, 40

[24] J.O McSpadden, R.M. Dickinson, L. Fan, and Kai Chang, "Design and experiments of a high-conversion-efficiency 5.8-GHz rectenna," *IEEE MTT-S International Microwave Symposium Digest*, vol. 2, pp. 1161–1164, 1998. 39

[25] J.O. McSpadden and K. Chang, "A dual polarized circular patch rectifying antenna at 2.45 GHz for microwave power conversion and detection," *IEEE MTT-S International Microwave Symposium Digest*, pp. 1749–1752, 1994. 39

[26] B. Strassner and K. Chang, "A circularly polarized rectifying antenna

array for wireless microwave power transmission with over 78% efficiency," *IEEE MTT-S International Microwave Symposium Digest*, pp. 1535–1538, 2002. 39, 44

[27] J. C. Lin, "Radio frequency exposure and safety associated with base stations used for personal wireless communication," *IEEE Antennas and Propagation Magazine*, vol. 44, no. 1, pp. 180–183, Feb. 2002. 40

[28] J. C. Lin, "Space solar-power stations, wireless power transmissions, and biological implications," *IEEE Microwave Magizine*, pp. 36–42, Mar. 2002. 40

[29] J.A Hagerty and Z. Popović, "An experimental and theoretical characterization of a broadband arbitrarily-polarized rectenna array," *IEEE MTT-S International Microwave Symposium Digest*, vol. 3, pp. 1855–1858, 2001. 40, 64

[30] J. Peeters Weem and Z. Popović, "Vivaldi antenna arrays for SKA," *IEEE Transactions on Antennas and Propagation*, vol. 1, pp. 174–177, 2000. 51

[31] N. Shinohara and H. Matsumoto, "Dependence of dc output of a rectenna array on the method of interconnection of its array elements," *Electrical Engineering in Japan*, vol. 125, no. 1, pp. 9–17, 1998. 55

[32] Cosmo Kramer, *Seinfeld: The Puerto Rican Day Parade*, NBC, New York, New York, 1999.

[33] A. Stratakos, R. Sullivan, S. Sanders, and R. Broderson, "High-

efficiency low-voltage dc-dc conversion for portable applications," in *Low-Voltage/Low-Power Integrated Circuits and Systems*, chapter 12. IEEE Press, Piscataway, NJ, 1999.   64

[34] M. Makowski and D. Maksimović, "Performance limits of switched-capacitor dc-dc converters," *IEEE Power Electronics Specialists Conference*, pp. 1215–1221, 1995.   65

[35] J. Kajiwara, M. Kinoshita, S. Sakiyama, and A. Matsuzawa, "High efficiency and latch-up free switched capacitor up converter on FD-SOI technology," *IEEE Symposium on VLSI Circuits*, pp. 288–291, 2002.   65

[36] P. Koeneman, I. Busch-Vishniac, and K. Wood, "Feasibility of micro power supplies for MEMS," *Journal of Microelectromechanical Systems*, vol. 5, no. 4, pp. 355–362, Dec. 1997.   65

[37] R. LaFollette, J. Harb, and P. Humble, "Microfabricated secondary batteries for remote, autonomous, electronic devices," *IEEE Sixteenth Annual Batter Conference on Applications and Advances*, pp. 349–354, 2001.   66

[38] William C. Jakes, *Microwave Mobile Communications*, IEEE Press, New Jersey, 1974.   67

[39] U. L. Rohde, "Oscillator basics and low-noise techniques for microwave oscillators and VCOs," *GaAs 2000 - Paris, France*, Oct. 2000.   69

[40] W. P. Robbins, *Phase Noise in Signal Sources*, IEE Telecummunications Series 9, Exeter England, 1982. 70

[41] F. H. Raab, "Idealized operation of the class-E tuned power amplifier," *IEEE Transactions on Circuits and Systems*, vol. CAS-24, pp. 725–735, Dec. 1977. 72, 73

[42] S. Pajić and Z. Popović, "An efficient X-band 16-element spatial combiner of switched mode power amplifiers," *Accepted to IEEE Transactions on Microwave Theory and Techniques*, Mar. 2003. 72, 75, 79, 122, 133

[43] E. W. Bryerton, W. A. Shiroma, and Z. Popović, "A 5-ghz high-efficiency class-e oscillator," *IEEE Microwave and Guided Wave Letters*, vol. 6, pp. 441–443, Dec. 1996. 75

[44] M. Prigent, M. Camiade, G. Pataut, D. Reffet, J. M. Nebus, and J. Obregon, "High efficiency free running class-f oscillator," *IEEE MTT-S International Microwave Symposium Digest*, pp. 1317–1320, 1995. 75

[45] J. O. McSpadden, L. Fan, and K. Chang, "High-efficiency ku-band oscillators," *IEEE Transactions on Microwave Theory and Techniques*, vol. 46, no. 10, pp. 1566–1571, Oct. 1998. 75

[46] M.D. Weiss, M. H. Crites, E. W. Bryerton, J. F. Whitaker, and Z. Popović, "Time-domain optical sampling of switched-mode microwave amplifier and multipliers," *IEEE Transactions on Microwave Theory and Techniques*, vol. 47, pp. 2599–2604, Dec. 1999. 76

[47] S. C. Cripps, "A theory for the prediction of GaAs FET load-pull contours," in *1983IEEE MTT-S International Microwave Symposium Digest*, Boston, MA, June 1983, pp. 221–223. 76

[48] H. R. Ahn and I. Wolff, "Asymmetric four-port and branch-line hybrids," *IEEE Transactions on Microwave Theory and Techniques*, vol. 48, pp. 1585–1588, Sep. 2000. 85

[49] I. Wolff and N. Knoppik, "Microstrip ring resonator and dipersion measurements," *Electronics Letters*, vol. 7, No. 26, pp. 779–781, Dec. 1971. 88

[50] Kai Chang, *Microwave Ring Circuits and Antennas*, John Wiley & sons, New York, NY, 1996. 88

[51] L. Hsieh and K. Chang, "Equivalent lumped elements G,L,C, and unloaded Q's of closed- and open-loop ring resonators," *IEEE Transactions on Microwave Theory and Techniques*, vol. 50, pp. 453–460, Feb. 2002. 88

[52] Manoja D. Weiss, *Switched-Mode Microwave Circuits for High-Efficiency Transmitters*, Ph.D. thesis, Univ. of Colorado at Boulder, Boulder, CO, 2001.

[53] Eric Bryerton, *High-Efficiency Switched-Mode Microwave Circuits*, Ph.D. thesis, Univ. of Colorado at Boulder, Boulder, CO, 1999.

[54] W.J. Tseng and S.J. Chung, "Analysis and application of a two-port aperture-coupled microstrip antenna," *IEEE Transactions on Mi-*

crowave Theory and Techniques, vol. 46, no. 5, pp. 530–535, May 1998. 96

[55] R.D. Martinez and R.C. Compton, "High-efficiency FET/microstrip-patch oscillators," *IEEE Antennas and Propagation Magazine*, vol. 36, no. 1, pp. 16–19, Feb. 1994. 96, 122

[56] K. Chang, K.A. Hummer, and G.K. Gopalakrishnan, "Active radiating element using FET source integrated with microstrip patch antenna," *Electronics Letters*, vol. 24, no. 21, pp. 1347–1348, Oct. 1988. 96

[57] D. Bonefacić and J. Bartolić, "Compact active integrated antenna with transistor oscillator and line impedance transformer," *Electronics Letters*, vol. 36, no. 18, pp. 1519–1521, Aug. 2000. 97

[58] C. Ho and K. Chang, "New FET active slotline ring antenna," *Electronics Letters*, vol. 29, pp. 521–522, Mar. 1993. 97, 122

[59] Z. Popović, R.M. Weikle, M. Kim, and D.B. Rutledge, "A 100-MESFET planar grid oscillator," *IEEE Transactions on Microwave Theory and Techniques*, vol. 39, pp. 193–200, Feb. 1991. 97, 122

[60] M.M. Kaleja and E.M. Biebl et al., "Low-cost automobile crash-sensor using a 61 GHz active integrated SIMMWIC antenna," *IEEE MTT-S International Microwave Symposium Digest*, vol. 3, pp. 1969–1972, 2000. 98

[61] R. Garg, P. Bhartia, I. Bahl, and A. Ittipiboon, *Microstrip Antenna Design Handbook*, chapter 5, Artech House, Boston, 2001. 99

[62] M.A. Khayat, J.T. Williams, D.R. Jackson, and S.A. Long, "Mutual coupling between reduced surface-wave microstrip antennas," *IEEE Transactions on Antennas and Propagation*, vol. 48, no. 10, pp. 1581–1593, Oct. 2000. 101

[63] I. Papapolymerou, R.F. Drayton, and L.P.B. Katehi, "Micromachined patch antennas," *IEEE Transactions on Antennas and Propagation*, vol. 46, no. 2, pp. 275–283, Feb. 98. 101

[64] J. Birkland and T. Itoh, "A 16 element quasi-optical FET oscillator power combining array with external injection locking," *IEEE Transactions on Microwave Theory and Techniques*, vol. 40, pp. 475–481, Mar. 1992. 122

[65] V. Radisic, Y. Qian, and T. Itoh, "Class f power amplifier integrated with circular sector microstrip antenna," *IEEE MTT-S International Microwave Symposium Digest*, vol. 2, pp. 687–690, 1997. 122

[66] Y.S. Wu and F.J. Rosenbaum, "Mode chart for microstrip ring resonators," *IEEE Transactions on Microwave Theory and Techniques*, vol. 21, pp. 487–489, 1973.

[67] A. Bhattacharyya and R. Garg, "Analysis of annular ring microstrip antenna using cavity model," *Archiv für Elektronik und Übertragungstechnik*, vol. 39, pp. 185–189, 1985.

[68] R.A. York and R.C. Compton, "Quasi-optical power combining using mutually synchronized oscillator arrays," *IEEE Transactions on Microwave Theory and Techniques*, vol. 39, no. 6, pp. 1000–1009, June 1991.

[69] Todd Marshall, *Design and Characterization of Low-Cost Ka-Band Amplifier Antenna Arrays*, Ph.D. thesis, Univ. of Colorado, Boulder, CO, 2000. 131

[70] Robert A. York, "Quasi-optical power combining," in *Active and Quasi-optical arrays for solid-state power combining*, Robert A. York and Zoya B. Popović, Eds. John Wiley, New York, 1997. 131

[71] M. T. Zhang, M. M. Javanovic, and F. C. Lee, "Design considerations for low-voltage on-board dc/dc modules for next generations of data processing circuits," *IEEE Transactions on Power Electronics*, vol. 11, pp. 328–337, Mar. 1996. 136

[72] Michael A. Forman, *Active Antenna Arrays For Power Combining and Communication*, Ph.D. thesis, Univ. of Colorado at Boulder, Boulder, CO, 2001.